UNIVERSITY OF TRENTO
Department of Physics

Doctoral Programme in Physics, XXX cycle

Doctoral Thesis

Gas transport properties and free volume structure of polymer nanocomposite membranes

Supervisor:
Riccardo Checchetto

Author:
David Roilo

Academic Year 2016-2017

Contents

Abstract

This thesis work presents the results of experimental studies on the gas transport properties of three polymer-based membrane systems: (i) amine-modified epoxy resins, (ii) epoxy resin nanocomposites containing Few Layer Graphene (FLG) nanoplatelets as dispersed fillers and (iii) nanocellulose-based membranes. The gas transport properties of the present membrane systems were studied by gas phase permeation techniques changing sample temperature and penetrant molecules; results were discussed in the framework of the free volume theory of diffusion, using information on the samples' free volume structure as experimentally obtained by Positron Annihilation Lifetime Spectroscopy (PALS). Results evidenced that the transport properties of small penetrant molecules are controlled by the membranes' free volume structure, which determines, in fact, the penetrant diffusion kinetics.

The free volume of epoxy resins was changed by changing their crosslink density but maintaining same chemical environment for penetrant molecules: it was observed that, reducing the free volume structure, the gas diffusivity decreases but no relevant changes in the gas solubility occurred. The experimentally obtained fractional free volume values permitted to reproduce the measured diffusivity values and their variation with temperature, using equations provided by the free volume theory of diffusion.

Increasing the amount of FLG fillers in epoxy-based nanocomposites, we observed a progressive gas permeability decrease, which was accompanied by a progressive reduction of their free volume. This correlation was attributed to the formation of constrained, gas-impermeable polymer regions at the filler-matrix interfaces. The thickness of these regions was evaluated by the reduction of the nanocomposites' fractional free volume with respect to the free volume of the pure polymer matrix; its value permits to reproduce quantitatively the experimental permeation data of the nanocomposites at all examined temperatures, filler concentrations and test gases.

Few micrometers thick nanocellulose films deposited on polylactic acid substrates act as impermeable barriers for CO_2, O_2, and N_2 and reduce the D_2 (deuterium) and He permeation flux by a factor of $\sim 10^3$. Penetrant transport through this biopolymer is controlled by the solution-diffusion mechanism and barrier properties are due to the extremely low penetrant diffusivity. The free volume in the nanocellulose coatings consists of interconnected elongated cavities with sub-nanometer

cross-sectional size where the selective transport of the small size penetrants is due to sieving effects. D_2 and He diffusion has thermally activated character and occurs in configurational regime.

CHAPTER 1

Introduction

Membranes are thin layers able to control the transport of chemical species in contact with them (Baker, 2004). Membrane systems are widely used in technological molecular separation processes as, for example, water purification/desalination, gas separation and pervaporation processes (Baker, 2009; Semiat and Hasson, 2009; Van der Bruggen, 2009). Membranes can be classified according to different criteria: their geometry (symmetric vs. asymmetric membranes, planar vs. cylindrical membranes), structural factors (porous vs. dense membranes), the membrane material (polymeric, ceramic, metallic membranes), the origin of the material (natural vs. synthetic membranes) and their application (gas barrier, gas separation).

The topic of this thesis is gas transport through polymer and polymer nanocomposite (PNC) membranes. Gas transport through polymers is generally controlled by the solution-diffusion mechanism (Baker, 2004) (see Figure 1): gas molecules are absorbed in the side of the membrane exposed to the gas (solution process) and migrate to the opposite side driven by a concentration gradient (diffusion process). The gas solubility S and the penetrant diffusivity D are parameters determining the gas flux J through the membrane. These parameters show an Arrhenius type temperature behavior and their value depends on the specific polymer-penetrant

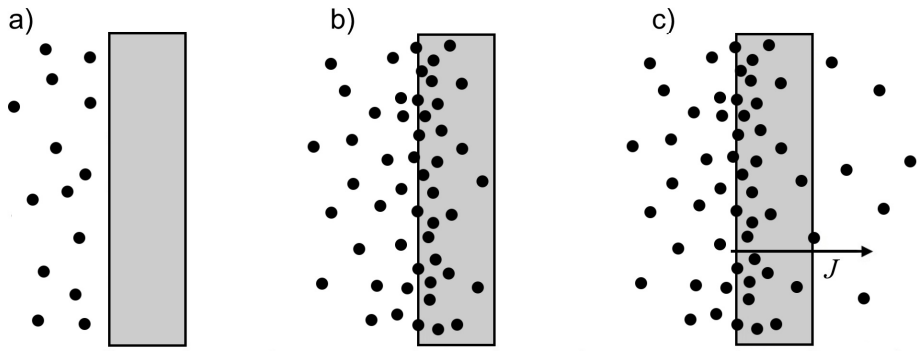

FIGURE 1. Permeation in a dense membrane through the solution-diffusion process. When one side of the membrane is exposed to a gas (a), the gas absorbs in it and diffuses down a concentration gradient (b), until it reaches the opposite side of the membrane, where it desorbs (c).

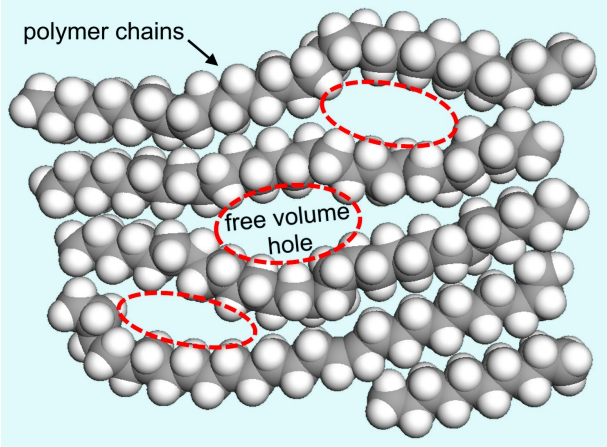

FIGURE 2. Graphical representation of free volume in polymers. Holes are evidenced by the red dashed lines.

system. Gas diffusivity D is related to the structure and dynamics of the sites where penetrant molecules are hosted and migrate (Matteucci et al., 2006).

In dense polymeric membranes, penetrant molecules are hosted in cavities formed by thermal fluctuations of the polymer chains, see Figure 2 (Baker, 2004). These cavities (called free volume holes) have size in the sub- nanometer range and form the polymer free volume. Free volume holes have temperature- dependent size and their thermal redistribution in the polymer allows the migration of penetrant gas molecules which diffuse, in fact, by successive jumps between adjacent holes (Vieth, 1991). When the interactions between the penetrant molecules and the polymer are negligible, then the free volume structure of the polymer, which is described by hole size distribution and hole number density, is the key factor controlling the penetrant diffusion process (Matteucci et al., 2006).

In microporous polymers, holes have size larger than in dense polymers and are rigid, that is do not fluctuate in position and size. These holes are generally called pores and, when interconnected, form preferential diffusion paths for penetrant molecules (Baker, 2004). Depending on the ratio between the size of the penetrant molecule and the size of the pore, diffusion in microporous polymers occurs by Knudsen mechanism or in configurational regime (see Figure 3) (Burganos, 2010). Knudsen diffusion occurs when the mean free path of the gas molecules in the interconnected pores is limited by the collisions between molecules and pore walls: gas diffusivity is proportional to the average thermal velocity of the molecules and to the pore size. When the pore size becomes comparable to the size of the penetrant molecule, then sieving effects and configurational diffusion processes define the penetrant transport. Gas molecules with size larger than that of the pore are excluded, whereas smaller molecules interact with the surface of the pore walls, lose

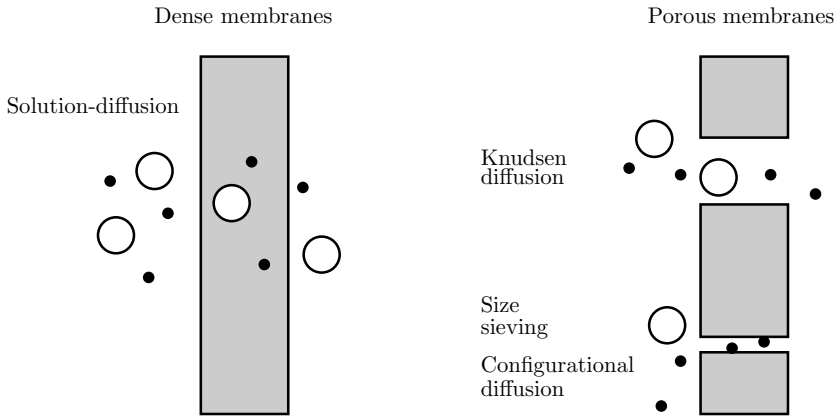

FIGURE 3. Diffusion mechanisms in microporous and dense polymer membranes.

their gaseous state and migrate with a thermally activated mechanism very similar to the surface diffusion process (Burganos, 2010; Baker, 2004).

In this thesis, we present our activity on the preparation, structural characterization and functional analysis (gas transport properties) of three kinds of polymer membranes:

(1) membranes made of amine- modified epoxy resins;
(2) membranes made of tightly packed nanocellulose fibril assemblies;
(3) nanocomposite membranes obtained dispersing filler nanoparticles in the amine- modified epoxy resins and in the tightly packed nanocellulose assemblies.

Epoxy resins are synthetic crosslinked polymers with dense structure having different technological applications (Pascault et al., 2012). Their structural properties, including the free volume structure, can be easily tuned by changing their crosslink density without altering the chemical environment for penetrant molecules (George and Thomas, 2001; Lin et al., 2005).

Nanocellulose is a biopolymer consisting of rod-like cellulose crystals (fibrils). Such fibrils self- assemble forming highly packed layers with rigid cavities between the nanofibrils (Fukuzumi et al., 2011). Crystalline fibrils are gas impermeable (Aulin et al., 2010) and nanocellulose films are thus of great interest for applications in packaging technology (Dufresne, 2013).

PNC membranes (also called mixed matrix membranes, MMM) are produced by dispersing filler nanoparticles in a polymer matrix. PNCs are attracting great interest in the membrane technology because they have the potential to surpass the

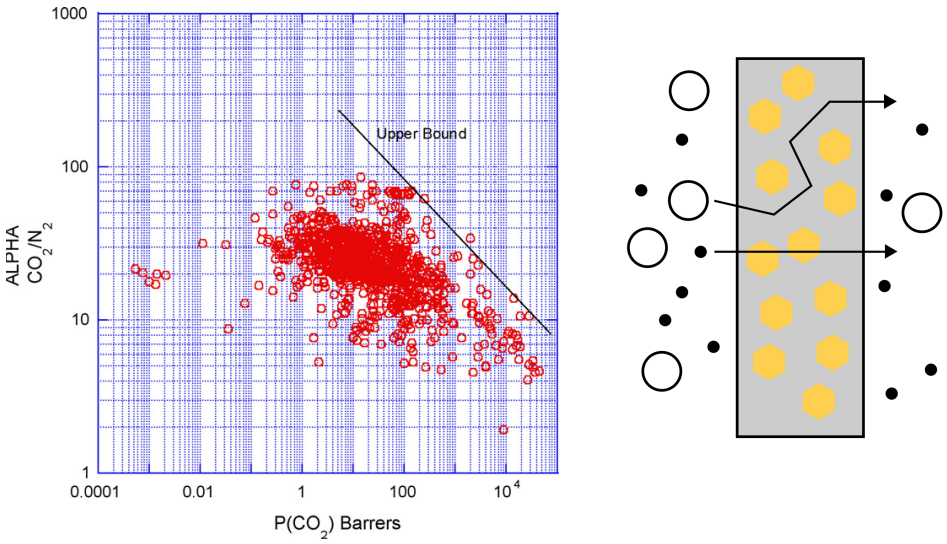

FIGURE 4. Left: Robeson plot for CO_2/N_2 separation. Circles represent polymer membranes. Their CO_2/N_2 selectivity is plotted against CO_2 permeability. All polymer membranes' performances lie below the upper bound line. Reproduced from (Robeson, 2008) with permission from Elsevier. Right: a PNC membrane. The yellow symbols represent molecular sieve fillers allowing transport of small penetrants, while blocking bigger molecules.

performances of pure polymeric membranes (Robeson limit, (Robeson, 1991, 2008), see Figure 4) both in gas separation and gas barrier applications (Paul and Robeson, 2008; Basu et al., 2010; Aroon et al., 2010). In fact, porous fillers dispersed in the polymer matrix can improve its selectivity by selectively allowing transport of small penetrants (Moore et al., 2004) while impermeable fillers can hinder molecular transport, thus enhancing the gas barrier properties of the pure polymer (Cui et al., 2016). Their performances are defined not only by the gas transport properties of the matrix and filler material, but also by the chemical-physical properties of the filler-matrix interface layers. Extended defects can form here, see Figure 5, influencing the transport properties of the nanocomposites (Aroon et al., 2010; Chung et al., 2007). We prepared gas barrier polymer nanocomposites by using the previously studied polymers as matrices and Few Layer Graphene (FLG) nanoplatelets and TiO_2 nanoparticles as gas-impermeable fillers (Cui et al., 2016; Zhou et al., 2009).

We used the described membranes to examine the correlation between gas transport properties of the pure polymers and of the polymer nanocomposites and

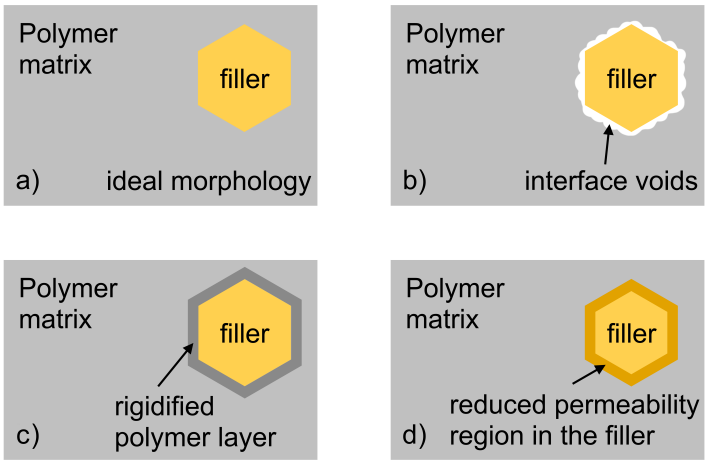

FIGURE 5. Filler-matrix interface structure. a) ideal morphology: the polymer matrix wets the filler particle and polymer interface layers maintain their bulk gas transport properties; b) interface voids, formed as a consequence of poor polymer-filler adhesion; c) polymer rigidification: mobility of the polymer chains in contact with the filler particles is hindered; d) pore blockage (occurring only for porous fillers): polymer chains partially enter the fillers' pores, clogging them (Aroon et al., 2010; Pal, 2008).

their free volume structure, to gain a deeper fundamental knowledge on the phenomena governing mass transport processes. To this task: i) we prepared pure and nanocomposite samples with systematically different free volume structure by changing the crosslink density and the nature and content of filler nanoparticles, ii) we studied their gas transport properties at different temperatures by gas phase permeation techniques (Checchetto et al., 1995) using different gas molecules and iii) we examined the free volume structure of the membrane samples by Positron Annihilation Lifetime Spectroscopy Consolati and Quasso (2010). The main results of this thesis work are:

(1) Changing sample temperature and crosslink density, the analyses evidenced a clear correlation between diffusivity values and free volume structure of the epoxy resins and their nanocomposites. No correlation was, on the opposite, observed in porous nanocellulose films.
(2) We elaborated a model providing an equation which permits to evaluate the fractional free volume of the samples (defined as the ratio of the specific free volume to the specific volume of a polymer) and its variation with temperature using PALS and thermomechanical data as input parameters.

(3) We reproduced the measured transport parameters in the epoxy membranes using equations provided by the free volume theory of diffusion with the fractional free volume value obtained by our model as input parameter; the apparent Arrhenius behavior of the diffusivity and permeability data was explained by a linear increase of the fractional free volume with temperature.

(4) We demonstrated that the improved gas barrier properties after dispersion of FLG nanoplatelets in the studied polymer matrix are consequence of the formation of rigidified polymer regions surrounding the filler particles. The quantitative analysis of PALS data permitted to evaluate the thickness of the rigidified regions and quantitatively reproduce the permeability reduction of the nanocomposites as a function of the filler content at each examined temperature.

(5) We demonstrated that the well known gas barrier properties of nanocellulose coatings are consequence of their free volume structure, which consists of rigid elongated cavities where penetrant diffusion occurs in configurational regime. PALS analysis allowed to measure the size of these cavities explaining the preferential transport of small size penetrant molecules as a consequence of sieving effects.

This thesis work is presented in the following chapters:

Chapter 2 provides theoretical notes on the gas transport in polymers and describes the solution-diffusion model. Equations describing the relation between the gas flux through a planar membrane and the gas solubility S and diffusivity D will be obtained and discussed. This chapter also provides a description of the free volume in polymers and defines the fractional free volume parameter. Notes on the free volume theory of diffusion will be then presented, to obtain equations describing the penetrant diffusivity as a function of the fractional free volume.

Chapter 3 provides information on the polymers and PNC preparation procedure and information on the results of their structural characterization.

Chapter 4 describes the experimental techniques used for the study of the gas transport properties and the analysis of the free volume structure. Gas transport properties were studied by gas-phase permeation technique using specifically home-built systems; the procedures to evaluate D and S thanks to the equations developed in chapter 2 will also be presented. The free volume structure was studied by Positron Annihilation Lifetime Spectroscopy technique, using laboratory-scale apparatuses (fast-fast coincidence lifetime setup, Department of Physics and L-NESS, Politecnico di Milano, Milano, Italy) and facilities (NEPOMUC positron source, Universität der Bundeswehr (Munich) und Institut fur Angewandte Physik und Messtechnik, Neubiberg, Germany).

Chapter 5 presents the results of the studies carried out using pure epoxy resin membranes. Results in this chapter will quantitatively clarify the correlation between sample free volume structure and gas transport properties using experimental data obtained at different temperatures and with different molecular penetrants.

Chapter 6 presents the results of the studies carried out using epoxy based nanocomposites with few layer graphene nanoplatelets as a dispersed phase. Data obtained from PALS measurements will clarify the role of the fillers in the observed reduction of the gas transport rates outlining the role of the interface layers.

Chapter 7 presents the results of the gas transport measurements carried out on nanocellulose and nanocellulose composite coatings deposited on PLA support. Composites were obtained by the dispersing TiO_2 nanoparticles in the nanocellulose layers. PALS analysis of the free volume structure is also presented to explain the observed gas barrier properties.

Appendix A presents the results of a study on the water vapor and gas transport properties of membranes made with polypropylene-carbon nanotube nanocomposites. This is a collaborative work carried out with colleagues of the Foundation for Research and Technology-Hellas at Patras and the University of Patras (Greece). In this appendix we mostly outline the author's contribution to this research work.

CHAPTER 2

Theory of gas transport in polymer membranes

In this chapter, we will discuss the physical processes controlling gas transport through dense membranes and we will discuss the solution-diffusion model. The quantities that characterize the system composed by polymeric membrane and permeant, most notably solubility S and diffusivity D, will be introduced and it will be explained how they can be determined from experiments.

In order to understand the following discussion, it is useful to simply describe the phenomenology of permeation, thus introducing the most relevant terms and allowing the reader to visualize the process. In all gas transport experiments and applications, the membrane is thin (meaning that its thickness is much smaller than the lateral size) and separates two chambers. The penetrant gas flows through the membrane from an upstream fluid phase to a downstream fluid phase, i.e. from one chamber to the other. The side of the membrane facing the chamber in which gas pressure is larger is called high pressure side (HPS) or upstream side, whereas the opposite, downstream side is called low pressure side (LPS). We will thus say that molecules move through the membrane from the high pressure side to the low pressure side.

In the following discussion, we will use a frame of reference in which the membrane is at rest and its surfaces are perpendicular to the x axis. In particular, the upstream surface of the membrane is a portion of the plane $x = 0$ and the downstream surface is a portion of the plane $x = \ell$, where ℓ is the thickness of the membrane.

2.1. The solution-diffusion model

The solution-diffusion model describes molecular transport through dense membranes as a combination of three different processes. (i) Molecular sorption: gas molecules are absorbed in the surface layers of the membrane which are exposed to the gas (upstream surface), (ii) molecular diffusion: gas molecules diffuse to the opposite side of the membrane (downstream surface), under a gas concentration gradient established in the membrane and (iii) molecular desorption: gas molecules at the downstream surface layers return in gas phase.

The model assumes that equilibrium conditions between molecules in gas phase and molecules absorbed in the membrane surface layers are rapidly set: this hypothesis is verified in almost all membrane processes because the diffusion process is

much slower than gas absorption and desorption at the membrane surfaces. Consequently, the sorption process can be described using the equilibrium Henry's law (Baker, 2004), which permits to calculate the gas concentration at the membrane surfaces and describe the concentration gradient in the membrane.

Fick's first law for diffusion establishes a relation between the gas concentration gradient in the membrane and gas transport rates.

2.1.1. Sorption of gases in polymers. In this section, we will describe the sorption of gases in rubbery polymers, whereas sorption in glassy polymers will be discussed later (section 2.1.5). According to Henry's law, for rubbery polymers immersed in a gas, the concentration c of the gas dissolved in the polymer at equilibrium is directly proportional to the pressure p of the gas phase, the proportionality coefficient being the solubility S:

$$c = S\,p \tag{2.1.1}$$

Although this is just an approximation (which holds for low gas pressures), linear isotherms are observed for light gases at essentially all pressures of practical interest and are characteristic of gas sorption in rubbery polymers (Paul, 2010; Matteucci et al., 2006).

In section 2.2, a more detailed analysis of the processes involved in gas sorption will be given, providing a microscopic interpretation of the parameter S.

2.1.2. Fick's laws for diffusion. Diffusion is the process by which matter is transported between different regions of a system by random molecular motions. The first quantitative description of this phenomenon was given by Fick, who noticed the similarity between mass transport and heat conduction (Crank, 1979). For single component diffusion in a isotropic medium (e.g. a single gas diffusing in a polymer), Fick's first law can be expressed as

$$\boldsymbol{J} = -D\nabla c \tag{2.1.2}$$

where $\boldsymbol{J}$ is the flux of the diffusing species, c is its concentration inside the medium and D is the diffusion coefficient or diffusivity (Vieth, 1991). When the concentration gradient ∇c lies on a specific direction $\hat{x}$, Fick's first law can be expressed in the following way:

$$J = -D\frac{\mathrm{d}c(x)}{\mathrm{d}x} \tag{2.1.3}$$

The time evolution of the concentration of the dissolved gas is given by Fick's second law. To obtain it, it is necessary to introduce the continuity equation

$$\nabla \cdot \boldsymbol{J} = -\frac{\partial c}{\partial t}, \tag{2.1.4}$$

which follows from the conservation of mass. We can calculate the gradient of the flux using Fick's first law:

$$\nabla \cdot \boldsymbol{J} = -\nabla \cdot (D\nabla c) = -\nabla D \cdot \nabla c - D\nabla^2 c \tag{2.1.5}$$

If D is uniform, $\nabla D = 0$ and we can obtain Fick's second law by combining the two equations above:

$$\frac{\partial c}{\partial t} = D\nabla^2 c \tag{2.1.6}$$

Or, restricting to the x axis,

$$\frac{\partial c}{\partial t} = D\frac{\partial^2 c}{\partial x^2} \tag{2.1.7}$$

2.1.3. Permeation. We will now apply all the above results to the process of diffusion of gases through a dense membrane, down a concentration gradient. We will first discuss the simplest case of a rubbery polymer membrane, since glassy polymers need some further remarks that will be discussed later in this chapter.

In gas separation, a gas mixture at pressure p_{HPS} is applied to the feed side (HPS) of the membrane, while on the other side permeated gas at pressure $p_{\mathrm{LPS}} \ll p_{\mathrm{HPS}}$ is removed. To a first approximation, we can discuss the situation in which only one gas is present, thus neglecting the influence of other gases on the diffusion of the component under study. There are two interfaces to be considered: the gas-membrane interface at $x = 0$ and the membrane-gas interface at $x = \ell$. Since we are assuming that at these interfaces, equilibrium is immediately reached between the gas and the polymer, Henry's law always applies at both sides of the membrane:

$$c(0) = S\,p_{\mathrm{HPS}} \quad \text{and} \quad c(\ell) = S\,p_{\mathrm{LPS}} \tag{2.1.8}$$

The above equations are the boundary conditions which allow us to solve Fick's second law in stationary transport conditions (stc), i.e. when the gas concentration $c(x)$ does not change in time. In fact, with this hypothesis, equation (2.1.7) becomes

$$D\frac{\partial^2 c}{\partial x^2} = 0 \tag{2.1.9}$$

which can be solved giving the gas concentration profile across the membrane:

$$c(x) = S\,p_{\mathrm{HPS}} + S\frac{p_{\mathrm{LPS}} - p_{\mathrm{HPS}}}{\ell}x \tag{2.1.10}$$

With the above expression for $c(x)$, it is straightforward to solve Fick's first law (equation (2.1.3)), obtaining the flux J^{stc} in stationary transport conditions:

$$J^{\mathrm{stc}} = \frac{D\,S\,\Delta p}{\ell} \tag{2.1.11}$$

with $\Delta p = p_{\mathrm{HPS}} - p_{\mathrm{LPS}} \simeq p_{\mathrm{HPS}}$.

Let us now consider a more general case, in which the gas concentration in the membrane changes in time. We will consider the typical gas permeation experiment, in which the membrane is initially under vacuum and thus the concentration $c(x)$ of dissolved gas is zero throughout the whole membrane. The membrane is exposed to the gas at $t = 0$, so that, for every $t \geq 0$, $c(x = 0) = Sp_{\mathrm{HPS}}$ is constant. The boundary conditions are therefore:

$$\begin{aligned} &c(x = 0, t < 0) = 0 && c(x = \ell, t < 0) = 0 \\ &c(x = 0, t \geq 0) = Sp_{\mathrm{HPS}} && c(x = \ell, t \geq 0) = Sp_{\mathrm{LPS}} \simeq 0 \end{aligned} \tag{2.1.12}$$

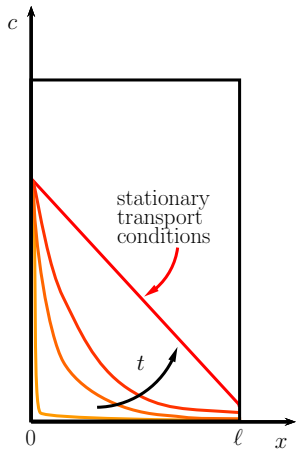

FIGURE 1. A qualitative plot of the permeant concentration throughout the membrane at different times. The color of the curve shifts for increasing time from orange to red.

With these conditions, Fick's equations can be solved giving the flux of the gas emerging from the downstream surface of the membrane, $J(t) = -D(\partial c/\partial x)_{x=\ell}$ (Crank, 1979):

$$J(t) = \frac{D\,S\,p_{\mathrm{HPS}}}{\ell}\left[1 + 2\sum_{n=1}^{\infty}(-1)^n \exp\left(-\frac{D\,n^2\,\pi^2\,t}{\ell^2}\right)\right]. \tag{2.1.13}$$

From a phenomenological point of view, we can say that at $t = 0$, gas starts dissolving in the membrane's first layers. Its concentration increases with time in the bulk of the membrane and for $t \to \infty$, the system reaches stationary transport conditions, in which c depends linearly on x. A graphical representation of the concentration profiles $c(x)$ in a membrane at different times t is given in Figure 1.

From equation (2.1.13) we can observe in fact that, for $t = 0$, $J(t) = 0$ and that for $t \to \infty$ the flux becomes constant and we obtain again equation (2.1.11). The permeability [1] P of a membrane is defined as the gas flux J^{stc} normalized by the trans-membrane pressure Δp and its thickness ℓ:

$$P = J^{\mathrm{stc}}\frac{\ell}{\Delta p} \tag{2.1.15}$$

From equations (2.1.11) and (2.1.15), it is clear that this quantity equals the product of solubility and diffusion coefficient:

$$P = SD. \tag{2.1.16}$$

[1] Permeability is usually expressed in barrer or in $[\mathrm{ml(STP)\,\mu m\,m^{-2}\,day^{-1}\,kPa^{-1}}]$ (Li and Chung, 2008):

$$1\,\mathrm{barrer} := 10^{-10}\,\frac{\mathrm{ml(STP)\,cm}}{\mathrm{cm^2\,s\,cmHg}} = 6.48\times10^{-2}\,\frac{\mathrm{ml(STP)\,\mu m}}{\mathrm{m^2\,day\,kPa}} = 3.35\times10^{-16}\,\frac{\mathrm{mol}}{\mathrm{m\,s\,Pa}} \tag{2.1.14}$$

Often, the dynamics of permeation are expressed in terms of the quantity $Q(t)$ of gas permeated through a membrane of unit area at time t. $Q(t)$ is the integral of $J(t)$: $Q(t) = \int_0^t J(\tau)d\tau$.

$$Q(t) = \frac{D\,S\,p_{\mathrm{HPS}}}{\ell}\left(t - \frac{\ell^2}{6\,D}\right) - 2\frac{\ell\,S\,\Delta p}{\pi^2}\sum_{n=1}^{\infty}\frac{(-1)^n}{n^2}\exp\left(-\frac{D\,n^2\,\pi^2\,t}{\ell^2}\right). \quad (2.1.17)$$

Typical plots for $J(t)$ and $Q(t)$ are shown in Figure (2). The $Q(t)$ curve can be

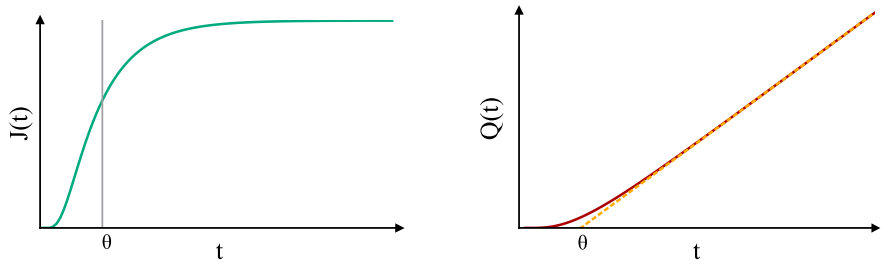

(a) (b)

FIGURE 2. Typical curves for gas flux (a) and quantity of permeated gas (b) as functions of time. The dashed line in panel (b) is the fit of the $Q(t)$ curve in stc (i.e. for $t \to \infty$) to a straight line.

thought as being divided in two parts. The first is the transient part, which occurs for $t \lesssim 5\,\theta$, where $\theta = {}^{\ell^2}/_{6D}$ is called timelag and its origin will soon be cleared. During this period of time, the concentration of the gas in the membrane varies until it reaches the stationary conditions (second part, $t \to \infty$), when $Q(t)$ becomes a straight line. Indeed, in stationary transport conditions, equation (2.1.17) simplifies to

$$Q(t) = \frac{D\,S\,p_{\mathrm{HPS}}}{\ell}\left(t - \frac{\ell^2}{6\,D}\right) = \frac{P p_{\mathrm{HPS}}}{\ell}\,(t - \theta) \quad (2.1.18)$$

which is a straight line which intercepts the time axis at $t = \theta$, see Figure 2. It is now clear that, once $Q(t)$ is measured, the permeability can be obtained from its slope and the diffusion coefficient from θ: this method is called *time lag technique*.

2.1.4. Selectivity. The ability of a membrane to separate a binary mixture of gases 1 and 2 is measured by the membrane's separation factor $\alpha^*_{1/2}$

$$\alpha^*_{1/2} = \frac{{}^{Y_1}/_{Y_2}}{{}^{X_1}/_{X_2}}, \quad (2.1.19)$$

where X_i and Y_i are the mole fractions of gas i in the retentate stream (at the upstream side) and in the permeate stream (at the downstream side), respectively.

In can be shown that, when the downstream pressure is negligible with respect to the upstream pressure, the separation factor can be expressed as the ratio between the permeabilities P_1 and P_2 (Ghosal and Freeman, 1994):

$$\alpha_{1/2} = \frac{P_1}{P_2} \tag{2.1.20}$$

It is worth to note that, in the general case, for a given membrane, the permeability P_i measured by single-component permeation measurements can differ from the permeability P_i^* measured when i is a component in a gas mixture. In general, in fact, the presence of other gases can influence the permeability of the membrane to gas i, for example by inducing plasticization of the membrane material (Baker, 2004; Baker and Low, 2014).

Using equation (2.1.20) and remembering equation (2.1.16), one can write

$$\alpha_{1/2} = \frac{S_1}{S_2} \cdot \frac{D_1}{D_2}, \tag{2.1.21}$$

The first term on the right-hand side of the above equation is called solubility selectivity, whereas the second term is called diffusivity selectivity.

2.1.5. Glassy polymers. For the sake of completeness, we will now describe some peculiarities of permeation in glassy polymers. For glassy polymers, sorption isotherms are usually different from what is observed in the case of rubbery polymers. In fact, one finds that the sorption isotherms for glassy polymers are steeper for low gas pressures and have a negative second derivative. This behavior is explained in the dual sorption model. The basic assumption of this model is that gas sorption in a polymer can occur in two kinds of sites. In rubbery polymers, molecules are dissolved in the polymer matrix, filling the equilibrium free volume of the polymer itself (we will call the concentration due to this contribution c_D, dissolved). In glassy polymers there is another contribution. These polymers are characterized by the presence of non-equilibrium free volumes (also called unrelaxed volumes), in which the permeant packs with liquid-like density. We will refer to the concentration of this part of the permeant as c_H, where H stands for "holes". Thus, the isotherms are described by the sum of two terms: the Henry term resembles the behavior described by equation (2.1.1), while the so-called Langmuir term describes condensation of the permeant in non-equilibrium free volumes.

$$c = c_\mathrm{D} + c_\mathrm{H} = k_\mathrm{D}\, p + \frac{c'_\mathrm{H}\, b\, p}{1 + b\, p} \tag{2.1.22}$$

where k_D, c'_H and b are parameters of the model. k_D is the proportionality coefficient for the Henry term, it is analogous to solubility in the case of rubbery polymers. c'_H is called hole saturation constant and b is called hole affinity constant (Baker, 2004; Vieth, 1991; Paul, 2010). A qualitative plot of the two contributions is shown in Figure 3.

It is legitimate to expect that, as in the case of sorption, even diffusion occurs in different ways. We can thus write the flux as a sum of two components:

$$J = -D_\mathrm{D} \frac{\partial c_\mathrm{D}}{\partial x} - D_\mathrm{H} \frac{\partial c_\mathrm{H}}{\partial x} \tag{2.1.23}$$

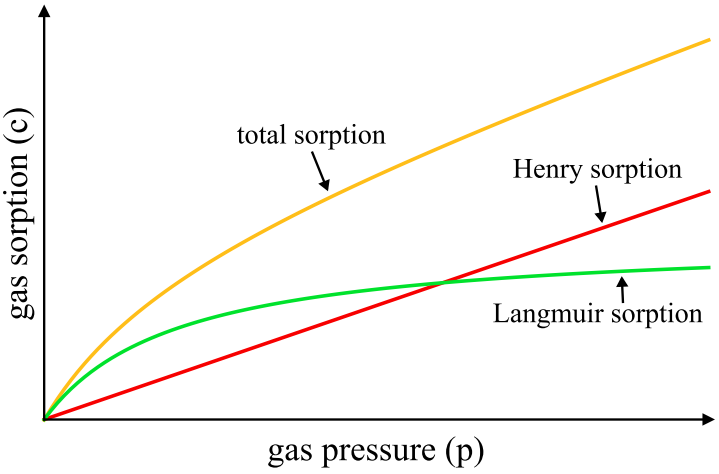

FIGURE 3. An illustration of the two contributions to sorption in a glassy polymer.

We now want to express permeation from the point of view of the two different populations D and H of permeant molecules. Starting from equation (2.1.22) we define solubilities the parameters that connect pressure to the concentrations c_{D} and c_{H}:

$$S_{\mathrm{D}} = \frac{c_{\mathrm{D}}}{p_{\mathrm{HPS}}} = k_{\mathrm{D}} \quad \text{and} \quad S_{\mathrm{H}} = \frac{c_{\mathrm{H}}}{p_{\mathrm{HPS}}} = \frac{c'_{\mathrm{H}}\, b}{1 + b\, p_{\mathrm{HPS}}} \tag{2.1.24}$$

Assuming the downstream pressure to be zero, permeability can be expressed in the following way:

$$P = S_{\mathrm{D}}\, D_{\mathrm{D}} + S_{\mathrm{H}}\, D_{\mathrm{H}} = k_{\mathrm{D}}\, D_{\mathrm{D}} \left(1 + \frac{FK}{1 + b\, p_{\mathrm{HPS}}}\right) \tag{2.1.25}$$

where $F = {}^{D_{\mathrm{H}}}/_{D_{\mathrm{D}}}$ and $K = {}^{c'_{\mathrm{H}} b}/_{k_{\mathrm{D}}}$ (Paul, 2010). From the above equation, it is clear that in glassy polymers permeability decreases with increasing pressure (although flux is still an increasing function of p_{HPS}). We point out however that, at the low pressures used for the experiments carried out in this thesis work, linear sorption isotherms were always observed and penetrant condensation in unrelaxed volumes was never detected.

2.1.6. Temperature dependence of S and D. We will see in section 2.3 that the dependence of diffusivity on temperature can be quite complicated, because D depends on the temperature through the free volume. Nevertheless, the temperature dependence of the diffusion coefficient can be described in the following way:

$$D = D_0 \exp\left(\frac{-E_D}{RT}\right) \tag{2.1.26}$$

where D_0 is a pre-exponential factor, E_D is an apparent activation energy for diffusion, R is the gas constant and T is the temperature. According to the "zone theory" for diffusion by Barrer, the activation energy E_D corresponds to the energy needed to create an "activated zone" near to the penetrant molecule, allowing it to take a diffusive jump. According to Meares (1954), the activation energy is proportional to the polymer's cohesive energy density and to the volume of the activated state, i.e. to the square of the penetrant's kinetic diameter multiplied by the jump length (Freeman, 1999; Zheng et al., 2007).

Solubility has a thermally activated behavior described by the relation

$$S = S_0 \exp\left(\frac{-\Delta H_S}{RT}\right) \tag{2.1.27}$$

where ΔH_S is the enthalpy of solution (or enthalpy of sorption) of the penetrant in the polymer while S_0 is a temperature-independent pre-exponential factor. the enthalpy of solution is given as the sum of two terms:

$$\Delta H_S = \Delta H_C + \Delta H_M \,, \tag{2.1.28}$$

where ΔH_C is the enthalpy of condensation of gas into liquid phase and ΔH_{M} is the enthalpy of mixing (Matteucci et al., 2006). Condensation is an exothermic process ($\Delta H_{\mathrm{C}} < 0$) and the enthalpy of condensation ΔH_{C} is related to the enthalpy of vaporization by the relation $\Delta H_{\mathrm{C}} = -\Delta H_{\mathrm{V}}$. From $P = DS$ one easily obtains a similar formula for the dependence of permeability on temperature.

$$P = D_0\, S_0\, \exp\left(-\frac{E_D + \Delta H_S}{RT}\right) = P_0\, \exp\left(\frac{-E_P}{RT}\right) \tag{2.1.29}$$

where P_0 is still a temperature-independent pre-exponential factor and E_P is the apparent activation energy for permeation.

2.2. Permeation at a microscopic level

In this section, we will start from the laws governing gas solution and gas diffusion in polymers, to understand in more detail the phenomena underlying gas transport in polymer membranes at a microscopic level. We will describe the process in analogy with the treatment proposed by Wang (1936) for metals, by separating in the following steps the sorption and desorption of gas molecules at the surfaces:

(1) the gas molecules collide on the surface of the membrane and get adsorbed;
(2) the opposite process can also happen, and gas molecules desorb from the surface of the membrane;
(3) gas molecules adsorbed on the surface of the membrane get absorbed to the membrane bulk;
(4) the opposite of the point (3) occurs, gas molecules pass from the bulk to the surface of the membrane.

The gas flow J^{ads} described by the process of point (1) is given by

$$J^{\text{ads}} = \alpha_m(1-\vartheta)\mu p \tag{2.2.1}$$

where α_m is the adsorption probability of the incident molecules, ϑ is the effective fractional surface coverage, defined in analogy with the case of gas adsorption on metals, p is the pressure of the gas in contact with the membrane surface and $\mu = (2\pi M k_{\text{B}} T_M)^{-1/2}$, so that μp is the number of gas molecules colliding on a unit surface per unit time. In the definition of μ, k_{B} is Boltzmann's constant, T_M is the gas temperature and M is the molecular mass of the gas.

The desorption flux J^{des} described by the above point (2) is

$$J^{\text{des}} = \delta\vartheta \tag{2.2.2}$$

where δ is the rate constant for desorption. The gas flow for molecules passing from the surface to the bulk (J^{abs}) and vice-versa (J^{dsb}) are given by

$$J^{\text{abs}} = \gamma\vartheta \tag{2.2.3}$$

and

$$J^{\text{dsb}} = \beta(1-\vartheta)c \tag{2.2.4}$$

where γ and β are proportionality constants and we remark that the concentration c is that of the gas dissolved in the membrane material in close vicinity to the surface.

The processes just described occur both at the HPS surface of the membrane, in contact with gas at pressure p_{HPS}, and at the Low Pressure Side of the membrane, in contact with gas at the pressure p_{LPS}. Since in the most common experimental conditions $p_{\text{LPS}} \ll p_{\text{HPS}}$, we will assume $p_{\text{LPS}} = 0$ in the following.

Inside the bulk of the membrane, the diffusion J^{d} of gas molecules obeys Fick's first law given by equation 2.1.3. The process is schematically represented in Figure 4. In stationary transport conditions, the gas flux J^{stc} through the membrane is constant in time and uniform (it does not depend on x). Therefore, we can describe the processes depicted in Figure 4 with the following equations:

$$\begin{array}{rcrcll}
J^{\text{stc}} & = & J_u^{\text{ads}} - J_u^{\text{des}} & = & \alpha_m(1-\vartheta_u)\mu p_{\text{HPS}} - \delta\vartheta_u & \text{(HPS, adsorption)} \\
J^{\text{stc}} & = & J_u^{\text{abs}} - J_u^{\text{dsb}} & = & \gamma\vartheta_u - \beta(1-\vartheta_u)c_u & \text{(HPS, absorption)} \\
J^{\text{stc}} & = & J^{\text{d}} & = & -D\frac{c_d - c_u}{\ell} & \text{(bulk)} \\
J^{\text{stc}} & = & J_d^{\text{dsb}} - J_d^{\text{abs}} & = & \beta(1-\vartheta_d)c_d - \gamma\vartheta_d & \text{(LPS, absorption)} \\
J^{\text{stc}} & = & J_d^{\text{des}} - J_d^{\text{ads}} & = & \delta\vartheta_d & \text{(LPS, adsorption)}
\end{array} \tag{2.2.5}$$

where we used the index u for the parameters relative to upstream side of the membrane and the index d for the downstream side. In the last equation of the system, we neglected the term $J^{\text{ads}} = \alpha_m(1-\vartheta_d)\mu p_{\text{LPS}}$ because we are assuming

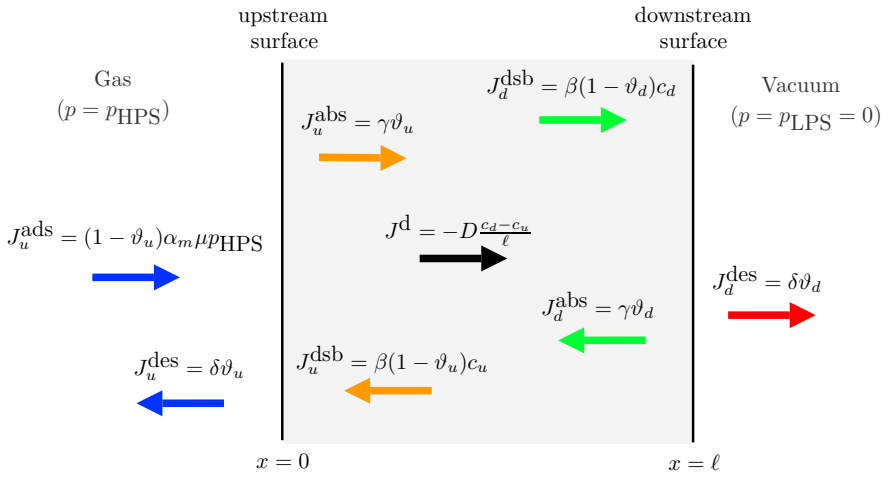

FIGURE 4. Schematic representation of the different contributions to gas flux in a polymeric membrane.

$p_{\mathrm{LPS}} = 0$. The above system of equations can be solved giving

$$\alpha_m \mu p_{\mathrm{HPS}} = \frac{2\delta J^{\mathrm{stc}}(\gamma+\delta) - \frac{\ell\beta}{D} J^{\mathrm{stc}}(J^{\mathrm{stc}}+\delta)(J^{\mathrm{stc}}-\delta)}{(J^{\mathrm{stc}}-\delta)(J^{\mathrm{stc}}-\gamma)} \tag{2.2.6}$$

The above equation makes it clear that the flux J^{stc} remains finite also for infinite pressures p_{HPS}. Indeed, the pressure increases with increasing J^{stc} but it diverges when J^{stc} approaches γ or δ, whichever is smaller. From a physical point of view, the fact that J^{stc} has to be smaller than γ means that the gas molecules can only get absorbed in the bulk of the membrane at a finite rate, whereas the meaning of the limit $J^{\mathrm{stc}} < \delta$ is given by the last equation of system (2.2.5): the effective surface coverage ϑ_d cannot be larger than 1.

Let us now assume the flux J^{stc} to be much smaller than both δ and γ, so that it can be neglected when compared to them. In this case, equation (2.2.6) becomes

$$\alpha_m \mu p_{\mathrm{HPS}} = J^{\mathrm{stc}} \left[\frac{2(\gamma+\delta)}{\gamma} + \frac{\ell\beta}{D}\frac{\delta}{\gamma} \right] \tag{2.2.7}$$

which can be rewritten as

$$J^{\mathrm{stc}} = \frac{\frac{D}{\ell}\alpha_m \mu p_{\mathrm{HPS}}}{\frac{\beta}{\gamma}\left[\delta + 2\frac{D}{\ell\beta}(\gamma+\delta)\right]} \tag{2.2.8}$$

If the membrane is thick enough, so that $\frac{D}{\ell\beta}$ becomes negligible, the above equation becomes

$$J^{\mathrm{stc}} = \frac{D}{\ell}\frac{\gamma}{\beta\delta}\alpha_m \mu p_{\mathrm{HPS}} \tag{2.2.9}$$

We see from the above equations that, for $J^{\mathrm{stc}} \ll \gamma$ and $J^{\mathrm{stc}} \ll \delta$, the gas flux is directly proportional to the upstream pressure p_{HPS}. From equation (2.2.9), we can

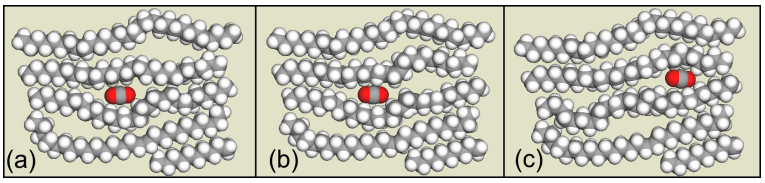

FIGURE 5. Diffusion of gas molecules in amorphous polymers: the molecule occupies a nanocavity (a) until a new one forms adjacent to the diffusing molecule, by means of thermal fluctuations of the polymer matrix (b). When this happens, the molecule can jump to the new nanocavity (c).

also obtain an expression of the solubility S which highlights the role of microscopic phenomena involved in gas sorption:

$$S = \frac{\gamma}{\beta\delta}\alpha_m\mu \tag{2.2.10}$$

2.3. Gas transport and free volumes in polymers

In this section a model will be introduced, which describes the correlation between permeant diffusion and the structure of the polymer. This approach is based on the concept of *free volume*, i.e. the volume of the polymer that is not occupied by polymer chains and can therefore be occupied by the diffusing molecules.

2.3.1. Diffusion through free volumes. According to the free volume theory, motion of molecules in the volume of a polymer occurs through jumps between thermally generated nanovoids in the polymer matrix. Diffusing molecules occupy small cavities between polymer chains, in which they can move over distances smaller than the diameter of the cavity itself. These cavities are called free volume elements (FVE) or "holes". Due to chance thermal motions of the polymer chains, free volume elements continuously form and disappear. When a nanovoid forms adjacent to the diffusing molecule and is large enough to contain it, the molecule can jump into it, where it will remain until another favorable polymer chain thermal motion occurs. The process has been represented in Figure 5. The sum of all the voids in an amorphous polymer is called free volume, as opposed to occupied (by the polymer chains) volume. Molecule diffusivity depends both on the size of the gas molecule and on the total amount of volume available for diffusion (Duda and Zielinski, 1996).

A first model for transport regulated by free volumes has been developed by Cohen and Turnbull (1959). Although their model was initially believed to be suitable only for liquids that can be considered as composed by rigid spheres, the greatest impact of their development has been on describing mass transfer in solutions consisting of long polymer chains mixed with small solvent molecules. In the Cohen-Turnbull model, the liquid is assumed as composed by N molecules, each of

them having volume V^*. The free volume elements are continuously redistributed in the liquid. The average free volume per sphere is given by V^{f}, so that the total volume of the liquid is $V_{\mathrm{L}} = N\,V^* + N\,V^{\mathrm{f}}$. In this case, the self diffusion rate of a hard sphere is proportional to the probability to find a hole of volume V^* or larger adjacent to the sphere. Cohen and Turnbull estimated this probability, finding the following expression for the self-diffusion coefficient:

$$D = A_{\mathrm{g}}\,\exp\left(-\gamma_{\mathrm{of}}\frac{V^*}{V^{\mathrm{f}}}\right) \tag{2.3.1}$$

where A_{g} is a constant related to the gas kinetic velocity, γ_{of} is an overlap factor between 0.5 and 1.0 which prevents double counting of free volume elements (i.e., free volumes shared by adjacent molecules) and V^* is the minimal hole size in which the diffusing molecule can jump Duda and Zielinski (1996).

Vrentas and Duda started from the Cohen-Turnbull theory for self diffusion to develop a model describing diffusion in polymers. They assumed that the volume occupied by a polymer can be ideally divided in three parts: core volume, interstitial free volume and hole free volume. The core volume is that occupied by the polymer chains, it is also called occupied volume. The interstitial free volume requires a large redistribution energy and is not implicated in diffusion. The hole free volume, on the opposite, is easily redistributed by thermal fluctuations and it determines the transport properties of the polymer system. To extend the Cohen Turnbull model for self diffusion in liquids to the case of diffusion in polymers, Vrentas and Duda introduced the concept of jumping unit, which allowed to take into account the fact that polymer chain motion occurs stepwise, through the motion of one segment (jumping unit) at a time (Duda and Zielinski, 1996). This means that not only the size of the diffusing molecule, but also the size of the polymer's jumping units determines the diffusion coefficient.

A further modification to the model of Cohen and Turnbull was proposed by Macedo and Litovitz (1965) and Chung (1996), who suggested that jumping units and diffusing molecules need to overcome an energy barrier to take a diffusive step, meaning that the sole presence of a neighboring free volume element with sufficient size is not enough. The diffusing molecule needs in fact to overcome the attractive forces with adjoining groups prior to take a diffusive step. This condition is implemented in the dependence of the pre-exponential factor on temperature.

At this point, it was necessary to give an expression of the binary mutual diffusion coefficient instead of the self diffusion coefficient. The binary mutual diffusion coefficient D^{∞} for an infinitely diluted penetrant in a polymer can be obtained using an approximated relation connecting self-diffusion coefficient and mutual binary diffusion coefficient. Nevertheless, if the gas sorption isotherm in the polymer is linear (as in the case of low gas concentration in rubbery polymers), the self diffusion coefficient equals the mutual diffusion coefficient (Ganesh et al.,

1992). With these considerations, the diffusivity for an infinitely diluted gas in a polymer can be written (Lv et al., 2009):

$$D^{\infty} = D_0 \exp\left(-\frac{E^*}{RT}\right) \exp\left(-\frac{\xi \hat{V}_2^*}{\hat{V}_{\mathrm{FH}}}\right) \tag{2.3.2}$$

where D_0 is a pre-exponential factor whose dependence on temperature is much weaker than that of the exponential terms (Macedo and Litovitz, 1965; Ricci et al., 1977), E^* is a measure of the activation energy the molecule needs to get free from the interaction with neighboring polymeric groups, $\hat{V}_2^*$ is the specific hole free volume needed for a diffusive step of a jumping unit of the polymer, $\hat{V}_{\mathrm{FH}}$ is the specific hole free volume of the polymer and ξ is the ratio of the critical molar free volume required for a diffusive step of the diffusant to that for a diffusive step of a polymer jumping unit. E^* is usually very small and it can often be considered zero to a first approximation (Vrentas and Vrentas, 1989). It should be noted that the above equation is a simplified version, obtained for infinite dilution, of the expression for the mutual binary diffusion coefficient for the system under investigation. For a more detailed treatment, see (Duda and Zielinski, 1996).

Equation (2.3.2) is often expressed in a simplified form (Lin and Freeman, 2006; Lin et al., 2007; Thornton et al., 2009):

$$D = A_D \exp\left(-\frac{B_D}{f}\right) \tag{2.3.3}$$

where A_D and B_D can be considered independent of temperature and penetrant concentration. A_D depends on the diffusant's volume and shape, B_D is proportional to the ratio between the penetrant molecule's volume and the minimum volume of the FVE required for the displacement of a polymer jumping unit. B_D is expected to decrease with the size of the penetrant molecules and the chain stiffness (Thran et al., 1999; Vrentas and Duda, 1977). f is the fractional free volume, defined as the ratio between the specific free volume V_{F} and the macroscopic specific volume V of the polymer:

$$f = \frac{V_{\mathrm{F}}}{V} = \frac{V - V_{\mathrm{o}}}{V} \tag{2.3.4}$$

where the specific free volume $V_{\mathrm{F}} = V - V_{\mathrm{o}}$, i.e. as the difference between the specific volume of the polymer and the specific volume V_{o} occupied by the polymer chains (Lee, 1980; Matteucci et al., 2006).

2.3.2. Free volume in glassy and rubbery polymers. It is found that fractional free volume is typically larger for glassy polymers than for rubbery polymers. We can try to understand this by analyzing the structure of a polymer above and below its glass transition temperature T_g. Above T_g, the polymer is in its rubbery state: polymer chains are relatively free to move and free volume originates from their imperfect packing. In rubbery state, hole free volume gives

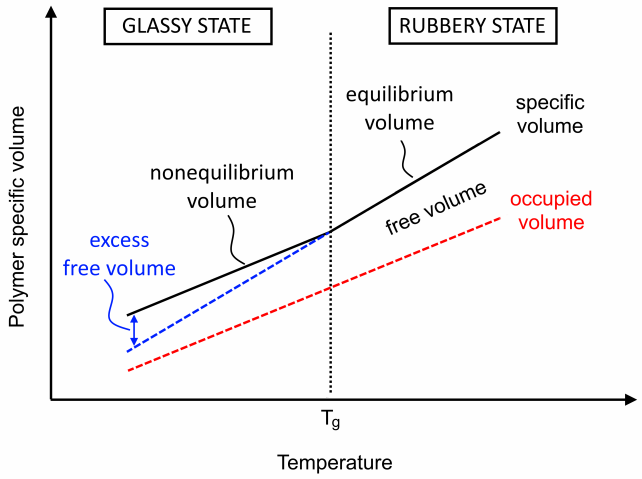

FIGURE 6. The different contributions to a polymer's volume as a function of temperature.

a large contribution to the total free volume. Free volume decreases with decreasing temperature until T_g is reached (see Figure 6). Cooling the polymer below its glass transition temperature "freezes" the polymer chains, which can no longer rotate freely. Because of the greatly reduced mobility of the polymer chains, the free volume elements are also frozen into the polymer matrix: excess free volume elements are therefore trapped in the polymer volume and the polymer is not in an equilibrium state. The magnitude of the excess free volume in the glassy state depends on how fast the polymer is cooled from the rubbery to the glassy phase (Ganesh et al., 1992). As the temperature is further reduced, the voids between polymer chains remain approximately the same, while occupied volume decreases due to the reduced amplitude of vibration of the elements composing the chains (Baker, 2004). At this point, it is necessary to note that, although the density fluctuations of a glassy polymer are strongly reduced with respect to that of a rubber, they are not completely eliminated. On much longer timescales, free volumes redistribute also in glassy polymers, which reach equilibrium undergoing a densification process (also referred to as *aging* of the polymer) in which the material reaches equilibrium and loses the excess free volume. This process occurs usually in the timescale of weeks to years and depends also on the size and shape of the polymer sample (Duda and Zielinski, 1996; Huang and Paul, 2007).

2.4. Diffusion in porous membranes

In the previous sections, we have described the diffusion mechanism for a gas molecule dissolved in a polymer. In the case of diffusion in a porous membrane,

the gas molecules are contained in fixed pores and do not enter the bulk of the membrane material. In the following, we will discuss the two transport mechanisms of interest for this thesis, i.e. those which occur when the size of the pore is smaller than the gas molecules' mean free path.

2.4.1. Knudsen diffusion. Knudsen diffusion occurs when the kinetic diameter σ_k of the diffusing molecule is smaller than the diameter d_c of the pore ($\sigma_k/d_c \lesssim 0.5$) Xiao and Wei (1992). In Knudsen diffusion, molecules move in vacuum with their thermal velocity given by

$$u = \sqrt{\frac{8k_B T}{\pi M}} \tag{2.4.1}$$

where M is the molecular weight of the penetrant. When molecules collide with the pore's wall, they are assumed to be momentarily adsorbed on the surface and to subsequently leave it in a completely random direction.

In these assumptions, and if the pores can be approximated with infinitely long cylindrical channels with radius d_c, then the Knudsen diffusivity is given by Burganos (2010)

$$D_K = \frac{1}{3} u d_c \tag{2.4.2}$$

We note that Knudsen diffusivity is not thermally activated. In fact, it depends on the square root of the temperature. The dependence of D_K on the square root of the gas molecular mass M is the basis for gas separation in membranes through which transport occurs in Knudsen regime (this relation is called Graham's law for diffusion (Baker, 2004)).

2.4.2. Configurational diffusion. Configurational diffusion occurs when the size of the pore is similar to that of the diffusant. It is thermally activated and occurs when the diffusing molecules, inside the pores, lose their gaseous state and adsorb on the pores' surface, vibrating harmonically (with frequency ν) in equilibrium positions in potential wells given by the interaction with the surface. When the gas molecules accumulate enough energy to surpass the potential well (which is much higher than $k_B T$), they can jump to one of the neighboring sites. In this model, assuming that the gas concentration is low and the adsorbed molecules do not interact with each other, the diffusivity is given by (Xiao and Wei, 1992; Gavalas, 2006):

$$D_{conf} = \frac{1}{z} \nu l_s^2 \exp\left(\frac{-E_D}{k_B T}\right) \tag{2.4.3}$$

In the above equation, z is the coordination number, i.e. the number of sites adjacent to the one in which the molecule resides; l_s is the distance between adjacent sites and E_D is the activation energy (i.e. the depth of the potential well).

CHAPTER 3

Materials

For the present thesis work, the following materials were studied:

(1) amine-modified epoxy resins;
(2) nanocomposites consisting of Few Layer Graphene (FLG) nanoplatelets dispersed in an epoxy resin;
(3) nanocellulose films and nanocellulose films with dispersed TiO_2 nanoparticles, deposited on polylactic acid (PLA) supports.

The epoxy and epoxy nanocomposite membranes were prepared by the author of this thesis, whereas the nanocellulose-based membranes were prepared by the Nanolab Research Group of the Department of Physics of the University of Trento.

Samples (1) are a set of four epoxy resin membranes in which the crosslink density was systematically varied by using crosslinkers with different polymeric chain length. The crosslink density is expected to be correlated with the free volume structure of the material. In this study, we used such a set of samples to study this correlation as well as the role of free volume on the gas transport properties of the epoxy resins.

Samples (2) are FLG nanocomposites based on one of the epoxy resins of the above described set. A set of nanocomposite membranes was prepared with different filler loadings, to study their gas barrier properties and the influence of the matrix-filler interface structure on gas transport.

Samples (3) are nanocellulose-based membranes. Nanocellulose is a highly crystalline material well known to have excellent barrier properties. Nevertheless, the specific mechanism underlying gas diffusion in such material is still unknown. This mechanism was the topic of the study, carried out using sets of samples with different thicknesses. Moreover, nanocellulose membranes with dispersed TiO_2 nanoparticles were prepared to study the influence of the fillers on the properties of the membranes.

In this chapter, we will only describe the sample preparation procedure and the results of their structural characterization, whereas experiments and results on the free volume structure and gas transport properties of the membranes will be described and discussed in specific chapters.

In appendix A, we will separately present a work on polypropylene/multiwalled carbon nanotube composite samples carried out in the framework of a collaboration with the Institute of Chemical Engineering Sciences, Foundation for Research and

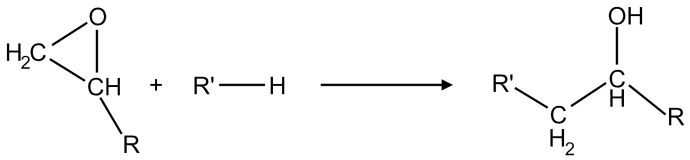

FIGURE 1. The curing reaction between an epoxide and a crosslinker.

Technology-Hellas, (Patras, Greece) and the departments of Chemistry and Chemical Engineering of the University of Patras (Greece). Preparation and structural characterization of the samples, as well as their gas transport properties, will be all discussed in appendix A.

3.1. Epoxy resins

Epoxy resins are crosslinked polymers obtained from the reaction of two components, called epoxide and crosslinker, the latter also being called hardener or curing agent. The epoxide is a molecule that contains a cyclic ether (epoxide or oxirane group), as shown in the leftmost part of Figure 1. The crosslinker is a molecule with groups able to react with the epoxide functional group, usually hydroxy groups or primary and secondary amines (Ebewele, 2000). The polymerization process consists in opening the epoxide group and bonding with the crosslinker's amine or hydroxy group as shown in Figure 1 (Mack and Smith, 2005).

For the preparation of the samples used in this study, we used diamine crosslinkers. There are two important quantities which characterize the reagents needed for the preparation of such epoxy resins: epoxides are characterized by the epoxy equivalent weight (EEW), defined as the quantity of epoxide (grams) containing one equivalent of epoxide groups; amine crosslinkers are characterized by the amine hydrogen equivalent weight (AHEW), i.e. the quantity of crosslinker that contains one equivalent of N-H groups (molecular weight of the hardener divided by the number of active hydrogens per molecule).

The polymer is prepared by mixing epoxide and amine in the correct proportions and submitting the obtained solution to a heat treatment. A completely crosslinked resin is obtained when the ratio between crosslinker and epoxide equals the ratio AHEW/EEW (Hoa, 2009).

3.1.1. Epoxy membrane preparation. The epoxy resins used in this work are based on an aliphatic epoxide, NeoPentyl Glycol Diclycidyl Ether (NPGDE, molecular weight=216 g/mol, EEW 145 g/eq.) purchased from Sigma Aldrich Srl (Italy). We used four crosslinkers with different chain length, in order to systematically vary the crosslink density (number of crosslink sites per unit volume)

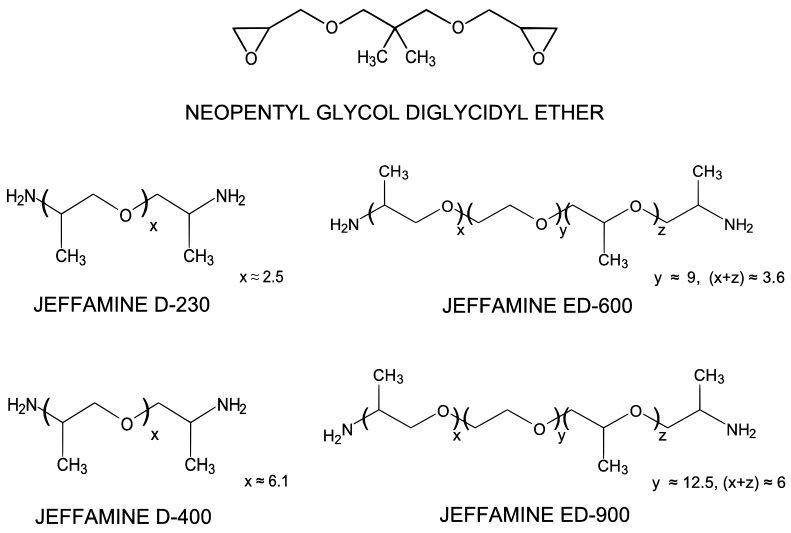

FIGURE 2. Chemical structures the epoxy neopentyl glycol diglycidyl ether and polyether diamines.

of the epoxy resins and hence tune their free volume structure. The used crosslinkers were: α, α-diamino terminated polyoxypropylene polyether diamines Jeffamine D-230 (molecular weight = 230 g/mol, AHEW = 59 g/eq.), D-400 (molecular weight = 400 g/mol, AHEW = 107 g/eq.) and α, α-diamino terminated poly(oxypropylene)-block-poly(oxyethylene)-block-poly(oxypropylene) triblock polyether diamines including Jeffamine ED-600 (molecular weight = 600 g/mol, AHEW = 156 g/eq.) and Jeffamine ED-900 (molecular weight = 900 g/mol, AHEW = 220 g/eq.), procured from Huntsman Chemical Co. The chemical structures of the epoxide and the polyether diamines are shown in Figure 2. The epoxy and amine hydrogen equivalent weights have been determined from standard titrimetry methods (Durbetaki, 1956).

To prepare the membrane samples, NPGDE and the amines have been weighed and mixed in stoichiometric proportions to obtain a 1:1 ratio between the number of epoxide groups and amine hydrogens, as described above, and vigorously hand-stirred for at least 10 minutes, to get a homogeneous mixture. Samples with thickness of the order of 0.1 mm were obtained by casting the mixture on a glass surface, whereas samples with thickness $\gtrsim 0.5$ mm were prepared in stainless steel molds.

The curing process for all the samples was carried out at 323 K for 4 hours and 353 K for the next 12 hours. In the following, the epoxy-Jeffamine D-230 and epoxy-Jeffamine D-400 will be referred to as NPGD-230 and NPGD-400, respectively,

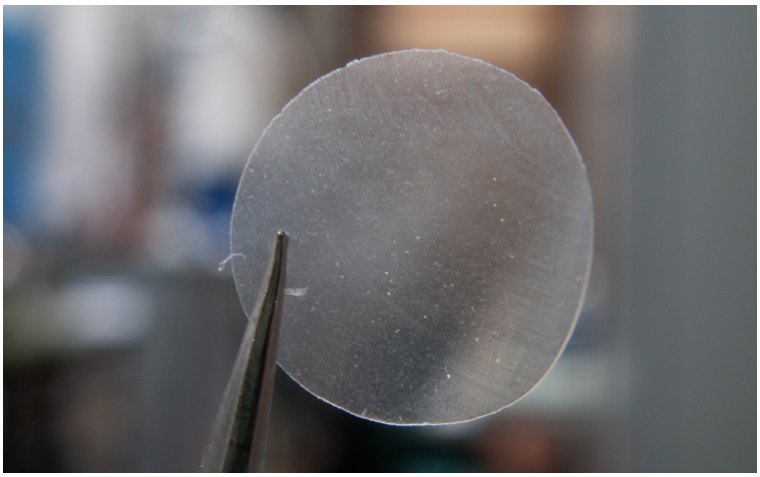

FIGURE 3. Photograph of a cured NPGED-230 membrane sample.

while the epoxy-Jeffamine ED-600 and epoxy-Jeffamine ED-900 will be referred to as respectively NPGED-600 and NPGED-900. The membrane samples for gas transport experiments were prepared in form of disks (18 mm diameter, $\sim 100\,\mu m$ thickness) using a self-designed cutting tool, see Figure 3.

3.1.2. Structural and morphological characterization. The structural and morphological properties of the samples were studied by Fourier Transform InfraRed (FTIR) spectroscopy, Differential Scanning Calorimetry (DSC) and Scanning Electron Microscopy (SEM) analysis. We will also discuss the correlation between structural properties of the materials and their crosslink density X. In completely cured samples, this parameter can be calculated using the following equation (Wang and Zhou, 2002; Patil et al., 2013):

$$X = \varrho \left[\frac{w_1(a-2)}{M_1} + \frac{w_2(b-2)}{M_2} \right] N_A \tag{3.1.1}$$

where ϱ is the mass density of the polymers; w_1 and w_2 are the weight fractions of the epoxide and of the diamines, respectively; a is the functionality of the epoxide and in our case $a = 2$; b is the functionality of the diamines, in our case $b = 4$; N_A is Avogadro's number. The obtained values are $X = 1.67\,\text{sites/nm}^3$ for NPGD-230; $X = 1.42\,\text{sites/nm}^3$ for NPGD-400; $X = 1.15\,\text{sites/nm}^3$ for NPGED-600; $X = 0.90\,\text{sites/nm}^3$ for NPGED-900.

3.1.2.1. *Fourier Transform InfraRed spectroscopy.* Fourier Transform Infrared Spectroscopy analysis was carried out using a Bruker Optics TENSOR 27 instrument in Attenuated Total Reflection mode and spectra were acquired in the 400-4000 cm^{-1} range with a resolution of $4\,\text{cm}^{-1}$. FTIR analysis was performed to verify the complete curing of the samples. To do so, spectra of the pure epoxide and of the polymer samples were compared. Figure 4 shows the spectra acquired for the pure epoxide and all the cured epoxy resins. In Figure 5, the detail of the

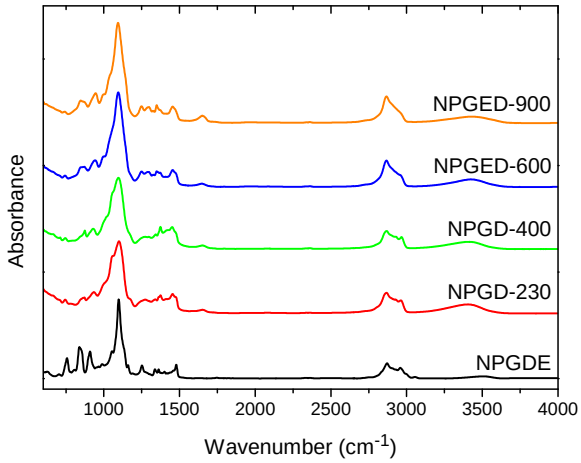

FIGURE 4. FTIR spectra of the NPGDE epoxide and of the cured epoxy samples.

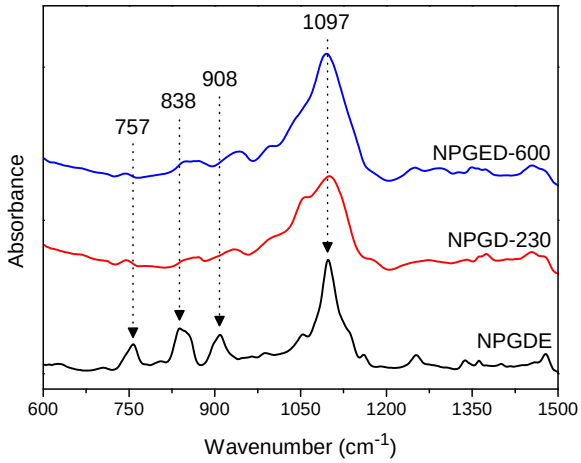

FIGURE 5. FTIR spectra of the pure epoxide and of the cured NPGD-230 and NPGED-600 samples in the 600-1500 cm^{-1} region.

FTIR spectrum of NPGDE, together with those of a high crosslink density sample (NPGD-230) and of a low crosslink density sample (NPGED-600) are reported for the wavelength interval between 600 cm^{-1} and 1500 cm^{-1}. In these spectra, the completeness of the curing process is confirmed by the decrease of the intensity of the peaks at 757 cm^{-1} (rocking -CH_2 of the epoxide group), 838 cm^{-1} (C-O-C stretching of the epoxide group), 908 cm^{-1} (C-O stretching of the epoxide group). The intense peaks at 1097 cm^{-1} present in all samples are attributed to the (C-O-C) stretching of the ethers (Starner, 1997; Gonzàlez et al., 2012). The details of the

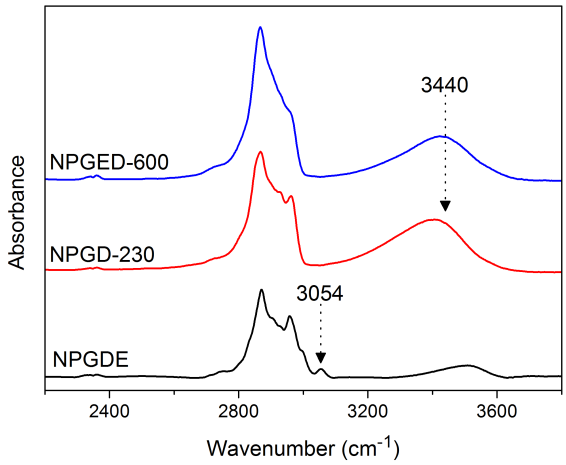

FIGURE 6. FTIR spectra of the pure epoxide and of the cured NPGD-230 and NPGED-600 samples in the 2200-3800 cm^{-1} region.

spectra at higher wavenumbers are reported in Figure 6. The peak at $3054\,\mathrm{cm}^{-1}$ due to C-H stretching in the (-CH_2) of the epoxide group disappears upon curing, confirming the consumption of the epoxide groups despite its low intensity (Gonzàlez et al., 2012). The peaks relative to the amine and hydroxide bonds appearing during the epoxide ring opening reaction are found between 3100 and $3600\,\mathrm{cm}^{-1}$. As often observed, they merge in one broad peak around $3440\,\mathrm{cm}^{-1}$ (Gilbert et al., 1991).

The analysis presented here thus shows that the membrane samples were completely cured, so we can be confident on the correctness of the X values as calculated by equation (3.1.1).

3.1.2.2. *Differential Scanning Calorimetry.* The thermal properties of the polymer samples were analyzed by Differential Scanning Calorimetry (DSC). The employed instrument was a DSC 8500 Hyper-enabled double-furnace Differential Scanning Calorimeter calibrated with an Indium standard. This instrument allows cooling rates up to $750\,\mathrm{K\,min}^{-1}$ and a data readout of 100 points/s. The scans were performed on samples weighting $\sim 6\,\mathrm{g}$ under dry nitrogen atmosphere. Before acquiring the scans, the samples were cooled to their glassy states. The scans were then performed with a heating rate of $5\,\mathrm{K\,min}^{-1}$. An empty DSC pan was taken as a reference in all measurements. DSC analysis was performed to measure the glass transition temperature T_g of the studied epoxy resins and analyze the correlation between the crosslink density X and the glass transition temperature of the cured polymers. Figure 7 shows the DSC scans for all samples and the relative T_g values. The curves show that the T_g decreases with decreasing crosslink density (i.e. with

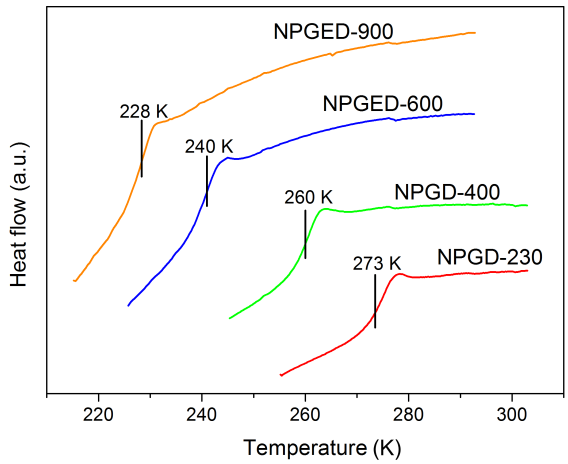

FIGURE 7. DSC scans of the cured samples. For each curve, the respective T_g is reported.

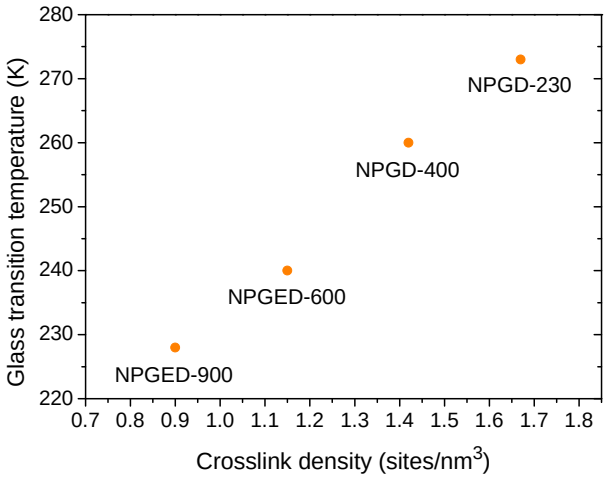

FIGURE 8. Glass transition temperature T_g as measured by DSC as a function of the crosslink density X of the four epoxy resin, as calculated by equation (3.1.1).

increasing chain length of the crosslinker) and that the samples were in rubbery phase at temperatures larger than 273 K.

Figure 8 shows a plot of the glass transition temperature T_g as a function of the crosslink density X of the studied epoxy resin, as detected by DSC analysis. The glass transition temperature shows an almost linear increase with the crosslink density.

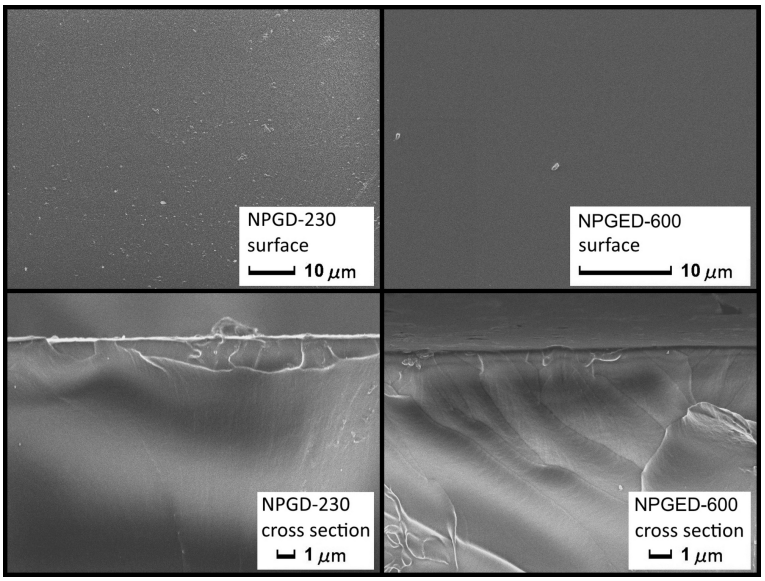

FIGURE 9. Scanning electron micrographs of NPGD-230 and NPGED-600 membranes.

3.1.2.3. *Scanning Electron Microscopy.* The cross-sectional and surface morphology of the epoxy membranes was studied by Scanning Electron Microscopy using a JEOL JSM-7001F Field Emission Scanning Electron Microscope. Cross-sectional images were acquired after cracking the samples in liquid nitrogen. No metallization was needed for the presented low-magnification images. In Figure 9 (upper panels), micrographs of the surface of a high crosslink density membrane (NPGD-230) and of a low crosslink density membrane (NPGED-600) are shown: the micrographs show uniform morphology without specific structures or imperfections such as pinholes or cracks. The cross sections of the same samples, reported in the lower panels of Figure 9, also show uniform morphology. No morphological difference in the surface or in the cross section can been detected in samples with different crosslink density X. A low-magnification micrograph of the cross section of a NPGED-900 membrane is reported in Figure 10: this image shows that the procedure used allows the preparation of samples with uniform thickness.

3.1.2.4. *Thermomechanical analysis.* The volumetric thermal expansion coefficient α_V was measured for all samples using a TA Instruments DMA Q800 under tensile configuration in the temperature range of 273 to 373 K at $6\,\mathrm{K\,s^{-1}}$.

The thermal expansion curves for NPGD-230 and NPGED-600 are reported in Figure 11. The slope of the curves gives the linear thermal expansion coefficient α_L, while α_V is given by $\alpha_V = 3\alpha_L$. The analysis of all samples resulted in indistinguishable values with average $\alpha_V = (5.6 \pm 0.1) \times 10^{-4}\,\mathrm{K}^1$, where the uncertainty is given by the semi dispersion of the values.

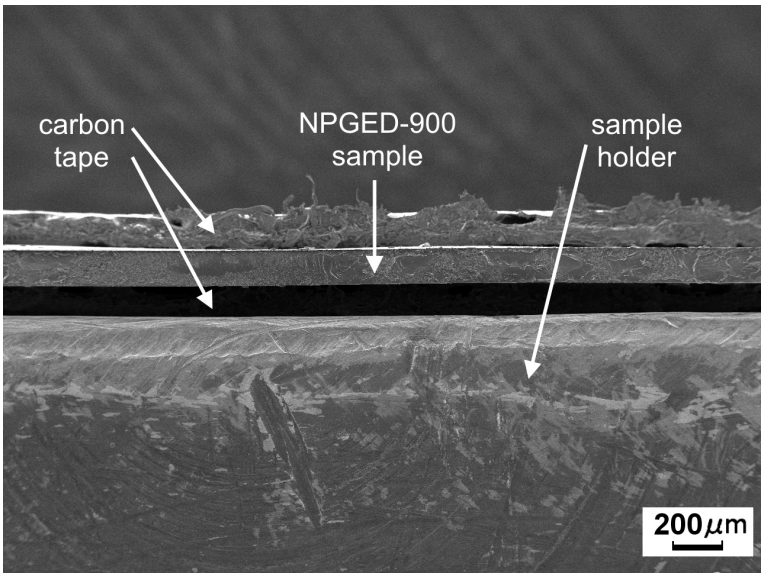

FIGURE 10. Cross section of a NPGED-900 membrane.

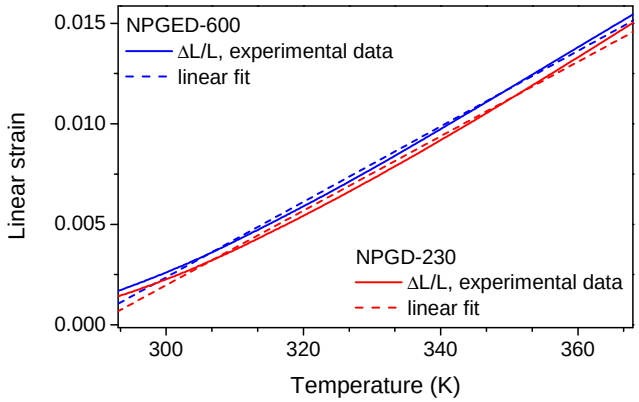

FIGURE 11. Linear strain ($\Delta L/L$) as a function of temperature for NPGED-600 (blue solid line) and NPGED-230 (red solid line). The dashed lines represent the linear fits of the experimental data.

From the data obtained from the structural characterization, some conclusions about the samples can be drawn:

(1) the preparation procedure gives rise to complete crosslinking between epoxide and crosslinker and permits the formation of defect-free samples;
(2) increasing the crosslinking density increases the glass transition temperature of the samples without affecting their morphology;
(3) the crosslink density does not influence the thermal expansion coefficient.

3.2. Epoxy-FLG nanocomposites

Graphene can be defined as a monolayer of graphite (Yoo et al., 2014), a perfect 2D material which has not only high transparency (Nair et al., 2008) and excellent mechanical properties (Lee et al., 2008) but is also gas-impermeable (Leenaerts et al., 2008). However, the production of high surface, non-defective graphene sheets is an expensive and complicated process (Cui et al., 2016).

Few Layer Graphene (FLG) nanoplatelets are graphene-derived materials consisting of stacks of graphene sheets which can be obtained via a top-down process as, for example, graphite exfoliation (Novoselov et al., 2012). These nanoparticles have thickness of few nm and a lateral size of the order of 1-10 µm. Thanks to their high aspect ratio and their impermeability, they are appropriate fillers for the production of PNC membranes with enhanced gas barrier properties (Yoo et al., 2014; Cui et al., 2016). Moreover, their high specific surface makes FLG nanoplatelets suited for a detailed study of the structural peculiarities appearing at the polymer-filler interface in nanocomposites and their influence on the gas barrier properties.

For the preparation of the epoxy-FLG nanocomposite samples, we decided to use the epoxy resin NPGED-900 (described in the above section) as a matrix. The low crosslink density of this polymer is accompanied by an open structure between the polymer chains, permitting high transport rates of penetrant gas molecules. This polymer is hence the best playground to study the possible effects of the FLG nanofillers on the penetrant transport process.

3.2.1. Epoxy-FLG nanocomposite preparation. Filaments of expanded graphite were obtained by submitting expandable graphite flakes provided by Faima srl (Italy) to thermal shock (750 °C, 3 mins). FLG nanoplatelets were fabricated by sonicating the filaments in acetone (C_3H_6O) for 30 mins at room temperature. Finally, FLG powders were obtained after drying in air the resulting suspension. Details on the preparation procedure can be found in Ref. (Carotenuto et al., 2014).

For the preparation of the nanocomposites, the FLG powders were firstly dispersed in acetone. The suspension was then stirred for 30 mins at 100 rpm using a mechanical stirrer, then it was sonicated for 20 mins using a horn sonicator. The epoxide was added in the desired amount and the obtained suspension was stirred for 3 more hours and left overnight. The hardener (Jeffamine ED-900, see section 3.1.1) was added in stoichiometric proportions to ensure complete crosslinking. The obtained solution was stirred for 30 mins and then cast on a glass support. Curing was carried out for 4 hours at 50 °C and for the following 12 hours at 80 °C.

Nanocomposite samples with different mass fractions of FLG were prepared, i.e. 5 wt. %, 7.5 wt. % and 10 wt. %. Given the mass density of $1.1\,\mathrm{g\,cm^{-3}}$ for the polymer matrix and $2.1\,\mathrm{g\,cm^{-3}}$ for the FLGs, these values correspond to volume fractions of 2.8 vol.%, 4.3 vol.% and 5.7 vol.%, respectively.

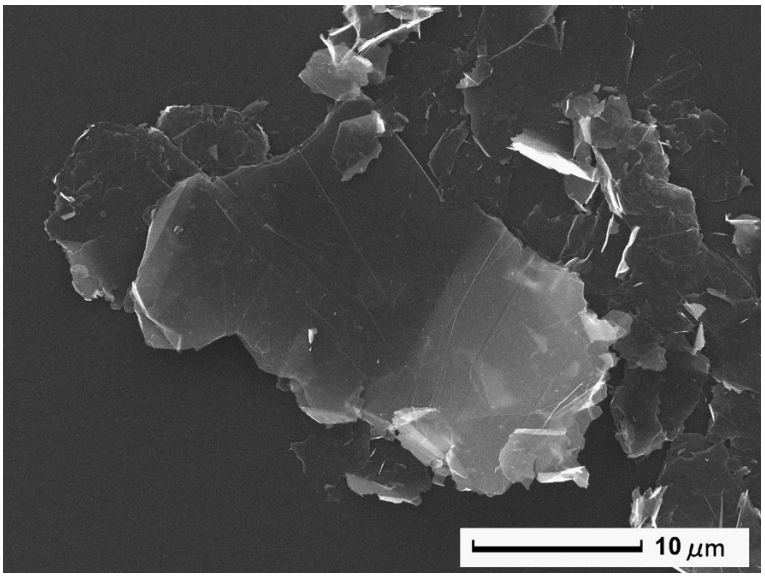

FIGURE 12. SEM micrograph of a FLG platelet

3.2.2. Epoxy-FLG nanocomposite characterization. The structural characterization of the epoxy-FLG nanocomposites was performed using SEM, X-ray diffraction (XRD) and DSC to study (i) the morphology of the samples; (ii) the degree of dispersion of the FLG nanoplatelets in the nanocomposites; (iii) their orientation and (iv) the influence of the fillers on the glass transition temperature of the polymer matrix.

3.2.2.1. *Scanning Electron Microscopy.* SEM images have been acquired using a JEOL JSM-7001F Field Emission Scanning Electron Microscope. To observe the cross section of the membranes, they were fractured in liquid nitrogen.

Figure 12 shows the morphology of a FLG nanoplatelet. It has irregular shape, lateral size of approx. 10 µm and a smooth surface. In Figure 13, we show micrographs of the surface of a pure NPGED-900 membrane (Figure 13(a)) and of three nanocomposite samples with 2.8, 4.3 and 5.7 vol.% filler loading (Figures 13(b), 13(c) and 13(d), respectively). The surface of the pure NPGED-900 membrane displays a uniform morphology, free from defects such as pinholes and cracks. In the nanocomposite samples, the presence of fillers below the first polymer layers can be observed. The FLG nanoplatelets appear uniformly dispersed and oriented with their surface parallel to the surface of the membrane.

The cross section of the samples is shown in Fig 14 for 2.8 vol.% filler loading. The filler particle can be distinguished from the surrounding polymer matrix, its shape and size are the same as the ones observed for isolated platelets (despite the sonication), and the particle has its surface parallel to the membrane surface. The inset of Figure 14 shows the cross section of a pure epoxy membrane: its morphology appears uniform and free from structures or pores.

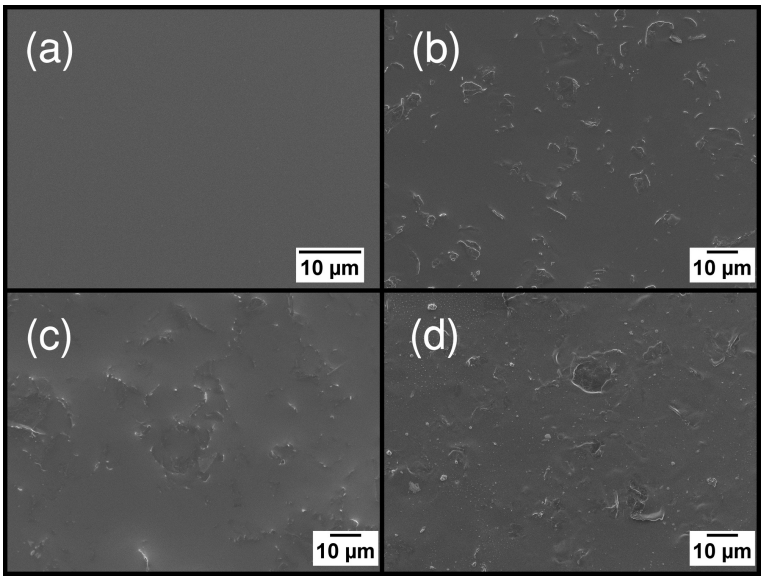

FIGURE 13. SEM micrograph of the surface of a pure epoxy membrane (a) and of nanocomposite samples with 2.8 (b), 4.3 (c) and 5.7 vol.% (d) filler loading.

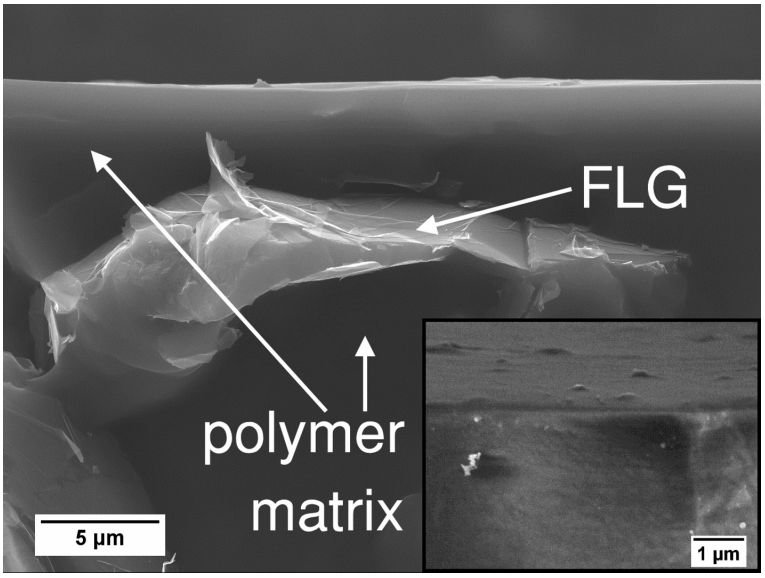

FIGURE 14. SEM micrograph of the cross section of a nanocomposite sample with 2.8 vol.% FLG concentration. In the inset, the cross section of a pure epoxy membrane.

3.2.2.2. *X-Ray Diffraction.* To study the size and orientation of the FLG particles in the nanocomposites, X-Ray Diffraction was used. Experiments were carried out in the Bragg-Brentano configuration using the Cu Kα radiation ($\lambda = 1.54\,\text{Å}$) using an XPert Pro Panalytical diffractometer. In Figure 15, we show the XRD

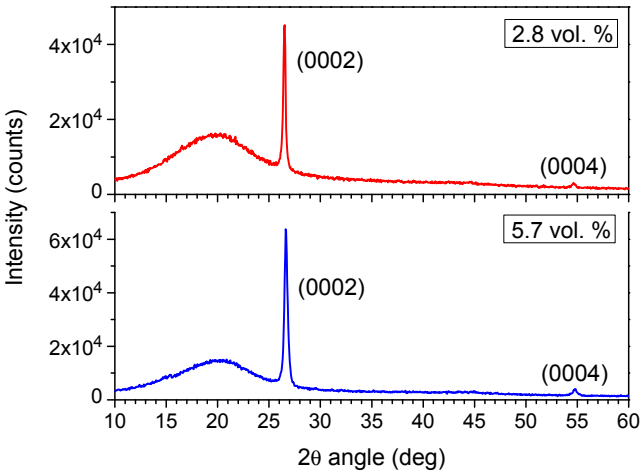

FIGURE 15. XRD spectra of the nanocomposite samples with 2.8 vol.% and 5.7 vol.% filler concentration.

spectra of the nanocomposite membranes with 2.8 vol. % and 5.7 vol. % filler loadings. The reflections of the g-C structure are evident in the (0002) and (0004) peaks at $2\theta \simeq 26.6°$ and $2\theta \simeq 57.8°$, respectively. The intensity of the peaks increases with the filler content. The broad reflection peak at angles between $2\theta \sim 10°$ and $2\theta \sim 30°$ is due to the amorphous polymer matrix.

From the XRD spectra, the following information can be obtained:

(1) Since only the (0002) and the (0004) are visible, the FLG platelets are oriented with their surface parallel to the surface of the membrane (Checchetto et al., 2014; Dimovski et al., 2004), as it was observed in the SEM micrographs;
(2) the average thickness of the nanoplatelets, as estimated by the analysis of the FWHM of the (0002) peak with the Debye-Scherrer equation, is $w = (10 \pm 1)\,\mathrm{nm}$;
(3) no ordered phase is induced in the polymer matrix by the addition of fillers.

3.2.2.3. *Differential Scanning Calorimetry.* DSC analysis was carried out on the pure and the nanocomposite samples to study the influence of the addition of FLG particles to the glass transition temperature. The analysis was performed using a DSC 8500 Hyper-enabled double-furnace Differential Scanning Calorimeter on samples weighting approx. 7 mg and with a heating rate or 5 K/min under nitrogen flow. Figure 16 shows the thermographs in the temperature range of 218-242 K. No significant variation in the glass transition temperature of the nanocomposite samples was observed, with respect to the pure polymer.

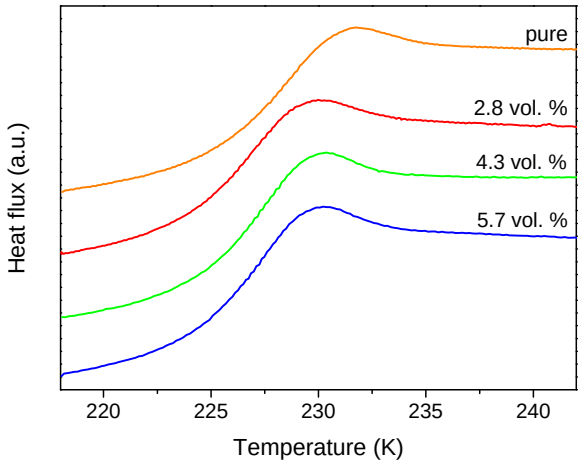

FIGURE 16. DSC thermographs of the pure NPGED-900 and the FLG nanocomposite samples with 2.8 vol. %, 4.3 vol. % and 5.7 vol. % filler loading.

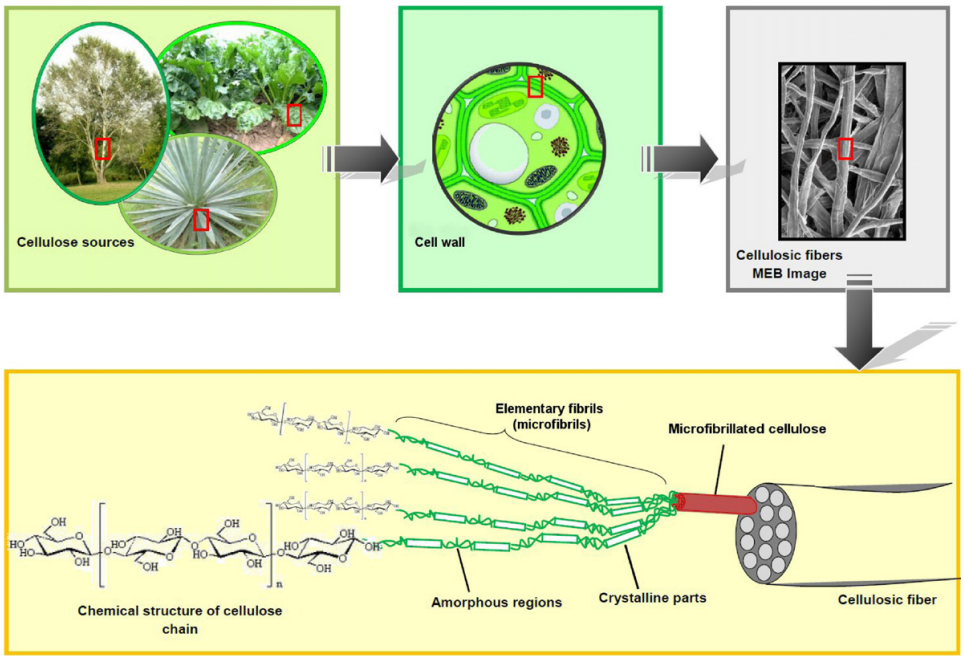

FIGURE 17. A graphical description of the structure of cellulosic fibers, from plants down to the chemical structure of the cellulose crystals. Reproduced from (Lavoine et al., 2012) with permission from Elsevier.

3.3. Cellulose nanofibers

Cellulose is considered the most abundant polymer on Earth (Dufresne, 2010; Siqueira et al., 2010). It is a structural polymer conferring its mechanical strength to higher plant cells and making up for approximately half the weight of wood Dufresne (2013). Its basic structural components are Cellulose Nanofibers (CN): rod-like crystalline cellulose domains with the structure shown in Figure 17, and having a dimer called cellobiose as a repeating unit (Lavoine et al., 2012). These crystalline domains, in plants, are linked to one another by amorphous regions forming longer microfibrils, which are packed in larger fibers called microfibrillated cellulose (MFC). These are immersed in an amorphous phase consisting mainly in lignin and hemicellulose, forming the cellulosic fibers which, on turn, make up for the plant cell walls (Dufresne, 2013; Lavoine et al., 2012).

Cellulose nanofibers can be obtained from wood pulp in several ways. A mechanical treatment can be used to isolate cellulose fibers from the lignocellulosic fibers. This procedure provides microfibrillated cellulose, having an amorphous fraction and actually consisting of aggregates of individual, crystalline nanofibers. MFC fibers have widths in the range of 20 to 60 nm and length of more than 1 µm (Lavoine et al., 2012; Chirayil et al., 2014).

As an alternative route, acid hydrolysis can be used to attack the amorphous parts of the cellulose fibers and break them in highly crystalline nanofibers with cross sectional diameter of approx. 5 nm and length of the order of 100 nm (Dufresne, 2013). This is however a hydrolytic procedure, thus it has low yield and it strongly decreases the fiber length to 100 -150 nm (Saito et al., 2007).

For this work, another method has been used to separate the individual cellulose nanofibers by preventing the formation of hydrogen bonds between them. 2,2,6,6-Tetramethylpiperidine-1-oxyl radical (TEMPO) -mediated oxidation was first reported by Saito et al. (2007) and it allows to convert the primary hydroxyls on the nanofibers' surface to carboxylate groups. A subsequent mechanical treatment allows to obtain individual TEMPO-Oxidized Cellulose Nanofibers (TOCNs) with widths of 3 - 4 nm and high aspect ratios (Fukuzumi et al., 2013b).

In the following, we will present in detail the preparation of the TOCN films and their structural, morphological and optical characterization. The gas transport properties of TOCN were studied using bilayer membranes consisting of few µm thick TOCN coatings on polylactic acid (PLA) foils which acted as a mechanical support. For the purposes of this study, PLA proved to be a well suited substrate for the cellulose nanofiber coatings because its hydrophilic character allowed to deposit uniform CN films by the casting technique described in the following (in fact, before the deposition, the cellulose nanofibers are in aqueous solution).

Nanocomposite TOCN films with dispersed TiO_2 nanoparticles were also prepared and studied, to investigate the influence of the fillers on the optical and gas transport properties of the films. TiO_2 nanoparticles were chosen as a filler, given their well known antimicrobial properties, which make them interesting for applications in food packaging technology (De Azeredo, 2009).

3.3.1. Cellulose fibers oxidation. To prepare the cellulose nanofibers (CN) films, a method described by Saito et al. (2007) was used. TEMPO -mediated oxidation of cellulose fibers at alkaline conditions and room temperature was performed to convert primary hydroxyls into carboxylate groups and obtain carboxylated cellulose nanofibers. 1 g of cellulose pulp, provided by SCA-Ostrand (Sweden) was suspended in 100 ml of water and kept under constant stirring for 1 h. Catalytic amounts of TEMPO (0.16 mg) and NaBr (0.1 g) were added to the slurry. 3.1 g of NaClO were then added to the mixture, which was stirred at a pH between 10.5 and 11.0 by adding NaOH (1 M) until no further decrease was observed in the pH. Then, the pH was lowered to 7.0 by washing the obtained slurry at least 10 times with high-purity water (400 ml). An ultrasonic tip with diameter of 13 mm (Bandelin Sonopuls HD2200) was used to sonicate 45 ml of the slurry for 4 mins at 20 kHz and an output power of 100 W_{eff} delivered in the sample's volume, to finally obtain a transparent suspension of TEMPO-Oxidized Cellulose Nanofibers (TOCN) having a density of 2.7 $mg\,ml^{-1}$ (Bettotti et al., 2016).

3.3.2. Film preparation. To obtain few micron thick coatings, the TOCN suspension was casted by directly pouring it on PLA disks having thickness of (23 ± 1) µm and diameter of 3 cm. These PLA foils, on turn, were laid on a polydimethylsiloxane (PDMS) substrate providing a hydrophobic surface able to confine the aqueous CN suspension. Drying was performed in an oven at 60 °C for 24 h. No surface treatment was performed on the PLA substrates thanks to the hydrophilic nature of this polymer which favored the formation of uniform coatings. In the following, we will call TOCN/PLA bilayer membranes the samples obtained as just described. Self-supporting TOCN films were prepared as well by casting the TOCN suspension on Petri dishes. The films were peeled off the dishes after annealing.

The thickness ℓ_{TOCN} of the TOCN films was evaluated starting from the analysis of their UV-Vis transmission spectra as described in detail in the following. In this way, a calibration was obtained, which allowed to predict the film thickness knowing the amount of the poured TOCN solution. TOCN films with thicknesses ranging from $\sim 2\,\mu\mathrm{m}$ to $\sim 12\,\mu\mathrm{m}$ were obtained by casting amounts of TOCN suspension per unit substrate surface in the range 0.4-2.4 $\mathrm{mg\,cm^{-2}}$.

The density ϱ_{TOCN} of the films was measured by preparing 7 films having a surface of $(4.0 \pm 0.2)\,\mathrm{cm^2}$ and measuring the thickness of each film as an average over three measurements performed on different regions. This allowed to evaluate the volume and hence the mass density of each film. The density $\varrho_{\mathrm{TOCN}} = (1.57 \pm 0.06)\,\mathrm{g\,cm^{-3}}$ was obtained as the average density of the 7 films.

3.3.3. Nanocellulose-TiO_2 nanocomposite preparation. Nanocomposite TOCN:TiO_2 films were prepared by adding TiO_2 nanoparticles to the CN dispersion. Degussa Aeroxide TiO_2 p25 nanoparticles having diameter of approx. 21 nm (EVONIK Industries, 2015) and a combination of rutile and anatase crystal structure were purchased from Evonik (Essen, Germany) and dispersed in the TOCN solution to obtain a weight fraction of 5 % of TiO_2 nanoparticles in the cellulose nanofibers films. TOCN:TiO_2/PLA bilayer membranes were prepared by casting the obtained solution on PLA foil with thickness (23 ± 1) µm as described in the case of pure TOCN. Given the TiO_2/TOCN weight ratio, the mass density ϱ_{TOCN} of the cellulose nanofibers and that of the TiO_2 nanoparticles $\varrho_{\mathrm{TiO_2}} = 3.9\,\mathrm{g\,cm^{-3}}$ (EVONIK Industries, 2015), the volume fraction of TiO_2 nanoparticles in the TOCN:TiO_2 layers is $\varphi_{\mathrm{TiO_2}} = 2\%$. The thickness $\ell_{\mathrm{TOCN:TiO_2}}$ of the coatings was calculated knowing the amount of solution casted and $\varphi_{\mathrm{TiO_2}}$, based on the calibration made for pure TOCNs.

3.3.4. Nanocellulose film characterization.

3.3.4.1. *Atomic Force Microscopy.* The morphology and the dimensions of isolated TOCNs and of the TOCN films were observed by a digital AFM microscope (Solver NT-MDT) operating in semi contact mode. Isolated TOCNs were obtained by depositing a drop of TOCN solution, suitably diluted with water, on a silicon

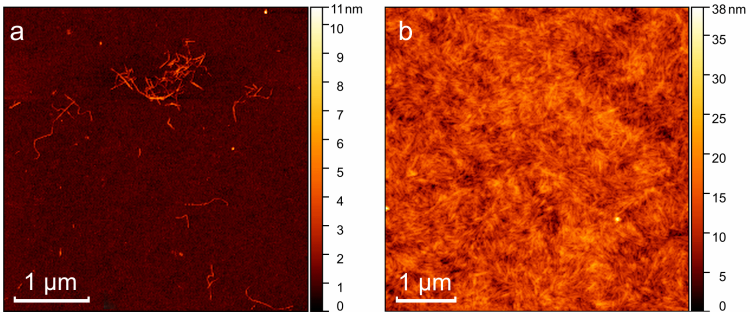

FIGURE 18. AFM images of (a) isolated cellulose nanofibers deposited on a silicon substrate; (b) surface of a TOCN coating deposited on a PLA substrate.

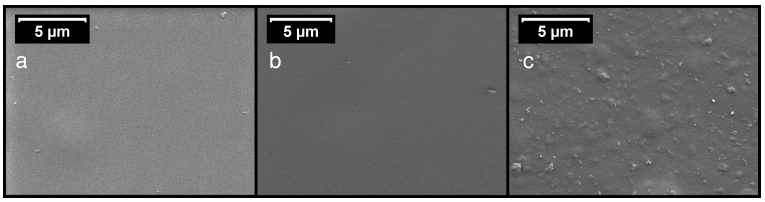

FIGURE 19. SEM micrographs of: (a) the surface of an uncoated PLA substrate; (b) the surface of a TOCN coating and (c) the surface of a TOCN:TiO_2 coating

substrate and drying it at 60 °C in an oven (Bettotti et al., 2016). To visualize and analyze the obtained data, the Gwyddion package was used (Neas and Klapetek, 2012). An AFM micrograph for isolated cellulose nanofibers deposited on a silicon support is reported in Figure 18 (a). A statistical study carried out on similarly prepared samples (Bettotti et al., 2016) revealed that the TOCN under study have an average diameter of 4 nm and lengths in the range of 50 - 300 nm. Figure 18 (b) shows the AFM image of the surface of a TOCN coating. The fibers appear oriented with their main axis parallel to the coating's surface and they form a densely packed network.

3.3.4.2. *Scanning Electron Microscopy.* The morphology of the membranes' surfaces and cross sections was studied by field emission scanning electron microscopy using a JEOL JSM-7001F microscope operating at 2 kV. The samples were metalized and, to observe their cross section, freeze-cut in liquid nitrogen.

Figure 19 shows SEM micrographs of the surface of an uncoated PLA foil (a), of a TOCN coating (b) and of a TOCN:TiO_2 coating (c). All membranes show a uniform morphology, free from imperfections such as pinholes and cracks. TiO_2 nanoparticle aggregates can be seen in Figure 19 (c). Figure 20 shows the cross section of a TOCN/PLA bilayer membrane (a) and of a TOCN:TiO_2/PLA bilayer membrane (b) fractured in liquid nitrogen. The coatings can be distinguished by the substrates, the micrographs reveal the uniformity of their thickness. A SEM

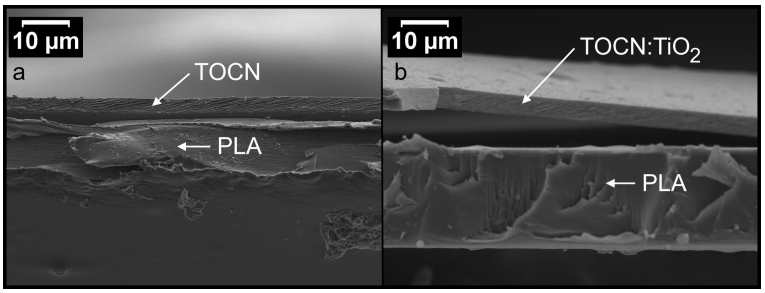

FIGURE 20. Cross sections of a TOCN/PLA bilayer membrane (a) and a TOCN:TiO_2/PLA bilayer membrane (b)

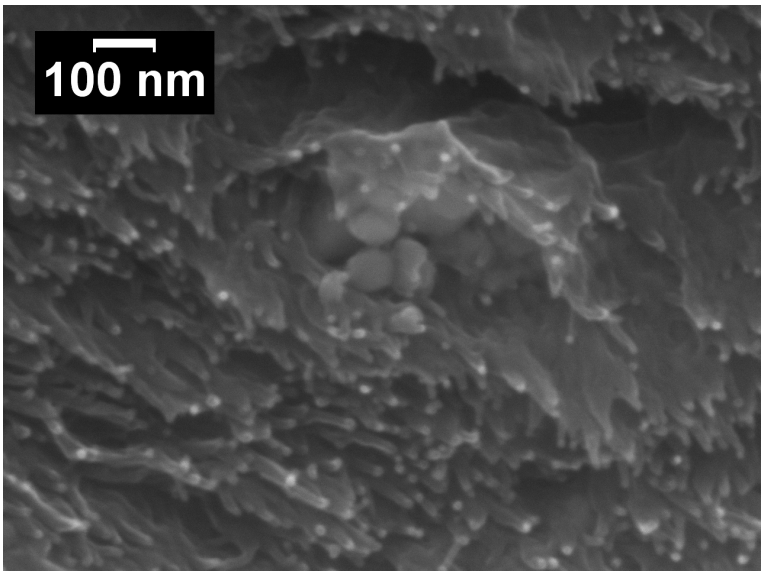

FIGURE 21. SEM micrograph of the cross section of a TOCN:TiO_2 coating.

micrograph of the cross section of a TOCN:TiO_2 layer at higher magnification is shown in Figure 21. This image allows to distinguish individual TOCNs and clearly evidences that they are aligned parallel to one another and their main axis is parallel to the surface of the coating. The image also shows an agglomerate of TiO_2 nanoparticles, with size of the order of 100 nm. Larger agglomerates are also found, mostly located at the interface between PLA and the coating.

3.3.4.3. *Optical characterization.* The absorption spectra of bilayer membranes and self-supporting TOCN films were acquired using a Varian Cary 5000 UV-Vis-NIR spectrophotometer operating in transmittance mode at wavelengths between 190 and 900 nm, with a resolution of 1 nm. From the spectra, the thickness ℓ_{TOCN} of the self-supporting TOCN films was obtained using the following equation (Poelman and Smet, 2003):

$$\ell_{\mathrm{TOCN}} = \frac{N}{4(k_2 - k_1)} \frac{1}{\sqrt{n^2 - \sin^2\theta}} \tag{3.3.1}$$

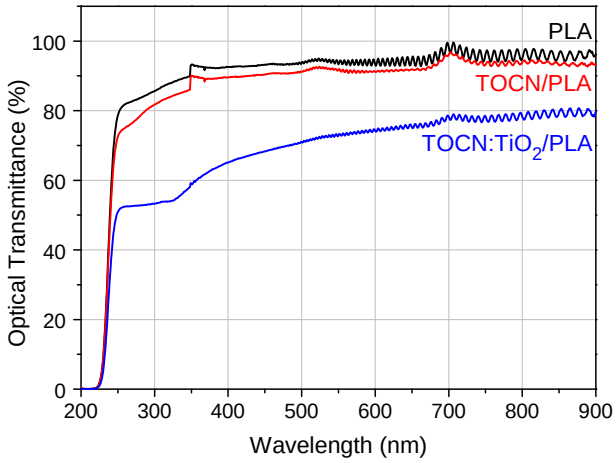

FIGURE 22. Optical transmittance spectra of a (23 ± 1) µm thick PLA foil (black line), a TOCN/PLA bilayer membrane with coating thickness of (2.5 ± 0.1) µm (red line) and a TOCN:TiO_2/PLA bilayer membrane with coating thickness of (2.5 ± 0.1) µm (blue line).

where k_1 and k_2 are the maximum and minimum wavenumbers of the interval taken into consideration, N is the number of fringes in this interval, θ is the angle of incidence and in our case it holds $\theta = 0$ and n is the refraction index of the film material, it is $n = 1.58$ in our case and we considered it constant in the examined wavelength range (Nogi et al., 2005).

In Figure 22, we report the optical transmittance (OT) spectra of a (23 ± 1) µm thick PLA foil, of a TOCN/PLA bilayer membrane with TOCN coating thickness of (2.5 ± 0.1) µm and a TOCN:TiO_2/PLA bilayer membrane with coating thickness of (2.5 ± 0.1) µm. The OT of PLA is almost zero in the low UV range and increases gradually at wavelengths λ around 225 nm. At $\lambda = 300$ nm, the OT is 86%, and it increases in the visible range, reaching values of $\sim 95\%$ at $\lambda = 600$ nm. The TOCN coating only slightly reduces the transparency of the membrane, which remains highly transparent to visible light: the OT is $\simeq 90\%$ at 600 nm. These data confirm the uniformity of the TOCN films and the lack of pores or structures which could reduce their OT by scattering light. Light transmission is more markedly reduced by the dispersion of TiO_2 nanoparticles both in the UV and in the visible range. TiO_2 absorbs indeed UV light due to its bandgap at 3.0 - 3.2 eV (Chen and Mao, 2007), whereas the reduction in the OT in the visible range can be attributed to light scattering from the TiO_2 nanoparticle aggregates detected by SEM (see Figure 21) (Caseri, 2000).

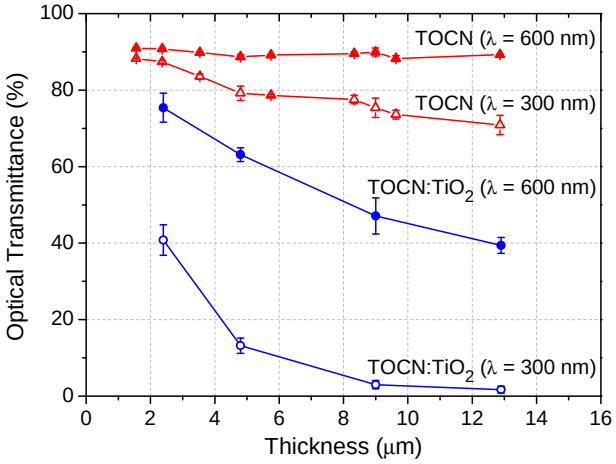

FIGURE 23. Optical transmittance of self-supporting TOCN (red symbols) and TOCN:TiO_2 layers (blue symbols) as a function of the thickness ℓ of the films. Open symbols refer to the OT values at $\lambda = 300\,\text{nm}$ and solids symbols represent values measured at $\lambda = 600\,\text{nm}$. The experimental points and the error bars represent the average values and standard deviations of at least 4 measurements.

Figure 23 shows the OTs of self-supporting TOCN and TOCN:TiO_2 films as a function of their thickness and at two different wavelengths, 300 nm (UV) and 600 nm (Vis). At 600 nm, the pure TOCN films maintain OT values of almost 90 % even for thickness $\ell_{\text{TOCN}} > 10\,\mu\text{m}$. In the UV, at 300 nm, the OT of TOCN films is $(72 \pm 2)\,\%$ with a $12\,\mu\text{m}$ thick coating. The presence of TiO_2 nanoparticles, instead, reduces light transmission, especially in the UV, where it drops to less than 10 % for film thicknesses of $\sim 10\,\mu\text{m}$.

If the light scattering due to the interface between the TOCN films and the air can be neglected, the OT spectra obtained with self-supporting TOCN films with different thicknesses ℓ_{TOCN} allow us to evaluate the optical absorption coefficient α_λ by Lambert's law (Young, 2000):

$$I \simeq I_0(1-\mathcal{R})^2 \exp(\alpha_\lambda \ell_{\text{TOCN}}) \tag{3.3.2}$$

$$OT(\%) = 100\frac{I}{I_0} \tag{3.3.3}$$

where I is the intensity of the light beam transmitted through a film of thickness ℓ_{TOCN}, I_0 the intensity of the incident beam and $\mathcal{R}$ is the reflectivity of the films, for normal incidence of the light beam. α_λ and $\mathcal{R}$ can be obtained, respectively, from the slope and from the intercept of the straight line which best fits values

	TOCN	TOCN:TiO_2
$\alpha_{300\,\mathrm{nm}}$ (μm^{-1})	$(25 \pm 1) \times 10^{-3}$	$(61 \pm 3) \times 10^{-3}$
$\alpha_{600\,\mathrm{nm}}$ (μm^{-1})	$(1.0 \pm 0.4) \times 10^{-3}$	$(36 \pm 5) \times 10^{-3}$
$\mathcal{R}_{300\,\mathrm{nm}}$	$(4.2 \pm 0.2) \times 10^{-2}$	0.0 ± 0.1
$\mathcal{R}_{600\,\mathrm{nm}}$	$(5.0 \pm 0.2) \times 10^{-2}$	$(7.7 \pm 0.9) \times 10^{-2}$

TABLE 1. Measured optical absorption coefficients α_λ and reflectivity $\mathcal{R}$ (see equation (3.3.2)) of the TOCN and TOCN:TiO_2 films.

of $\ln(I_{00}/I_{OT})$ plotted as a function of ℓ_{TOCN}. The obtained values are reported in Table 1.

CHAPTER 4

Methods

In this chapter, we will describe the techniques used for the determination of the gas transport properties of the studied membranes and their free volume structure. For the gas transport measurements, two different techniques were used. In the following, we will describe them in detail to make clear their advantages and drawbacks and to clarify why each technique was chosen for the specific membrane samples under study.

Subsequently, we will describe the PALS technique and the coincidence setup used for the free volume studies in the epoxy-based membranes, as that is the most common setup for Ps lifetime experiments in polymers. A different experimental technique has been used for the free volume study of nanocellulose films: details on it are given in the relative publication by Roilo et al. (2017) and references therein. Nevertheless, the physics underlying the experimental technique is the same and it is described in this chapter.

4.1. Gas transport experiments

In this section, we will describe how the quantities $J(t)$ and $Q(t)$ given by equations (2.1.13) and (2.1.17), respectively, can be measured and how the gas transport parameters P, D and S can be obtained from the experiments.

In this thesis work, two home-built apparatuses were used for the gas transport measurements, based on the same working principle. In these setups, the studied membrane separates two vacuum chambers, which are evacuated to their background vacuum before each experimental run. At time $t = 0$ (trigger time of the experiment), the High Pressure Side (HPS) of the membrane is exposed to the permeant gas at a fixed pressure p_{HPS}. Gas molecules permeate through the membrane and reach the analysis chamber facing the Low Pressure Side (LPS) of the membrane, where the pressure p_{LPS} increases in time as described by (Redhead et al., 1993):

$$I(t) = V \frac{\mathrm{d}p_{\mathrm{LPS}}(t)}{\mathrm{d}t} + S_{\mathrm{P}}\, p_{\mathrm{LPS}}(t). \tag{4.1.1}$$

where $I(t)$ is the gas stream (expressed as [volume]×[pressure]/[time]) entering the analysis chamber, V the volume of the analysis chamber and S_{P} the pumping speed of the pump evacuating it. The gas flux expressed as a quantity of matter per unit

	He	H_2	D_2	H_2O	N_2	O_2	CO_2
T_c (K)	5.19	33.2	38.2	647	126.2	154.6	304.2
σ_k (Å)	2.60	2.89	2.89	2.65	3.64	3.46	3.3

TABLE 1. Critical temperature T_c and kinetic diameter σ_k of the gases used in the studies presented in this work (Redhead et al., 1993; Breck, 1974; NIST, 2017; Hoge and Lassiter, 1951).

time and unit area is given by

$$J(t) = \frac{I(t)}{ART_a} \tag{4.1.2}$$

where R is the ideal gas constant, A is the membrane surface exposed to the gas and T_a is the temperature of the gas in the analysis chamber.

One of the two apparatuses used for the experiments works at constant volume (CV), meaning that the analysis chamber is isolated from the pumping system just before each experimental run, making $S_P = 0$ in equation (4.1.1). As a result, during the tests the permeation flux $J(t)$ is proportional to the time derivative of p_{LPS}. In the second apparatus, working under constant pumping (CP), the analysis chamber is constantly evacuated and the term $V\frac{dp_{LPS}(t)}{dt}$ in equation (4.1.1) can be neglected. In this case $J(t)$ is proportional to p_{LPS}.

Test gases having different kinetic diameters and condensability properties have been used to study the gas transport properties of the membrane samples. The kinetic diameters σ_k and the critical temperatures T_c of all gases used in this work are reported in Table 1.

In the following sections, we will give all details on the apparatuses and how the recorded signals are analyzed to obtain the gas transport parameters.

4.1.1. Permeation experiments at constant volume.

4.1.1.1. *Experimental apparatus.* The experimental apparatus used for the gas phase permeation measurements in constant volume is schematically represented in Figure 1. A photograph is shown in Figure 2. The apparatus was built using standard ultra high vacuum stainless steel components. It consists of three main parts: a gas feed line, which also acts as a high pressure side chamber, a sample holder, and an analysis chamber where the permeated gas is detected.

The gas feed line is made of standard copper pipes (6 mm external diameter) and is evacuated by a molecular drag pump (TP2) backed by a rotary vane vacuum pump (RP2) to a vacuum in the 10^{-1} Pa range. During the experimental run, the pressure in the gas feed line (i.e. the pressure of the gas in contact with the HPS of the membrane) is measured by a Baratron Gauge (BG2, MKS 626) with full-scale reading of 10^5 Pa. A variable leak valve (VL) allows to fill the pipes between valves

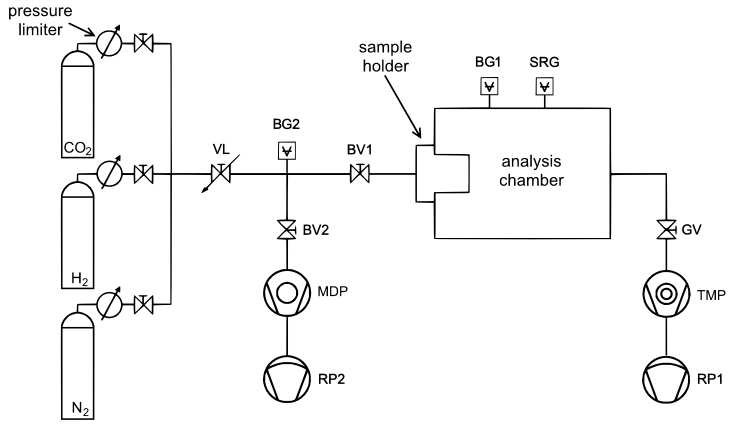

FIGURE 1. A schematic of the apparatus used for the permeation measurements at constant volume.

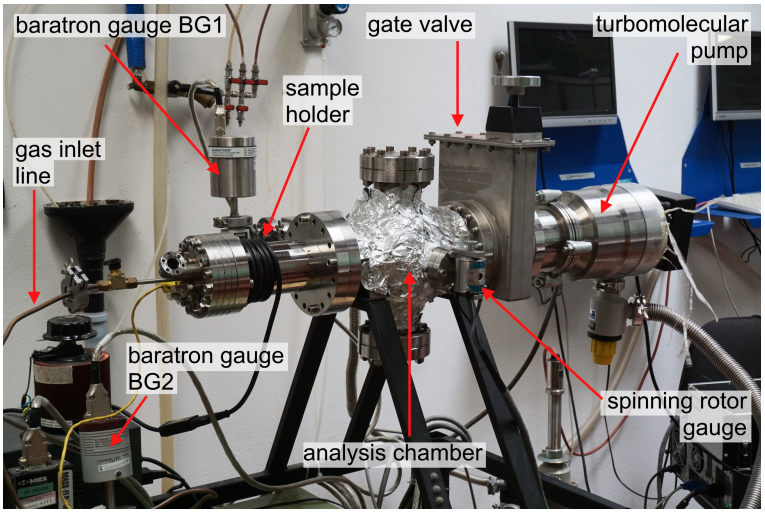

FIGURE 2. A photograph of the CV apparatus.

VL, BV1 and BV2 with pure gases from high pressure cylinders at the desired pressure.

The sample holder is schematically represented in Figure 3. It consists of a standard CF70 flange, on which a cylindrical tube with wall thickness of 3 mm has been welded. The tube contains two heating cartridges, a stainless steel pipe which is connected to the gas inlet line and feeds the gas to the membrane and a thermocouple to measure the sample's temperature. A properly designed flange in AISI 316 L stainless steel is welded to the opposite side of the tube, see Figures 3 and 4. Samples are placed between this flange and a cap. A Viton O-ring ensures high vacuum sealing between the sample and the sample holder. To avoid mechanical failures of the membrane samples due to the different pressures between HPS and LPS, a disc of porous steel was placed between the sample and the cap. The gas

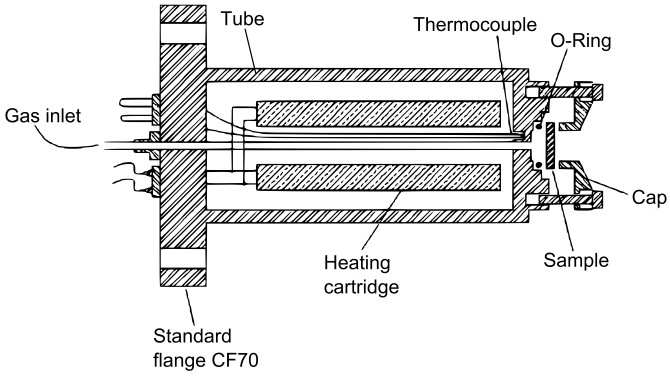

FIGURE 3. A schematic diagram of the sample holder.

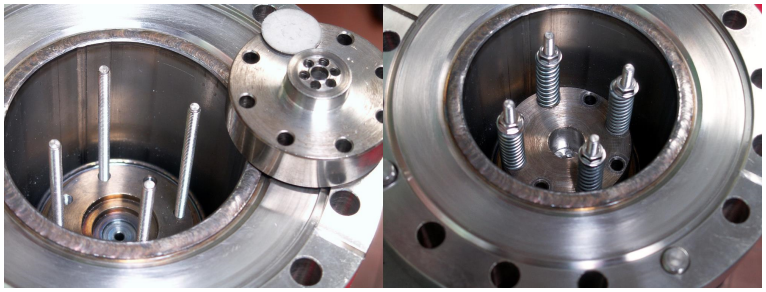

FIGURE 4. Photographs of the sample holder, with removed cap and porous steel disc (left) and with assembled cap (right)

permeability of this highly porous steel (0.5 µm rejection grade) is much larger than that of the examined membranes and does not affect the measured permeability value of the examined polymeric membrane.

The analysis chamber has a volume V of $3.0 \times 10^{-3}\,\mathrm{m}^3$ and is evacuated by a turbomolecular pump (TP1, Leybold Turbovac 360), which is backed by a rotary vane vacuum pump (RP). The background vacuum in the analysis chamber is in the 10^{-5} Pa range. The analysis chamber can be separated from the turbomolecular pump using a gate valve (GV). The pressure increase in the analysis chamber due to the permeating gas can be measured by a Baratron pressure gauge (BG1, MKS 627B) and a spinning rotor pressure gauge (SRG, MGS SRG-2) with a full-scale reading of 10^2 Pa and 1 Pa respectively.

4.1.1.2. *Procedure.* The experimental procedure for permeation measurements consists of the following steps:

(1) first of all, both the gas inlet line and the analysis chamber are evacuated to their background vacuum;
(2) using the variable leak valve VL, the volume between valves VL, BV1 and BV2 is filled with test gas from the cylinders;
(3) the gate valve GV of the LPS is closed;

(4) the experiment is triggered at $t = 0$ by opening the BV1 valve, to feed the gas to the membrane.

The pressure p'_{LPS} in the analysis chamber is recorded as a function of time at fixed time intervals. As will be discussed in detail later, the total pressure p'_{LPS} of the gas in the analysis chamber is in general slightly larger than the partial pressure p_{LPS} of the permeated gas.

The experiments end when p'_{LPS} reaches the full-scale value of the measuring instruments: the duration of the experiments thus depends both on experimental parameters such as sample temperature and p_{HPS} value as well as the permeation properties of the membrane material. In our experimental runs, the pressure p_{HPS} in the gas feed line (i.e. in the high pressure side chamber) was always constant within less than 1% during the whole experiment. Furthermore, since pressure p'_{LPS} in the low pressure side was always negligible with respect to p_{HPS} (at least 10^4 times smaller), the trans-membrane pressure $\Delta p = p_{\mathrm{HPS}} - p_{\mathrm{LPS}}$ was effectively coincident with p_{HPS}.

4.1.1.3. *Detected signal and gas transport parameters.* For the tests performed at CV, the pressure signal $p_{\mathrm{LPS}}(t)$ is directly proportional to the quantity $Q(t)$ of gas permeated through a membrane of unit area at time t. Indeed, since the valve (GV) is closed during the experimental runs, the term proportional to S_{P} in equation (4.1.1) vanishes. In this case, remembering also equation (4.1.2) and integrating it in time from 0 to t, we see that

$$Q(t) = \int_0^t J(\tau) d\tau = p_{\mathrm{LPS}}(t) \frac{V}{A\,R\,T_{\mathrm{a}}}, \tag{4.1.3}$$

where A is the membrane surface, R is the perfect gas constant and T_{a} is gas temperature in the analysis chamber (thermal equilibrium conditions between permeated molecules and analysis chamber are immediately set by collision processes with the chamber walls). The comparison of the experimentally obtained $Q(t)$ curve with equations (2.1.17) and (2.1.18) allows to calculate permeability and diffusivity as described in section 2.1.3.

It is worthy to note that the pressure increase in the analysis chamber during the measurements presents a background signal due to outgassing processes (mostly gas release from the internal walls of the chamber). Consequently, the measured total pressure p'_{LPS} is actually the sum of two contributions:

$$p'_{\mathrm{LPS}}(t) = p_{\mathrm{LPS}}(t) + p_{\mathrm{bck}}(t) \tag{4.1.4}$$

where $p_{\mathrm{bck}}(t)$ is the partial pressure of outgassed gas, called background pressure. In order to subtract $p_{\mathrm{bck}}(t)$ from $p'_{\mathrm{LPS}}(t)$, the background signal needs to be measured. The following procedure is used:

(1) with the HPS chamber evacuated to its background vacuum, the analysis chamber is evacuated to the final background pressure;

(2) the gate valve GV is closed and the pressure increase in the analysis chamber is monitored as a function of time to evaluate the $\frac{dp_{\mathrm{bck}}}{dt}$ background signal.

In the present experimental apparatus, the outgassing process gives rise to a linear increase of the pressure in the analysis chamber: by fitting $p_{\mathrm{bck}}(t)$ to a straight line, for the experiments presented here, it was found that the outgassing rate is always lower than $\frac{\mathrm{d}p_{\mathrm{bck}}}{\mathrm{d}t} \simeq 10^{-8}\,\mathrm{kPa/s}$ as measured by both pressure gauges.

The background signal $\frac{dp_{\mathrm{bck}}}{dt}$ is measured before each experimental test. The signal to noise ratio SNR of the permeation measurement, defined as

$$\mathrm{SNR} = \left(\frac{dp_{\mathrm{LPS}}}{dt}\right)\left(\frac{dp_{\mathrm{bck}}}{dt}\right)^{-1} \tag{4.1.5}$$

was always larger than five for the experiments discussed in this work.
Due to the use of a total pressure gauge as a detector, a high permeation signal to noise ratio is needed to obtain accurate measurements with this technique. The CV technique is therefore used mostly for membranes having relatively high permeability. In this thesis work, it was used to analyze the gas transport properties of epoxy-based membranes and polypropylene-based membranes.

4.1.2. Permeation experiments under constant pumping.

4.1.2.1. *Experimental apparatus.* The apparatus schematically represented in Figure 5 was used to carry out the permeation measurements with constantly pumped analysis chamber (CP conditions). A photograph is shows in Figure 6. This setup is home-built and was described in detail by Checchetto et al. (1995). For the present work, it was slightly modified to accommodate polymer membranes.

The analysis chamber is an electropolished AISI 304 L stainless steel vessel with $2 \times 10^{-2}\,\mathrm{m}^3$ volume. It is evacuated by a turbomolecular pump (TMP, Adixen model ATP 150), backed by a molecular drag pump (MDP) and a diaphragm pump to a background vacuum in the $10^{-7}\,\mathrm{Pa}$ range. The system does not contain elastomers, apart from the Viton O-rings providing gas-tight support to the membrane inside the sample holder. A Bourdon pressure gauge (BG Wika, full scale reading $5 \times 10^{2}\,\mathrm{kPa}$, resolution $5\,\mathrm{kPa}$) and a thermocouple pressure gauge (TG, Varian model 0531, full scale reading $10^{-2}\,\mathrm{kPa}$) allow to measure the pressure p_{HPS} of the gas in contact with the HPS of the membrane. The gas in the analysis chamber can be detected by an ionization gauge (IG, Varian model 850), a spinning rotor gauge (SRG, MKS model SRG-2) and a quadrupole mass spectrometer (QMS, Balzers model QMG 420) with an electron impact source and a secondary electron multiplier detector.

The sample holder is schematically represented in Figure 7, photographs are shown in Figure 8. The membrane is clamped between two O-rings; two plates of porous steel are placed inside the O-rings and provide mechanical support to the membranes. The membrane samples are disks with an effective diameter (defined

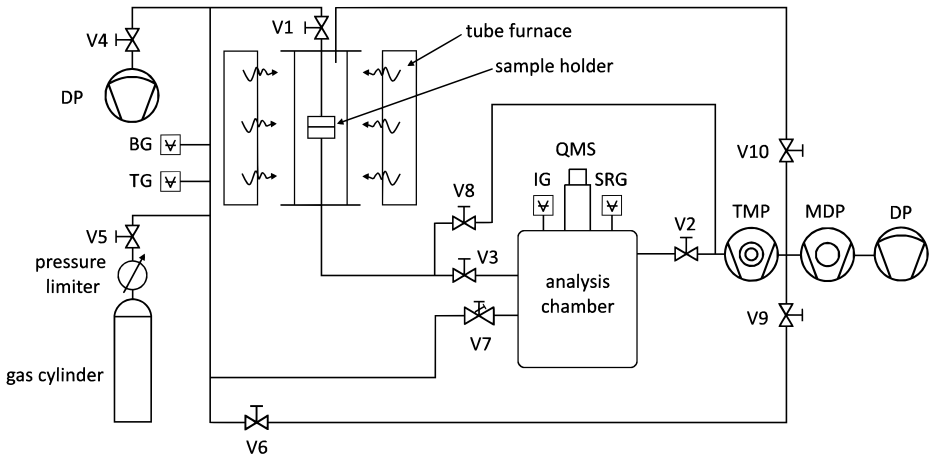

FIGURE 5. Schematic diagram of the apparatus used for gas transport experiments at constant pumping. TMP: turbomolecular pump, MDP: molecular drag pump, DP: diaphragm pump, IG: ionization pressure gauge, TG: thermocouple pressure gauge, BG: bourdon pressure gauge, SRG: spinning rotor pressure gauge, QMS: quadrupole mass spectrometer

by the O-rings) of 13 mm. The sample holder is placed inside a tube oven and is kept under vacuum to prevent the detection of any gas permeation signal other than that relative to the gas permeating from the HPS to the LPS of the membrane.

4.1.2.2. *Procedure.* The procedure for a gas transport experiment includes the following steps:

(1) the whole apparatus is first evacuated to the background vacuum;
(2) the tubes between valves V1 and V4-V7 (see Figure 5) are filled with the chosen test gas at the desired pressure;
(3) at $t = 0$, the measurement is started by opening the valve V1 and letting the gas get in contact with the high pressure side of the membrane.

During the measurement, the valve V8 is closed and the valves V2 and V3 are open, so the permeated gas flows through the analysis chamber, which is constantly pumped by the turbomolecular pump. The permeated gas is detected by the QMS. The use of a mass spectrometer instead of a pressure gauge allows accurate measurements by detecting only the chosen molecules (i.e. the ones permeating through the membrane) and avoiding therefore the contributions given from the flux of gases desorbing from the analysis chamber's walls. Thus, the mass spectrometer allows to detect slight variations in the partial pressure of one specific gas, which could not be detected by total pressure measurements. The partial pressure of a gas in the analysis chamber is directly proportional to the QMS signal relative to that gas. The sensitivity of the QMS, defined as the ratio of the QMS signal (ion current) to

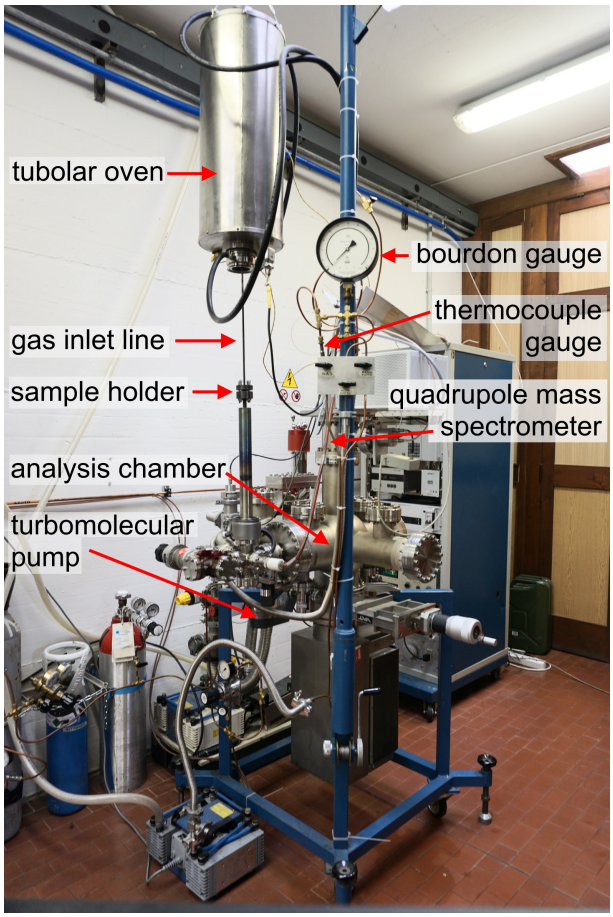

FIGURE 6. Photograph of the apparatus for the permeation experiments in CP conditions. In this photograph, the oven has been lifted to show the sample holder.

the relative gas partial pressure, has been obtained through adequate calibrations using the IG and SRG pressure gauges. During the measurements, the pressure p_{LPS} of the gas in contact with the low pressure side, i.e. the downstream side of the membrane, is always negligible with respect to p_{HPS}.

4.1.2.3. *Detected signal and gas transport parameters.* In this section, we will describe how the gas flux through the membrane can be obtained from measurements of its partial pressure p_{LPS} in the analysis chamber and how permeability, diffusivity and solubility of a gas in the membrane can be obtained from a permeation curve, i.e. from the gas flux signal measured as a function of time.

As already pointed out, the partial pressure p_{LPS} of a gas in the analysis chamber is proportional to the relative QMS signal and can therefore be detected as a function of time. Under our measurements conditions, it has been verified that the factor S_{P}/V is always much larger than $\frac{1}{p_{\mathrm{LPS}}}\frac{dp_{\mathrm{LPS}}}{dt}$. Therefore, equation (4.1.1) can

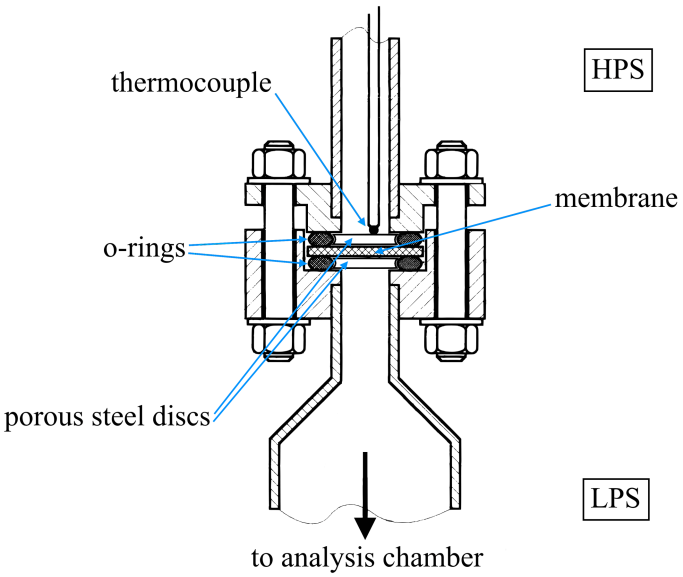

FIGURE 7. A schematic representation of the sample holder of the CP apparatus.

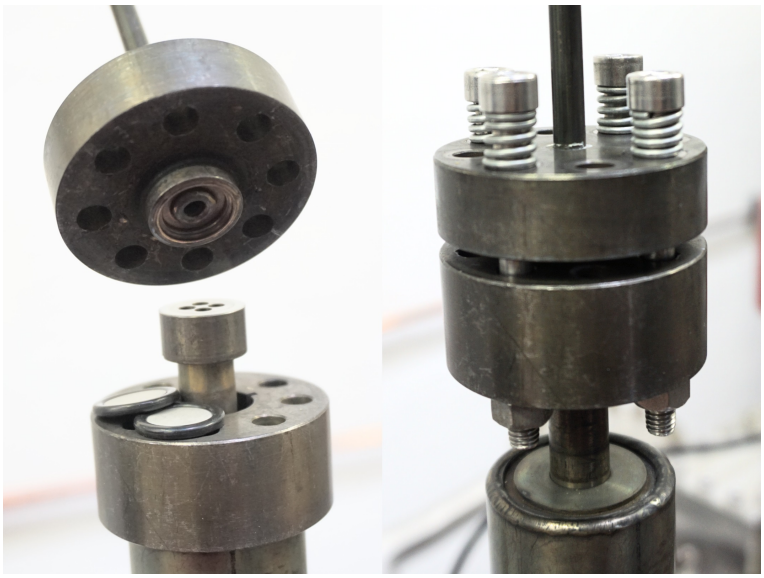

FIGURE 8. The sample holder of the CP apparatus. In the left photograph, the sample holder is opened and the O-rings and porous steel supports are shown. The photograph at right shows the closed sample holder.

be simplified and combined with equation (4.1.2) giving

$$J(t) = \frac{S_{\mathrm{P}}}{ART_a}\, p_{\mathrm{LPS}}(t) \tag{4.1.6}$$

S_P has been measured for all test gases by calibration with a reference sample of known permeability.

In analogy with the case of the experiments in CV conditions, the experimentally measured flux $J'(t)$ is the sum of the actual permeation flux $J(t)$ and a contribution $J_{bck}(t)$ due to small leaks, backflow through the pump and wall desorption:

$$J'(t) = J(t) + J_{bck}(t) \tag{4.1.7}$$

This latter contribution acts as a background signal and needs to be subtracted. $J_{bck}(t)$ is typically constant in the timeframe of the permeation measurements and it can be determined before each experimental run as the signal recorded by setting $p_{HPS} = 0$ and therefore $J(T) = 0$. We define the signal to noise ratio in the measurements performed at constant pumping as $I/\delta I_{bck}$, with δI_{bck} being the fluctuations of the background signal I_{bck}. The detection limit of the system is given by $J = \frac{\delta I_{bck}}{ART_a}$ and it depends on the gas of interest.

Knowing the flux in stationary transport conditions (stc), $J(t \to \infty) = J^{stc} = const$, the permeability P of the membrane is readily calculated using the definition:

$$P = J^{stc}\frac{\ell}{(p_{HPS} - p_{LPS})} \simeq J^{stc}\frac{\ell}{p_{HPS}} \tag{4.1.8}$$

To obtain the diffusivity D of the gas in the membrane, the permeation curves (i.e. the experimental plots of J vs time) can be fitted reminding equation (2.1.13) in section 2.1.3, which can also be written as

$$\frac{J(t)}{J^{stc}} = 1 + 2\sum_{n=1}^{\infty}(-1)^n e^{-\frac{Dn^2\pi^2 t}{\ell^2}} \tag{4.1.9}$$

Finally, the solubility S of a gas in a membrane can be calculated knowing its diffusivity and permeability and using the relation $P = SD$.

Thanks to the high sensitivity of the QMS to small gas fluxes, the CP technique is used when the studied membranes have small permeability. In this thesis work, it was the technique of choice for the determination of the gas transport properties of nanocellulose-based films.

4.2. Positron Annihilation Lifetime Spectroscopy

4.2.1. Physical background. The free volume in polymers can be studied by Positron Annihilation Lifetime Spectroscopy (PALS), a powerful technique that uses positrons (e^+) as probes to analyze nanometer-sized voids (Nakanishi and Jean, 1988; Mogensen, 1995). When a positron is injected in a polymer, it can annihilate as a free positron, or it can form positronium (Ps) with an electron of the polymer. Positronium is the bound state of a positron and an electron and it exists in two states: the triplet state is called *ortho*-Ps (*o*-Ps), the singlet state is called *para*-Ps (*p*-PS). (Yampolskii and Shantarovich, 2006) In solids, *o*-Ps gets trapped in low electron density regions such as the free volume elements. Here, it

can annihilate with an electron belonging to the "walls" of the hole having opposite spin, via the so-called pick-off mechanism. This process reduces the lifetime of *o*-Ps from 142 ns in vacuum to lifetimes τ_3 in the range of approximately 1 to 10 ns in condensed matter. *p*-Ps, conversely, has the same lifetime of 125 ps in matter and in vacuum (Consolati and Quasso, 2010). To summarize, the annihilation spectra of positrons in polymers have typically three components: (i) *p*-Ps annihilation (lifetime $\tau_1 = 125$ ps, intensity I_1), (ii) annihilation as free positrons (lifetime $\tau_2 = 0.3-0.4$ ns, intensity I_2), (iii) pick-off annihilation of *o*-Ps (lifetime $\tau_3 \approx 1-10$ ns, intensity I_3) (Yampolskii and Shantarovich, 2006). The τ_3 lifetime depends on the size of the cavity containing the *o*-Ps: the smaller the cavity, the shorter the lifetime. Furthermore, from the associated intensity I_3, information on the number density of cavities can be obtained. Several models exist, which allow to predict the size of the probed cavities given their shape and the average lifetime of *o*-Ps in the material (Consolati and Quasso, 2010; Mallon, 2003; Jean, 1995). The most relevant ones for the purposes of the present study will be presented later.

4.2.2. Experimental setup. The positron source commonly used is ^{22}Na: a radioactive isotope of Na which undergoes β^+ decay to ^{22}Ne with the emission of a positron and a 1274 keV γ-ray. The source is sandwiched between two polymer samples in such a way that the positrons generated by the source immediately enter the polymer. The annihilation of *o*-Ps with an electron of the polymer results in two γ-rays with energy of 511 keV. The 1274 keV and 511 keV photons are detected by photomultiplier tubes (PMT). In particular, the 1274 keV γ, emitted in the moment of the "birth" of the positron, acts as start signal. Each time a photon with this energy is detected by the PMT, a fast timing signal is generated by a constant fraction discriminator (CFD), which starts a time to amplitude converter (TAC). The voltage ramp of the TAC is stopped by the signal of a second CFD when a 511 keV photon, generated by the annihilation of the *o*-Ps, is detected. The output signal of the TAC is then converted to a digital signal by an analog to digital converter and sent to a computer. The obtained experimental spectrum is a histogram, given by the convolution of the intrinsic spectrum and a resolution function, which describes the response of the setup to the detection of two simultaneous photons. The resolution function can be determined by calibration with sources, such as ^{60}Co, which decay emitting two photons in a time interval short enough to be considered zero, for details see (Consolati and Quasso, 2010).

The setup used in this study has a time resolution function with full width at half maximum (FWHM) of 260 ps, as determined by calibration with a ^{60}Co source. The spectra were stored by means of a multi-channel analyzer with 25 ps per channel. The source was ^{22}Na (15 µCi), deposited between two Kapton foils with thickness of 7 µm. During the analyses, the samples were kept under vacuum ($\sim 10^{-5}$ Pa) at temperatures between 183 K and 343 K. Spectra were acquired at

temperature intervals of 10 K. Each spectrum consists of $\sim 3 \times 10^6$ annihilation events and required 16 h for the acquisition, it was recorded every 4 h. No variation in I_3 was observed at fixed temperature as a function of time: charging effects in the analyzed samples are negligible (Cangialosi et al., 2003; Qi et al., 2001). A Silicon crystal was used as a reference to evaluate the fraction of positrons annihilating in the source or in the Kapton foils. A source component of 12% was found, with a lifetime of 0.382 ns.

4.2.3. Spectra and lifetime measurement. As already said, the experimental spectrum $S^{\mathrm{e}}(t)$ is given by the convolution of a resolution function $R(t)$ and the intrinsic spectrum $S^{\mathrm{i}}(t)$:

$$S^{\mathrm{e}}(t) = R(t) \otimes S^{\mathrm{i}}(t). \tag{4.2.1}$$

In the case of polymers, the most common way to analyze a spectrum is to treat it as a sum of N discrete components (usually $N = 3$) with lifetime τ_i and intensity I_i:

$$S^{\mathrm{e}}(t) = R(t) \otimes \left[\sum_i^N \frac{I_i}{\tau_i} \exp\left(\frac{-t}{\tau_i}\right) + B^{\mathrm{c}} \right] \tag{4.2.2}$$

where B^{c} is a constant background due to spurious coincidence events. Several software packages exist for the analysis of the experimental spectra and allow to deconvolute the resolution function, subtract the background and the contribution to the spectrum given by positrons annihilating within the source, and finally fit the spectrum to find the values for τ_i and I_i (Consolati and Quasso, 2010). As we already said, the annihilation lifetime τ_3 of *o*-Ps gives information on the average size of the probed holes. A further step can be done to obtain a distribution of *o*-Ps lifetime, and hence of hole sizes. This can be done assuming a log-normal distribution $L_{\mathrm{n}}(\lambda)$ of lifetimes, i.e. a gaussian distribution on a logarithmic scale, where $\lambda = 1/\tau$:

$$L_i(\lambda) = \frac{1}{\sqrt{2\pi}\lambda\sigma_i^*} \exp\left[-\frac{(\ln\lambda - \ln\lambda_{i0})^2}{2\sigma_i^{*2}} \right] \tag{4.2.3}$$

where the standard deviation σ_i^* of the distribution $L_i(\lambda)$ and its maximum λ_{i0} are free fit parameters. The relevant parameters are the mean lifetime τ_i and the standard deviation σ_i of the lifetime distribution $L_i(\tau)d\tau = L_i(\lambda)\lambda^2 d\lambda$ (Dlubek, 2010). For this work, the software LT9.0 (Kansy, 1996) was used to obtain the mean lifetimes and the corresponding distributions.

CHAPTER 5

Influence of molecular packing and free volume on the gas transport properties of amine-modified epoxy resins

5.1. Introduction

Epoxy resins are crosslinked polymers which are prepared by a crosslinking process between epoxides and curing agents, as discussed in section 3.1. These polymers exhibit interesting properties for applications, such as high chemical and thermal resistance and good mechanical properties. They have industrial applications in a wide range of fields, including adhesives, metal coatings, high tension electrical insulators and flame retardant materials (Pascault et al., 2012). There is still a great interest in the study and development of epoxy resins because their structural properties can be modified in order to meet the requirements for specific applications (Tian et al., 2016; Patel et al., 2016; Harada et al., 2016). The tuning of these polymers' properties can be obtained in many different ways, such as modifying the extent of the curing reaction (Jordan et al., 1992), using mixed epoxides and curing agents (Okabe et al., 2013), changing the stoichiometric ratio between epoxide and curing agent (Calventus et al., 2001) or suitably choosing epoxide molecules with an aromatic or aliphatic backbone chain (Urbaczewski-Espuche et al., 1991). A further way to tune the materials properties is to change the crosslink density X (George and Thomas, 2001; Lin et al., 2005). Indeed, the crosslink density affects polymer chain packing and hence influences the free volume structure of the material (Liu et al., 2009). The change in crosslink density thus affects the gas transport properties of the materials.

In this chapter, we will present a study on the correlation between the crosslink density, the free volume structure and the gas transport properties of amine-modified epoxy resins. Gas permeability, solubility and diffusivity in the epoxy resins at different crosslink density are measured as a function of temperature and correlated to the evolution of the fractional free volume as it changes with crosslink density. In this work, the value of the fractional free volume of the epoxy samples was obtained experimentally.

The studied materials are four epoxy resins obtained by reacting the same epoxide (NeoPentyl Glycol Diglycidyl Ether, NPGDE) with four polyether diamines having different chain length; see section 3.1 for details on the sample preparation and

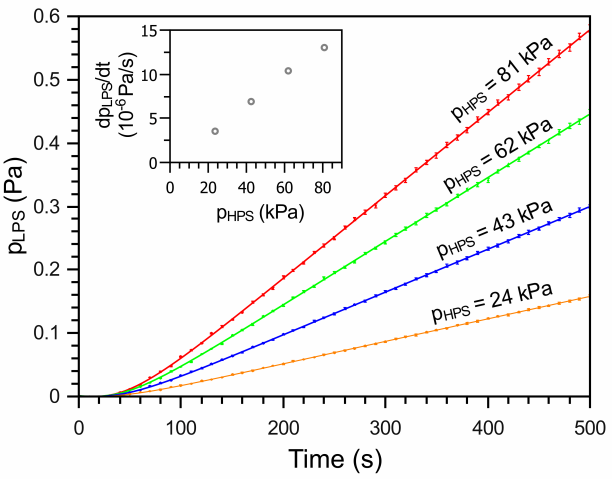

FIGURE 1. p_{LPS} pressure in the analysis chamber as a function of time (see chapter 4.1.1), for CO_2 permeation through NPGED-900 at $T = (336 \pm 1)\,\mathrm{K}$ for different p_{HPS} pressures. The lines are the fits to equation (2.1.17). In the inset, the pressure increase rate in stc dp_{LPS}/dt in the analysis chamber is plotted against p_{HPS}. The experimental error is smaller than the symbols used to represent the data.

characterization. The choice of these materials allowed to prepare four polymers having different crosslink densities, but maintaining similar chemical environment for the migrating particles. The test gases used for this study are CO_2, N_2 and H_2 and have different molecular size and condensation properties (see Table 1 in chapter 4). The gas transport properties of the membranes have been experimentally studied by a gas phase permeation technique, see section 4.1.1, and their free volume structure was analyzed by PALS, see section 4.2.

5.2. Gas transport and free volume

5.2.1. Gas diffusivity and solubility in the epoxy resins. The gas permeation measurements were carried out using a gas phase permeation technique in constant volume configuration: the apparatus and the procedure are described in section 4.1.1. The measurements were carried out at temperatures between approx. 290 K and 370 K, using CO_2, N_2 and H_2 as test gases and with p_{HPS} values up to $\sim 100\,\mathrm{kPa}$.

The CO_2 permeation curves through NPGED-900 at $T = 336\,\mathrm{K}$ are reported in Figure 1. The slope of the curves in stationary transport conditions (stc) is directly proportional to p_{HPS} (see inset), as indicated by the relation $J^{\mathrm{stc}} = D\,S\,p_{\mathrm{HPS}}/\ell$ (see equation (2.1.11)), remembering that in the present experimental conditions, $\Delta p \simeq p_{\mathrm{HPS}}$), and indicates that permeation in these samples obeys the solution

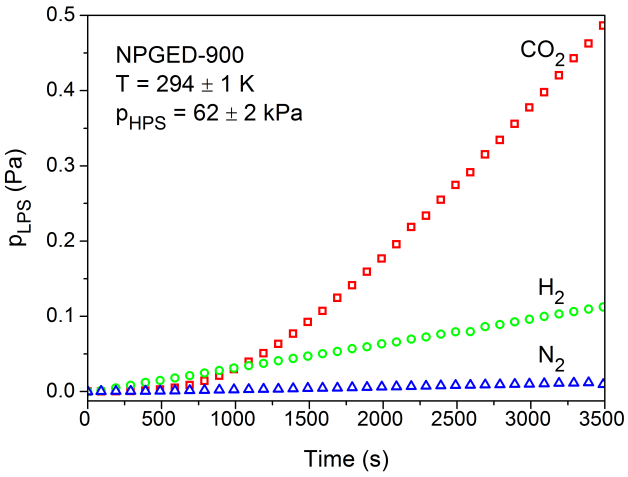

FIGURE 2. Permeation curves of the three test gases in NPGED-900.

diffusion model, since the solution process follows Henry's law. The figure also shows equivalent timelag θ values for each curve, suggesting that D does not depend on gas concentration in the membrane.

The permeation curves for NPGED-900 obtained at (294 ± 1) K with p_{HPS} = (62 ± 2) kPa with the three gases are shown as an example in Figure 2. This figure shows that the CO_2 permeability is larger than that of N_2 and that H_2 has intermediate permeability values. The timelag of the CO_2 permeation curve is well measurable, whereas it cannot be measured for N_2 and H_2. In the case of H_2, the timelags are too short to be measured, also al low temperature. Moreover, due to the low permeability of N_2 in these membranes and therefore to the poor signal to noise ratio, no diffusivity could be measured for this gas.

Figure 3 reports the Arrhenius plots of the gas permeability values with large enough signal to noise ratio (SNR>5). Curves in Figure 3 were fitted to the relation $P = P_0 \exp\left(-\frac{E_P}{RT}\right)$ (see equation (2.1.29)), to obtain the apparent activation energy value for permeation E_P. The obtained values are reported in Table 1. The selectivities $\alpha_{\mathrm{A/B}} = P_{\mathrm{A}}/P_{\mathrm{B}}$ of the studied membranes were calculated and are reported in Table 2. The obtained experimental data indicate that:

(1) the permeability values decrease with increasing crosslink density;
(2) the apparent activation energy for permeation increases with increasing polymer crosslink density (this effect is particularly evident for CO_2);
(3) the CO_2/N_2 as well as the CO_2/H_2 selectivity values increase with increasing crosslink density.

Permeation in these samples occurs via solution-diffusion mechanism, therefore, it is useful to separately analyze the gas solubility and diffusivity as a function of

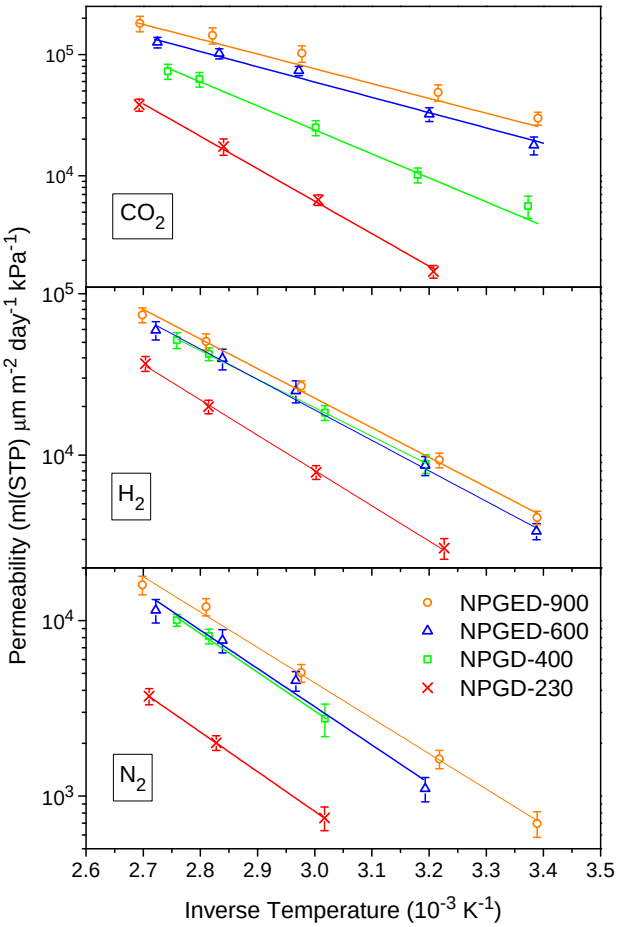

FIGURE 3. Arrhenius plots of the permeabilities of the three test gases in all studied epoxy membranes.

sample	E_P (CO_2) (kJ/mol)	E_P (H_2) (kJ/mol)	E_P (N_2) (kJ/mol)
NPGD-230	51 ± 2	41.9 ± 0.8	44.0 ± 0.4
NPGD-400	38 ± 2	33.5 ± 0.8	43 ± 1
NPGED-600	24 ± 3	36 ± 1	42 ± 4
NPGED-900	21 ± 2	35 ± 1	38 ± 3

TABLE 1. Apparent activation energies for the permeation of the three test gases.

crosslink density. To this task, the D and S values of CO_2 were obtained from the analysis of the permeation curves measured between $T = 290\,\mathrm{K}$ and $T = 370\,\mathrm{K}$.

sample	α_{CO_2/H_2}	α_{CO_2/N_2}	α_{H_2/N_2}
NPGD-230	0.80 ± 0.04	8.4 ± 0.4	10.4 ± 0.5
NPGD-400	1.4 ± 0.2	4.5 ± 0.6	3.3 ± 0.4
NPGED-600	2.9 ± 0.2	16 ± 1	5.5 ± 0.4
NPGED-900	3.9 ± 0.4	20 ± 2	5.3 ± 0.5

TABLE 2. Membrane selectivities at $T = (336 \pm 1)\,\mathrm{K}$.

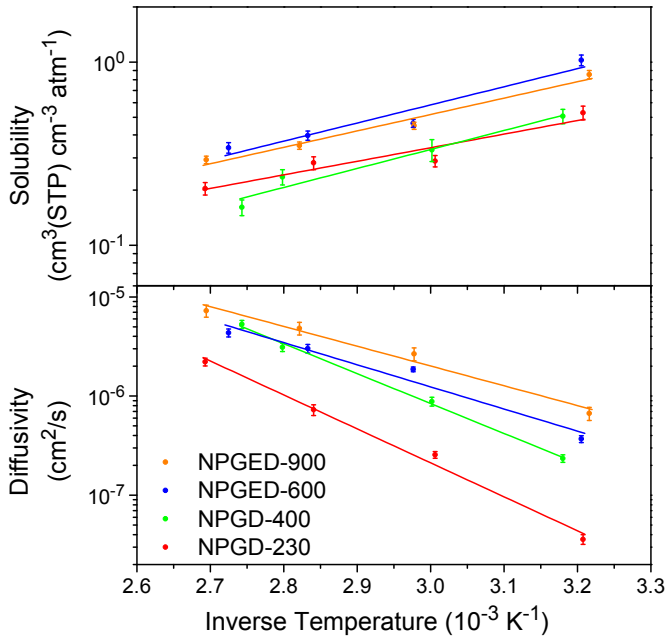

FIGURE 4. Arrhenius plots of solubility and diffusivity of CO_2 in all studied samples.

Specifically, D was obtained by fitting the permeation curves to equation (2.1.17) and S was then evaluated by the relation $P = SD$.

The Arrhenius plots for these two quantities are reported in Figure 4. Diffusivity data are reported in the lower panel of the figure. The plots show that the CO_2 diffusion coefficient strongly depends on X: at fixed temperature, D increases by decreasing the crosslink density. For example, at $T \simeq 312\,\mathrm{K}$ it increases from NPGD-230 to NPGED-900 by a factor of approx. 20. On the other hand, S is less dependent on crosslink density and there is no clear trend between S and X (as an example, the ratio between the highest and the lowest measured solubilities is not more than 2). The apparent activation energy for diffusion E_D and the enthalpy of

sample	E_D (kJ/mol)	ΔH_S (kJ/mol)
NPGD-230	67 ± 4	-14 ± 3
NPGD-400	58 ± 2	-20 ± 3
NPGED-600	42 ± 4	-20 ± 3
NPGED-900	38 ± 4	-18 ± 1

TABLE 3. CO_2 apparent activation energies E_D and sorption enthalpies ΔH_S in the studied samples.

sorption ΔH_S have been calculated by fitting the data in Figure 4, to the equations:

$$D = D_0 \exp\left(\frac{-E_D}{RT}\right) \qquad S = S_0 \exp\left(\frac{-\Delta H_S}{RT}\right) \tag{5.2.1}$$

which were discussed in section 2.1.6. The obtained values are reported in Table 3, which clearly shows that the apparent activation energy for diffusion increases with increasing crosslink density, whereas the enthalpy of sorption is equivalent inside the experimental indetermination, indicating that the crosslink density determines the gas transport rates of these samples only by changing the gas diffusion process. The fact that the enthalpy of sorption does not change in the different samples is compatible with the fact that the membranes have similar chemical structure, i.e. the interaction between the penetrant molecules and the chemical environment is the same in all samples.

On the other hand, it can be argued that the free volume structure of the samples depends on the crosslink density. Vrentas and Vrentas (1991) suggest indeed that the crosslinking affects the specific hole free volume of the polymer, which in turn determines the diffusivity, as discussed in section 2.3.1.

To this task, detailed investigation on the free volume structure of the polymers was carried out by PALS.

5.2.2. Positron Annihilation Lifetime Spectroscopy analysis. PALS analysis (see section 4.2 for a description of the technique and the experimental details) was performed on all epoxy samples. PALS spectra were acquired at temperatures between 183 K and 343 K at temperature intervals of 10 K. As an example, the PALS spectrum for NPGED-900 at 313 K is plotted in Figure 5. The spectra were analyzed with Patfit-88 (Kirkegaard et al., 1989) and LT9.0 (Kansy, 1996) to obtain three lifetimes $\tau_1 < \tau_2 < \tau_3$ and the corresponding intensities and distributions. Fitting was performed by fixing the p-Ps lifetime τ_1 value at 125 ps. With this constraint, the χ^2 values lie between 1.01 and 1.11. The obtained τ_2 values increase from (0.344 ± 0.002) ns at 183 K to (0.399 ± 0.002) ns at 343 K. The free volume structure of the polymer samples is described by the τ_3 values and the corresponding intensity I_3. τ_3 is indeed connected to the volume of the holes and I_3 to their number density.

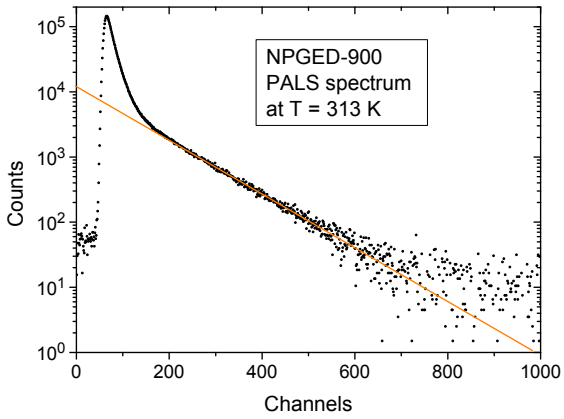

FIGURE 5. The PALS spectrum for NPGED-900 at 313 K. The orange line is a representation of the fitting line from which τ_3 is obtained.

Assuming that the free volume elements are spherical holes, their radius R was obtained using the Tao-Eldrup equation (Tao, 1972; Eldrup et al., 1981):

$$\tau_3 = 0.5 \left[1 - \frac{R}{R + \Delta R} + \frac{1}{2\pi} \sin\left(\frac{2\pi R}{R + \Delta R} \right) \right]^{-1} \tag{5.2.2}$$

where ΔR is the empirical electron layer thickness. Figure 6 shows the average τ_3 values, the hole size $v_\mathrm{h} = \frac{4}{3}\pi R^3$, the standard deviation σ_3 of the lifetime τ_3 and the relative intensity I_3 as functions of temperature for NPGED-900. This figure permits to obtain the glass transition temperature, as seen by PALS, as the intersection between the two straight lines fitting the v_h values in glassy and rubbery phase (Baker, 2004). T_g has been calculated for all samples and the obtained values are reported in Table 4. The intensity I_3, proportional to the number density of the holes (Mallon, 2003), shows an increase of the order of 10% in the studied temperature range. The same behavior was observed for all samples, meaning that the number density of the holes is unaffected by the crosslink density. The volume v_h increases much more markedly, i.e. from $\sim 0.05\,\mathrm{nm}^3$ to $\sim 0.16\,\mathrm{nm}^3$ in the rubbery phase. We can therefore conclude that the change of the free volume with temperature is determined by the thermal expansion of the free volume holes rather than by an increase on the hole number density. σ_3 is independent on temperature for $T < T_\mathrm{g}$, while it increases slightly with temperature in rubbery state, with a slope of $(3.1 \pm 0.2) \times 10^{-4}\,\mathrm{ns\,K^{-1}}$.

Note that for the NPGED-900 sample, the τ_3 curve shows a "knee", where it loses linearity at temperatures above T_g+80 K. This effect can be explained in terms of structural relaxation of polymer chain segments. If the structural relaxation time is similar or shorter than τ_3, the walls of the holes can move while Ps is contained

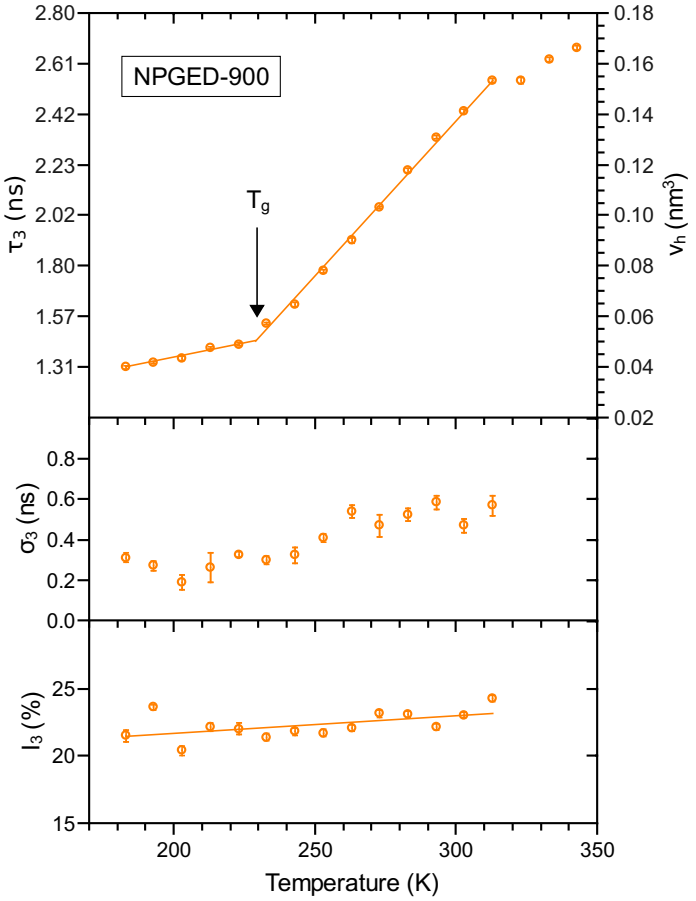

FIGURE 6. Average *o*-Ps lifetime τ_3 and hole size v_h (upper panel), standard deviation σ_3 of the lifetime τ_3 (middle panel) and relative intensity I_3 (lower panel) as functions of temperature for NPGED-900. The lines are linear fits of the data.

in the hole itself, effectively reducing the probed volume (Dlubek et al., 2006, 2008; Pethrick et al., 1980; Malhotra and Pethrick, 1983). Anyway, the τ_3 and v_h values in this temperature range can be obtained by extrapolation (Dlubek et al., 2006).

Figure 7 shows the τ_3 and v_h values for all samples, plotted against the sample temperature. The figure shows that, at fixed temperature, v_h decreases for increasing crosslink density. The average volume v_h of the holes depends linearly on temperature. In the glassy phase, its temperature dependence can be expressed as follows:

$$v_h(T) = v_h(0) + \left(\frac{dv_h}{dT}\right)_g T \qquad \text{for } T < T_g \tag{5.2.3}$$

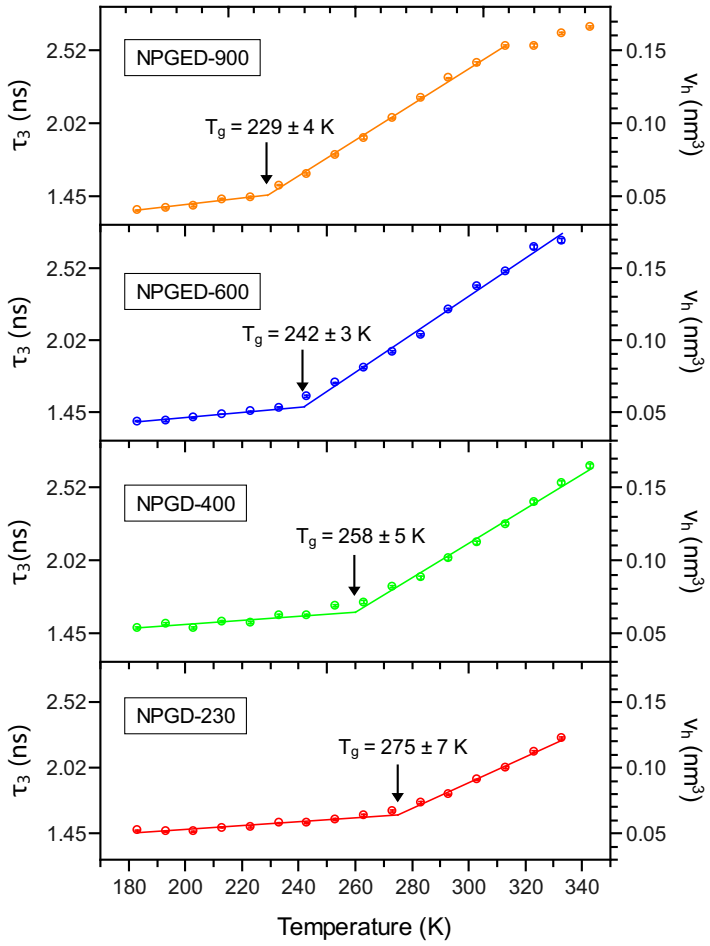

FIGURE 7. τ_3 and corresponding v_h values for all samples, as functions of temperature.

where $(\mathrm{d}v_\mathrm{h}/\mathrm{d}T)_\mathrm{g}$ is the free volume expansivity in glassy state and $v_\mathrm{h}(0) \simeq 2 \times 10^{-2}$ nm^3 is the static hole volume at $T = 0$ K. In the rubbery state, v_h is given by

$$v_\mathrm{h}(T) = v_\mathrm{g} + \left(\frac{\mathrm{d}v_\mathrm{h}}{\mathrm{d}T}\right)_\mathrm{r} (T - T_\mathrm{g}) \qquad \text{for } T > T_\mathrm{g} \tag{5.2.4}$$

where $(\mathrm{d}v_\mathrm{h}/\mathrm{d}T)_\mathrm{r}$ is the free volume expansivity in rubbery state and v_g is the average hole volume at the glass transition temperature. It can be obtained as the intersection between the lines given by equations (5.2.3) and (5.2.4). The coefficient of thermal expansion of the hole free volume in glassy phase (α_hg) and in rubbery phase (α_hg) are defined in the following way:

$$\alpha_\mathrm{hg} = \frac{1}{v_\mathrm{g}} \left(\frac{\mathrm{d}v_\mathrm{h}}{\mathrm{d}T}\right)_\mathrm{g} \qquad \text{for } T < T_\mathrm{g} \tag{5.2.5}$$

and

$$\alpha_\mathrm{hr} = \frac{1}{v_\mathrm{g}} \left(\frac{\mathrm{d}v_\mathrm{h}}{\mathrm{d}T}\right)_\mathrm{r} \qquad \text{for } T > T_\mathrm{g}. \tag{5.2.6}$$

The values of α_{hg} are in the range between $\sim 2 \times 10^{-3}\,K^{-1}$ for NPGD-230 and $\sim 4 \times 10^{-3}\,K^{-1}$ for NPGED-900. The values of v_g, $(dv_h/dT)_r$, α_{hr}, T_g and I_3 for all samples are reported in Table 4. To summarize the data shown in Figs. 6 and 7 and in Table 4, we can say that:

(1) I_3 depends very weakly on temperature and does not depend on the crosslink density;
(2) v_h depends linearly on temperature, both above and below T_g. In rubbery phase the hole volume, rather than the hole number density, determines the free volume evolution with temperature;
(3) at fixed temperature, v_h decreases with increasing crosslink density.

5.2.3. Fractional free volume evaluation. The fractional free volume was defined in section 2.3.1. It can be evaluated starting from PALS measurements: indeed, it is proportional to the average hole volume v_h and the intensity I_3 of the *o*-Ps annihilation signal (Wang et al., 1990; Jean et al., 2013).

$$f(T) = CI_3(T)v_h(T) \tag{5.2.7}$$

C is a constant connected to the probability of formation of *o*-Ps and depends on the specific polymer. Since I_3 and v_h have been measured, only C needs to be estimated. In the following, we will do so without specific assumptions, finding an equation allowing to calculate f based only on measurable quantities. The fractional free volume at the glass transition temperature f_g can be evaluated by:

$$f_g = f(T = T_g) = \alpha_V/\alpha_{hr} \qquad \text{for } \alpha_V \ll \alpha_{hr} \tag{5.2.8}$$

which holds when the volumetric thermal expansion coefficient α_V of the polymer is much smaller than the coefficient of the thermal expansion of the hole free volume (Hristov et al., 1996).

To verify this condition, α_V was measured by dilatometry experiments. As shown in section 3.1.2.4, the measurements produced indistinguishable values: we thus evaluated the α_V average value and its indetermination as the semi-dispersion around the value $\alpha_V = (5.6 \pm 0.1) \times 10^{-4}\,K^{-1}$.

Since the α_{hr} values are in the range of $10^{-2}\,K^{-1}$, see Table 4, the above condition is fulfilled and we can conclude that the variations of the total volume of the studied polymers are due to changes in the hole free volume (Hristov et al., 1996). The obtained f_g values are reported in Table 4. Using equation (5.2.7) at T_g and equation (5.2.6) and (5.2.8), the following expression for C can be obtained:

$$C = \frac{\alpha_V}{I_3(T_g)} \left(\frac{dv_h}{dT}\right)_r^{-1} \tag{5.2.9}$$

The obtained values are reported in Table 4. Inserting the above equation in equation (5.2.7),

$$f(T) = \alpha_V \frac{I_3(T)}{I_3(T_g)} v_h(T) \left(\frac{dv_h}{dT}\right)_r^{-1} \tag{5.2.10}$$

	NPGD-230	NPGD-400	NPGED-600	NPGED-900
v_g (nm^3)	$(6.4 \pm 0.4) \times 10^{-2}$	$(6.2 \pm 0.3) \times 10^{-2}$	$(5.3 \pm 0.2) \times 10^{-2}$	$(5.1 \pm 0.2) \times 10^{-2}$
$\left(\frac{dv_h}{dT}\right)_r \left(\frac{nm^3}{K}\right)$	$(0.98 \pm 0.01) \times 10^{-3}$	$(1.18 \pm 0.01) \times 10^{-3}$	$(1.31 \pm 0.01) \times 10^{-3}$	$(1.24 \pm 0.01) \times 10^{-3}$
α_{hr} (K^{-1})	$(1.54 \pm 0.09) \times 10^{-2}$	$(1.90 \pm 0.09) \times 10^{-2}$	$(2.47 \pm 0.09) \times 10^{-2}$	$(2.43 \pm 0.08) \times 10^{-2}$
T_g (K)	275 ± 7	258 ± 5	242 ± 3	229 ± 4
I_3 (%)	24 ± 1	25 ± 1	24 ± 1	23 ± 1
f_g	$(3.7 \pm 0.2) \times 10^{-2}$	$(2.9 \pm 0.1) \times 10^{-2}$	$(2.3 \pm 0.1) \times 10^{-2}$	$(2.3 \pm 0.1) \times 10^{-2}$
C (nm^{-3})	2.4 ± 0.2	1.9 ± 0.2	1.8 ± 0.1	2.0 ± 0.1

TABLE 4. Some of the most relevant parameters on the free volume structure of the studied epoxy resins, as evaluated by PALS: average hole volume at the glass transition temperature v_g; hole volume expansivity $\left(\frac{dv_h}{dT}\right)_r$ in rubbery state, volumetric thermal expansion coefficient of the holes α_{hr} in rubbery state, glass transition temperature T_g as determined by PALS, fractional free volume f_g at the glass transition temperature, C constant.

Remembering equation (5.2.4) for v_h in rubbery phase, we obtain

$$f(T) = \alpha_\mathrm{V} \frac{I_3(T)}{I_3(T_\mathrm{g})} \left[v_\mathrm{g} + \left(\frac{\mathrm{d}v_\mathrm{h}}{\mathrm{d}T} \right)_\mathrm{r} (T - T_\mathrm{g}) \right] \left(\frac{\mathrm{d}v_\mathrm{h}}{\mathrm{d}T} \right)_\mathrm{r}^{-1} \qquad \text{for } T > T_\mathrm{g} \tag{5.2.11}$$

which can also be written as

$$f(T) = \frac{I_3(T)}{I_3(T_\mathrm{g})} \left[\frac{\alpha_\mathrm{V}}{\alpha_\mathrm{hr}} + \alpha_\mathrm{V}(T - T_\mathrm{g}) \right] \qquad \text{for } T > T_\mathrm{g} \tag{5.2.12}$$

This is an original equation, its value lies in the fact that it permits to evaluate f only relying on experimentally measured quantities and without making any *a priori* assumptions or approximations. In fact, an alternative method often used for the estimation of fractional free volume f of a polymer is the group contribution method suggested by Bondi (1968) and consisting in the estimation of the occupied volume V_o starting from the sum of the Van der Waals volumes $V_{\mathrm{W},i}$ of each group i forming the molecular chains:

$$V_\mathrm{o} = 1.3 \sum_i V_{\mathrm{W},i} \tag{5.2.13}$$

where the packing density factor 1.3 was proposed by Bondi based on the packing density of molecular crystals at 0 K and takes into account the fact that the zero point volume is larger than the molecular volume (Yampolskii and Shantarovich, 2006; Thran et al., 1999). Once V_o has been estimated, f can be obtained by equation (2.3.4). However, the values obtained in this way are only a rough estimation of the fractional free volume, since the group contribution model implies some approximations: (i) the occupied volume V_o is considered independent on temperature; (ii) the packing density factor 1.3 is the same for all polymers; (iii) this additive scheme does not consider peculiarities of the conformations of polymers (Yampolskii and Shantarovich, 2006).

5.2.4. Fractional free volume and gas diffusivity. Figure 8 summarizes the previously discussed results, as it evidences that the crosslink density influences both the diffusivity and the free volume structure, as seen by PALS through T_g. The decrease of T_g with decreasing crosslink density is a consequence of the different chain packing of the samples, and thus of the different free volume structures. Also the diffusion coefficient of CO_2 heavily depends on the free volume structure of the samples.

In the following, we will discuss in detail the relation between free volume structure of the present samples and diffusion properties by analyzing the diffusion coefficient of CO_2 in the analyzed polymers in the framework of the free volume theory for diffusion that was presented in section 2.3. Note that the CO_2 diffusivity values were obtained for temperatures larger than 293 K, so that all samples are in their rubbery state.

Before discussing the measured diffusivity values in the framework of the free volume theory of diffusion, we will verify whether all probed free volume elements

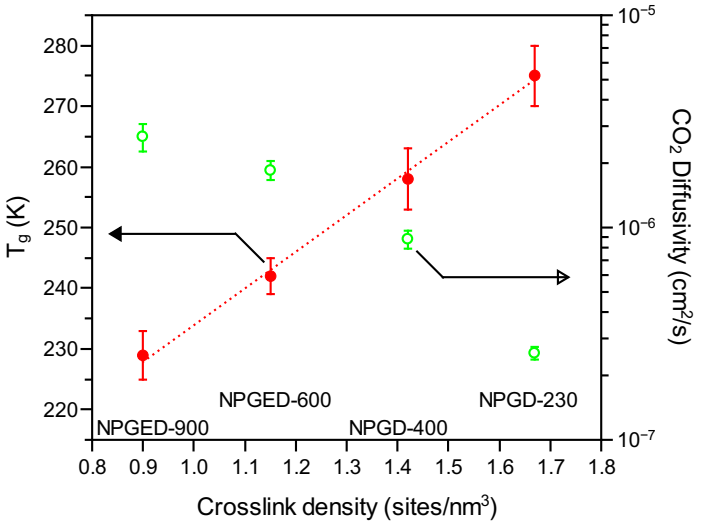

FIGURE 8. T_g as measured by PALS (red full circles) and diffusivity of CO_2 at (334 ± 1) K (green open circles) in the studied membranes, plotted as functions of the calculated crosslink densities. The dotted line is a guide for the eyes.

contribute to CO_2 transport in these polymers. As explained in section 2.3, according to the free volume theory for diffusion, the penetrant molecule can take a diffusive step as soon as a free volume element of sufficient size forms, close to the one containing the diffusant itself. The Lennard-Jones diameter of CO_2 is 0.39 nm and its volume is 0.031 nm^3: let us take this value as an estimate of the minimum hole size needed to accommodate a diffusing CO_2 molecule. Let us define $v_{h,min} = v_h(\tau_3 - \sigma_3)$: this value can be considered as representative for the smallest holes in the holes' distribution. In the case of NPGED-900, in the temperature range at which D was measured, $\sigma_3 \sim 0.4$ ns. In this temperature interval, we obtain $v_{h,min} \simeq 0.1\,nm^3$. For NPGD-230, similarly we obtain $v_{h,min} \simeq 0.05\,nm^3$. We can conclude that even the smallest free volume elements detected by PALS are large enough to accommodate a CO_2 molecule and thus contribute to its diffusion.

To reproduce the measured diffusion coefficients in the framework of the free volume theory for diffusion, the data for D and f in NPGED-900 were fitted to equation (2.3.3), which we remind for the reader's convenience:

$$D = A_D \exp[-B_D/f(T)] \tag{5.2.14}$$

From the fitting, the values $A_D = (2 \pm 1) \times 10^{-3}\,cm^2/s$ and $B_D = 0.58 \pm 0.04$ were obtained. The measured diffusivity data, the $f(T)$ data as calculated from equation (5.2.12) and the fitting curve are reported in Figure 9. This procedure was repeated for the diffusivity of CO_2 in all other samples. The diffusivity data, plotted as a function of the fractional free volume along with the fitting lines obtained

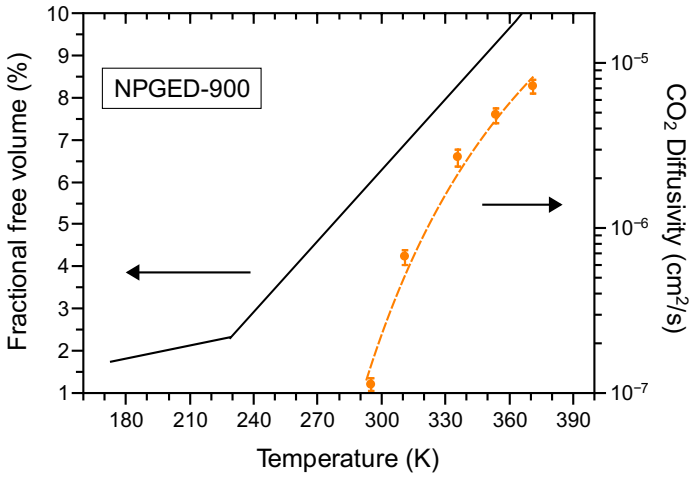

FIGURE 9. Solid lines: f values calculated with equation (5.2.12); dots: CO_2 diffusivity values in NPGED-900; dashed line: fitting of the diffusivity data with equation (5.2.14)

sample	$A_D(\mathrm{cm}^2/\mathrm{s})$	B_D
NPGD-230	$(1.2 \pm 0.1) \times 10^{-3}$	0.58 ± 0.04
NPGD-400	$(3 \pm 1) \times 10^{-3}$	0.58 ± 0.02
NPGED-600	$(4 \pm 2) \times 10^{-3}$	0.60 ± 0.07
NPGED-900	$(2 \pm 1) \times 10^{-3}$	0.58 ± 0.04

TABLE 5. A_D and B_D values obtained from the fits of the CO_2 diffusivity data to equation (5.2.14).

with equation (5.2.14) are reported in Figure 10, whereas the A_D and B_D values obtained by the fits are reported in Table 5. All diffusivity data can be reproduced by equation (5.2.14). All A_D values are in the $10^{-3}\,\mathrm{cm}^2/\mathrm{s}$ order, and B_D is the same for all samples, inside the indeterminations. These findings are explained by the fact that the different crosslink densities correspond to different free volume structures but not to changes in the matrix-penetrant interaction.

Before concluding this discussion, it is worth pointing out the originality of this approach for the analysis of gas transport data by using PALS measurements. In many studies, a linear correlation between $\ln(D)$ and $1/v_\mathrm{h}$ was observed (Kwisnek et al., 2010; Tanaka et al., 2000; Nagel et al., 2002; Xie et al., 2011; Okamoto et al., 1993) and used to conclude whether gas transport was controlled by the free volume structure (Kwisnek et al., 2010; Tanaka et al., 2000). Other studies used the PALS spectra to describe the size distribution of the hole free volumes to complement the information on the free volume structure as obtained, for example, by the calculation of the fractional free volume through theoretical models. This permitted us

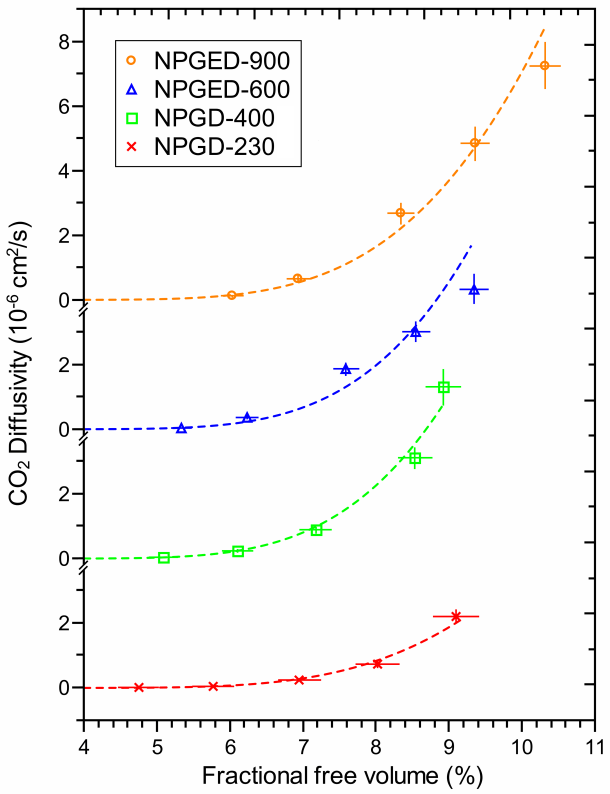

FIGURE 10. CO_2 diffusivity data in all studied samples plotted as functions of the fractional free volume f. The lines are the fits to equation (5.2.14)

to gain information on the accessibility of the free volume holes to the penetrant molecules (Han et al., 2010; Hu et al., 2006; Gringolts et al., 2010; Nagel et al., 2000). In this work, we have evaluated the fractional free volume $f(T)$ by PALS measurements without using any empirical constants or approximations for its theoretical calculation. Knowing the fractional free volume, it was possible, through a well established model for gas diffusion in polymers, to explain the different gas transport rates between epoxy matrices having different free volume structures and to reproduce the behavior of the gas diffusivity as a function of temperature, see Figure 10.

5.2.5. Fractional free volume and gas permeation. In this section we will show that, inside the free volume theory, the permeation properties of the studied epoxy resins can be reproduced for all examined gases.

In the above sections, we described the measured CO_2 diffusivity in the framework of the free volume theory for diffusion, thanks to the experimentally obtained $f(T)$ values, for varying temperature and crosslink densities. In the following we

will describe, using the free volume theory, also the gas permeability of the studied membranes for CO_2, N_2 and H_2.

To do so we remember that, for polymeric membranes, the permeability equals the product between diffusivity and solubility ($P = SD$) and that solubility depends on temperature as stated by the van't Hoff equation:

$$S = S_0 \exp\left(-\frac{\Delta H_S}{RT}\right) \tag{5.2.15}$$

As described in the previous section, the diffusivity is related to the fractional free volume $f = f(T)$ by equation (5.2.14). Consequently, the gas permeability P changes with temperature according to the relation:

$$P = P_0 \exp\left(-\frac{B_D}{f(T)}\right) \exp\left(-\frac{\Delta H_S}{RT}\right) \tag{5.2.16}$$

where $P_0 = A_D S_0$ is a pre-exponential factor. As we saw in section 2.1.6, the solution enthalpy ΔH_S is given by the sum of two contributions: the enthalpy of condensation ΔH_C and the enthalpy of mixing ΔH_M. ΔH_C depends on the condensation properties of the gas, whereas ΔH_M depends on the gas-polymer interaction. If the interaction between the polymer and the penetrant occurs by dispersion forces, then this term is of secondary importance with respect to the condensability term, which dominates. The enthalpy of sorption can therefore be approximated with the enthalpy of condensation: $\Delta H_\mathrm{S} \simeq \Delta H_\mathrm{C} = -\Delta H_\mathrm{V}$ (Matteucci et al., 2006; Krevelen, 1990).

For CO_2 we could experimentally determine the diffusivity and the solubility at each temperature. The enthalpy of sorption could therefore be calculated from the Arrhenius plots of the solubility (see Table 3). It resulted independent on the crosslink density and comparable with the CO_2 heat of condensation at the triple point, 15.3 kJ/mol (Yang et al., 2000), meaning that the enthalpy of mixing only gives a minor contribution to the ΔH_S value. For H_2 and N_2, the solubility could not be measured. Anyway, these gas molecules do not possess a permanent dipole moment, nor they have a quadrupole moment as CO_2, so the interaction with the polymer can be expected to be even lower. Therefore, we can use the approximation $\Delta H_\mathrm{S} \simeq \Delta H_\mathrm{V}$ for H_2 and N_2. The following literature values were chosen: $\Delta H_\mathrm{S} = 5.52$ kJ/mol for N_2 and $\Delta H_\mathrm{S} = 0.92$ kJ/mol for H_2 (Yang et al., 2000), whereas for CO_2 the measured values reported in Table 3 were used.

The experimental permeability data were fitted to equation (5.2.16). The obtained B_D values for N_2 and H_2 are reported in Table 6, together with the values obtained for CO_2 as discussed in section 5.2.4. The permeability data in all samples for the studied test gases are plotted as functions of the inverse fractional free volume ($1/f$) in Figure 11, together with the fitting curves. From the data in Table 6 and in Figure 11, two observations can be made about the B_D parameter:

sample	B_D (CO_2)	B_D (N_2)	B_D (H_2)
NPGD-230	0.58 ± 0.04	0.51 ± 0.04	0.36 ± 0.05
NPGD-400	0.58 ± 0.02	0.51 ± 0.03	0.29 ± 0.04
NPGED-600	0.60 ± 0.07	0.51 ± 0.03	0.37 ± 0.01
NPGED-900	0.58 ± 0.04	0.53 ± 0.03	0.43 ± 0.01
$\langle B_D \rangle$	0.59 ± 0.04	0.51 ± 0.02	0.37 ± 0.03

TABLE 6. B_D values (see equation (5.2.14) and (5.2.16)) for the studied gases.

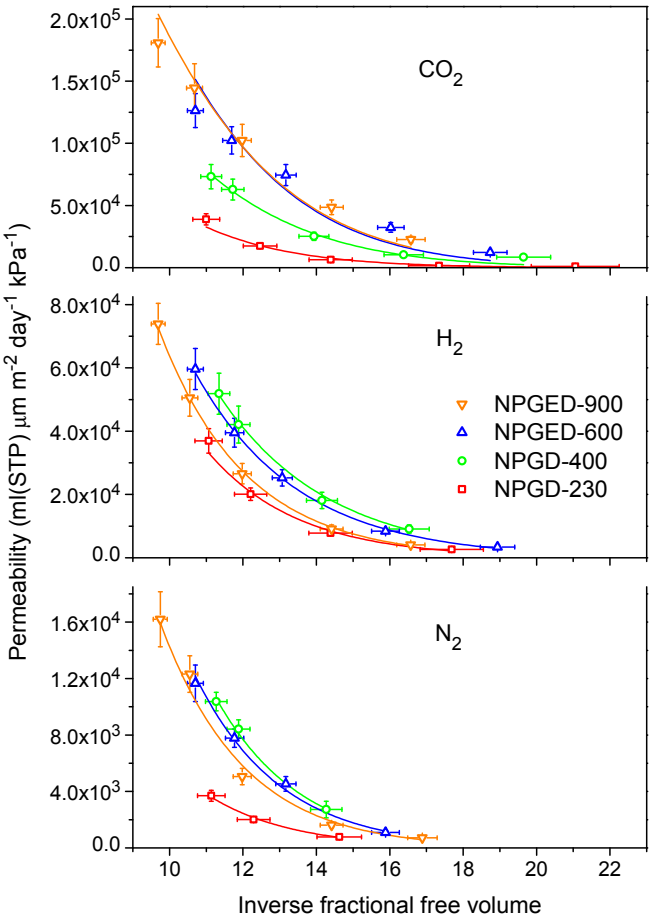

FIGURE 11. Gas permeability of CO_2, H_2, N_2 as a function of inverse fractional free volume $1/f$. The lines represent the best fits with equation (5.2.16) and the parameters in Table 6

(1) for given penetrant molecule, the values for B_D in different matrices are very similar. This evidence suggests that B_D depends on the penetrant-matrix pair but not on the free volume structure of the matrix;
(2) for given crosslink density (i.e. for given polymer matrix), B_D scales with the diffusing molecule's size, in agreement with the theoretical predictions (Duda and Zielinski, 1996; Thran et al., 1999; Vrentas and Duda, 1977).

The data reported in Figure 11 and the fits indicate that the Arrhenius behavior of the permeability can be explained by the linear dependence of f on temperature, as described in equation (5.2.12). Noting also that, given the ΔH_S values reported above, the solubility is not expected to change much in the analyzed temperature range (by a factor of approx. 3 for CO_2 and 1.1 for H_2), we can state that the dominant contribution to the dependence of P on temperature is the diffusivity, which is the only term depending on fractional free volume.

Figure 11 also shows a quite unexpected result: In samples with the same chemical environment for the permeating molecules, at fixed f value, permeability is not the same for all samples and increases with decreasing crosslink density. This effect appears to be dependent on the penetrant size. For example, at $f = 0.08$ ($f^{-1} = 12$), the ratio of the permeability of NPGED-900 to the permeability of NPGD-230 is ~ 5 for CO_2 and ~ 1.5 for H_2. At $f = 0.08$, the temperature for NPGED-900 is 336 K and for NPGD-230 it is 358 K: the permeability of NPGED-900 for $f = 0.08$ is 5 times larger than for NPGD-230 even if the temperature is 20 K lower. From PALS data, we have seen that samples having the same fractional free volume have the same hole number density and the same average hole volume. To explain the behavior of the gas permeability, we need to consider the free volume redistribution. Indeed, as we saw in section 2.3.1, the gas molecule cannot take a diffusion jump until a hole forms close to it because of the thermal motions of the polymeric chains. As qualitatively demonstrated by the fact that the glass transition temperature of the studied polymers increases with increasing crosslink density, the rigidity of the polymeric network increases with increasing X. We infer that the increased rigidity of the more crosslinked samples hinders the free volume redistribution, which indeed depends on the mobility of the polymer chains segments (Noorjahan and Choi, 2015). The higher crosslink density, hence, reduces the probability that a free volume element of sufficient size opens close to the diffusing molecule (Poulsen et al., 2003). This probability is scarcely influenced by temperature since, as explained in sect 2.3.1, hole free volume need negligible thermal energy to redistribute. This explains why, at fixed f value, the permeability of highly crosslinked samples is lower than that in less crosslinked matrices, despite the higher temperature. Unfortunately, the above considerations do not explain why the dependence on X of the permeability at fixed f is more marked for CO_2 than for N_2 and H_2 although, as we have seen above, all free volume elements

are large enough to accommodate all penetrant molecules. We suggest that this effect could be attributed to the interaction between the diffusing molecules and the polymer matrix. This interaction, indeed, is stronger for CO_2 due to its quadrupolar character, whereas it is weaker for the other two molecules.

With the results obtained so far, it is now also possible to discuss the obtained selectivity values, reported in Table 2. The CO_2/N_2 and CO_2/H_2 selectivity decrease with increasing crosslink density. This behavior is a consequence of the stronger reduction of the CO_2 permeability compared with N_2 and H_2 permeability, with increasing X. In turn, the stronger decrease of the CO_2 permeability with increasing X and thus with decreasing f is explained by the value of $\langle B_D \rangle$, which is larger for CO_2 than for N_2 and H_2. In other words, due to the larger $\langle B_D \rangle$ value, which is connected to the molecule's size, CO_2 transport rates are more sensitive to free volume variations.

5.3. Conclusions

We prepared amine-modified epoxy membranes with different crosslink densities by using an aliphatic epoxide and polyether diamines with different chain lengths. The permeation of the studied test gases occurs by solution-diffusion. The differences in the transport properties of the different samples were attributed to variations in the diffusion rates rather than in the gas solubilities.

The dependence of the diffusion rates on the crosslink density, and hence on the polymer structure, have been explained in the framework of the free volume theory for diffusion. The size of the free volume elements and its distribution have been determined by PALS at different temperatures, allowing us to obtain the fractional free volume in all samples in rubbery phase, as a function of temperature, to finally explain the measured CO_2 diffusion coefficients.

The free volume data also allowed us to explain the observed Arrhenius behavior of the permeability for all gases with the linear increase of fractional free volume with temperature. The role of free volume redistribution has also been observed and it explains the dependence of the permeability on the polymers' crosslink density for constant fractional free volume.

CHAPTER 6

Free volume reduction and polymer rigidification in Graphene-based nanocomposite membranes

6.1. Introduction

Nanocomposites comprising high aspect ratio nanoparticles are attracting great interest for applications in the membrane technology. In particular, graphene based nanocomposites have demonstrated great potential in improving the barrier properties of polymer membranes, thanks to the high aspect ratio of graphene and to the high electron density of the carbon rings making up for the graphene sheets, which make it impermeable also to small-size penetrants (Compton et al., 2010; Sadasivuni et al., 2013; Cui et al., 2016). Moreover, nanocomposites based on graphene and graphene-derived materials show enhanced mechanical, thermal and electrical properties (Kim et al., 2010).

Few Layers Graphene (FLG) is a graphene-derived material consisting of nanoplatelets that can be easily obtained by exfoliation of expanded graphite (Novoselov et al., 2012). These nanoplatelets are made of stacks of graphene layers having thickness of few nanometers and lateral size up to 100 µm. Thanks to their lamellar shape with a high aspect ratio, FLG allows the production of membranes showing enhanced gas barrier properties. FLG-based nanocomposites have been reported to have gas barrier properties which are orders of magnitude better than nanoclays at low concentrations (Compton et al., 2010; Sadasivuni et al., 2013).

In the previous chapters, we have well characterized the structural and gas transport properties of amine-modified epoxy resins. For this work, we have used one of these resins (NPGED-900) as a matrix for the preparation of nanocomposite membranes, using different concentrations of FLGs as fillers. The filler loading φ_d (where the index d stands for "dispersed phase") was systematically changed up to ~ 5 vol.% to avoid filler aggregation (Yoo et al., 2014; Potts et al., 2011). The gas transport properties of the obtained PNC membranes were studied by a gas phase permeation technique using three molecules with different kinetic diameters and condensabilities (CO_2, N_2 and H_2, see the T_c and σ_k values in Table 1 in chapter 4) as test gases.

As we saw in chapter 1, the gas transport properties of polymer nanocomposites are influenced by defects formed at the interface between filler and polymer matrix, such as void formation and rigidification at the polymer-filler interface. In this work,

peculiarities in the structure of the nanocomposites were studied by comparing the PALS spectra and DSC measurements of the pure and nanocomposite samples.

In this study, we describe the phenomena occurring at the matrix-filler interface and discuss how they control the gas transport properties of nanocomposite membranes comprising FLGs dispersed in amine-modified epoxy resins.

6.2. Free volume structure of the nanocomposites

We carried out PALS analysis to investigate the changes in the samples' free volume structure due to the dispersion of nanofillers. PALS spectra fitting was carried out by using the same procedure and software packages used for the pure epoxy resin samples, see section 5.2.2. Briefly, the spectra were fitted with three lifetime components ($\tau_1 < \tau_2 < \tau_3$; χ^2 values between 1.00 and 1.21), by fixing the τ_1 value at 125 ps. The obtained τ_2 values are similar to those found in the pure epoxy membranes: in the nanocomposites they range from (0.335 ± 0.002) ns to (0.377 ± 0.002) ns at the examined temperatures. The τ_3 values for the pure and the nanocomposite samples are plotted as functions of temperature in Figure 1 (right vertical axis). The average radius R of the free volume holes was evaluated by assuming them to have spherical shape, as in the case of the pure polymers (see section 5.2.2). The resulting v_h values are plotted in Figure 1, left vertical axis. The v_h values as functions of temperature are well fitted by straight lines, both below and above the glass transition temperature T_g, whose value was obtained from the intersection between the two straight lines. The T_g of the polymer matrix, (229 ± 4) K, does not change after filler addition. This confirms the observations made by DSC, see section 3.2.2.3.

The intensity of the *o*-Ps annihilation signal I_3 is presented as a function of temperature in Figure 2 for samples in rubbery phase.

The data in Figures 1 and 2 indicate that, at each examined temperature, the average free volume v_h does not change after filler addition. On the other hand, I_3 diminishes with increasing filler content. Hence the addition of the fillers changes the free volume structure of the samples not by altering the free volume hole size, but by reducing the number density of the holes and therefore the fractional free volume of the samples, which is proportional to the product $v_\mathrm{h} I_3$ (see equation (5.2.7) in the previous chapter). In the following, we will therefore use the product $v_\mathrm{h} I_3$ as a measure of f itself. The $v_\mathrm{h} I_3$ product is plotted for all samples in Figure 3 as a function of temperature for $T > T_\mathrm{g}$; its values can be well fitted to straight lines in the pure and nanocomposite samples. The difference between the fractional free volume in the nanocomposite and pure samples are quantitatively described by the parameter $r_f(T)$ defined as:

$$r_f(T) = \frac{f_\mathrm{NC}}{f_\mathrm{C}} = \frac{(v_\mathrm{h} I_3)_\mathrm{NC}}{(v_\mathrm{h} I_3)_\mathrm{C}} \tag{6.2.1}$$

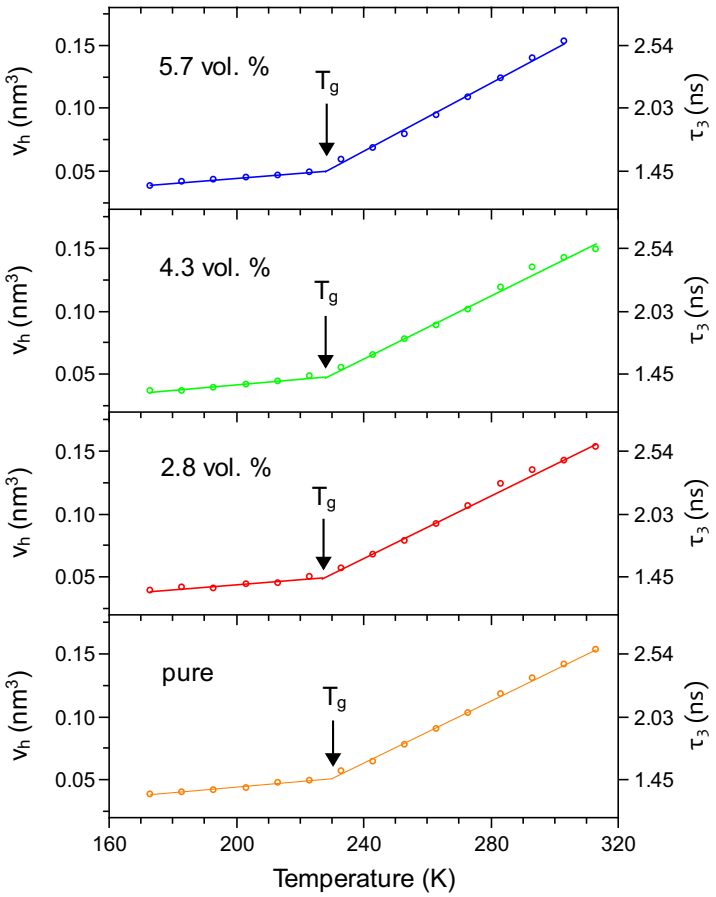

FIGURE 1. o-Ps lifetime τ_3 values (right vertical axes) and average hole volume v_h (left vertical axes) as functions of temperature for the pure epoxy resin and the nanocomposites with different filler concentrations.

where the index NC stands for "nanocomposite" and C for "continuous phase". Three observations can be made looking at the values for r_f: (i) filler addition does not change the fractional free volume for the nanocomposite with an FLG concentration of 2.8 vol.% ($r_f \simeq 1$); (ii) the reduction in f is well evident in samples with filler loadings of 4.3 and 5.7 vol.%, for which $r_f < 1$; (iii) at $T > T_\mathrm{g}$, in the examined samples r_f does not change with temperature.

At this point, it is important to remark that the reduction of fractional free volume in the nanocomposite samples cannot be only attributed to the presence of fillers in the polymer matrix. In fact, if we consider as an example the 4.3 vol.% loaded sample, we observe that the fractional free volume here is reduced by approx. 15 %. This reduction is at least three times larger than the reduction of the polymer specific volume (see insets of Figure 3).

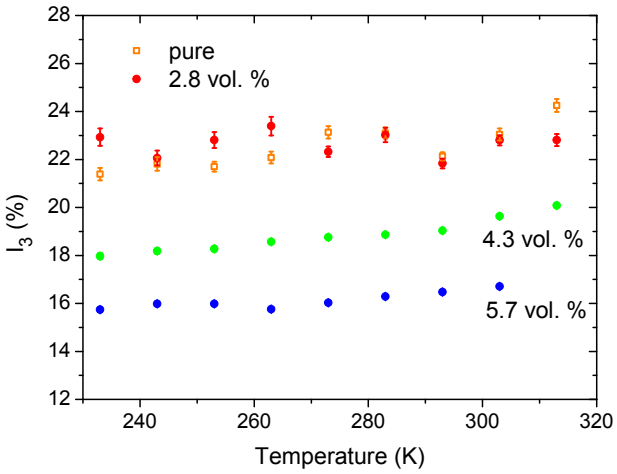

FIGURE 2. o-Ps annihilation signal intensity I_3 as a function of temperature for the pure epoxy membrane and the nanocomposites.

6.3. Gas transport properties in the nanocomposites

The Arrhenius plots of the CO_2, H_2 and N_2 permeabilities in the pure and nanocomposite samples are reported in Figure 4 and indicate that the filler addition decreases the gas permeability. The ratio P_{NC}/P_C, where P_{NC} is the permeability of the nanocomposite and P_C is the permeability of the pure polymer, quantitatively describes this reduction. We note that (i) at fixed filler concentration in the nanocomposites, the ratio P_{NC}/P_C is the same for all gases (i.e. filler addition does not change the gas selectivity); (ii) P_{NC}/P_C does not change with temperature. The measured P_{NC}/P_C values have been plotted for all test gases at the temperature of $T = 334\,\mathrm{K}$ in the insets of Figure 4.

The apparent activation energy for permeation E_P of the pure matrix are $(21 \pm 2)\,\mathrm{kJ/mol}$ for CO_2, $(35 \pm 1)\,\mathrm{kJ/mol}$ for H_2 and $(38 \pm 3)\,\mathrm{kJ/mol}$ for N_2, see section 5.2.1. In the nanocomposites, E_P does not change at all examined concentrations. The obtained average values are $(21 \pm 1)\,\mathrm{kJ/mol}$ for CO_2, $(32 \pm 3)\,\mathrm{kJ/mol}$ for H_2 and $(32 \pm 4)\,\mathrm{kJ/mol}$ for N_2.

Before going on with the discussion, it is worth to remark that the improvements of the membranes' gas barrier properties after filler addition are comparable to those detected in similar system such as graphite nanoplatelets (Kalaitzidou et al., 2007; Checchetto et al., 2014), graphene (Compton et al., 2010; Sadasivuni et al., 2013; Jin et al., 2013), functionalized graphene (Kim and Macosko, 2009), graphene oxide (Wu et al., 2013) or other high aspect ratio fillers such as silicate clays (Herrera-Alonso et al., 2010; Osman et al., 2004; Cui et al., 2015).

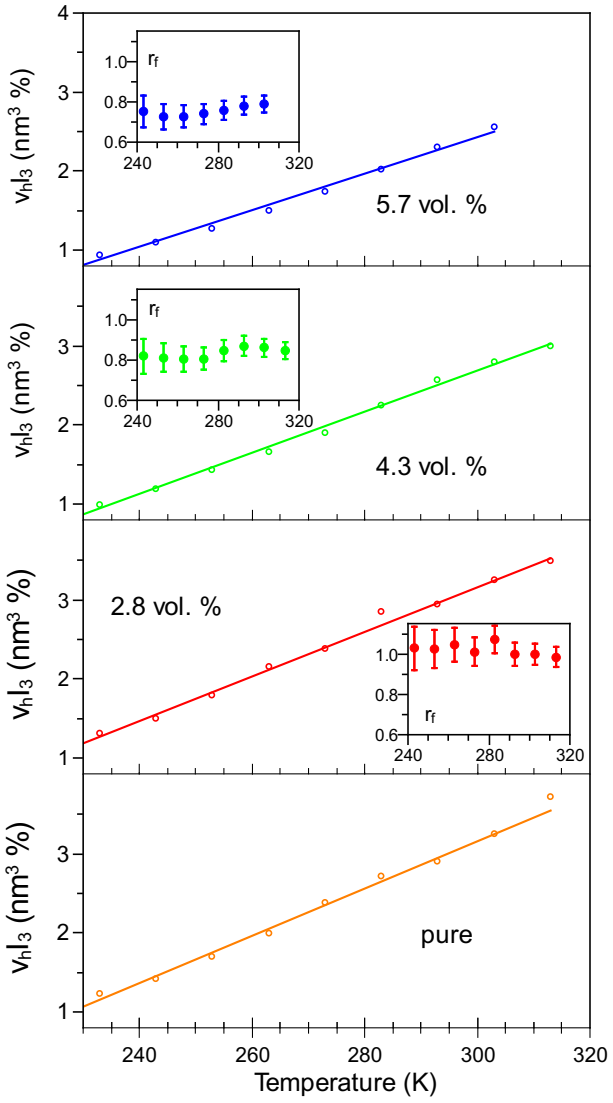

FIGURE 3. $v_{\mathrm{h}}I_3$ product for all samples as a function of temperature. The experimental errors are inside the size of the symbols. The straight lines are linear fits. The insets show the ratio r_f between the fractional free volume of the nanocomposites and of the pure epoxy matrix as a function of temperature.

6.4. Modeling of permeation in FLG-based nanocomposites

In this section, we will discuss the obtained experimental results in the framework of different models for permeation in PNCs. We will analyze the parameter $P_{\mathrm{NC}}/P_{\mathrm{C}}$ at the intermediate temperature of $T = 334\,\mathrm{K}$ in the different nanocomposites. As previously reported, the $P_{\mathrm{NC}}/P_{\mathrm{C}}$ value is temperature independent.

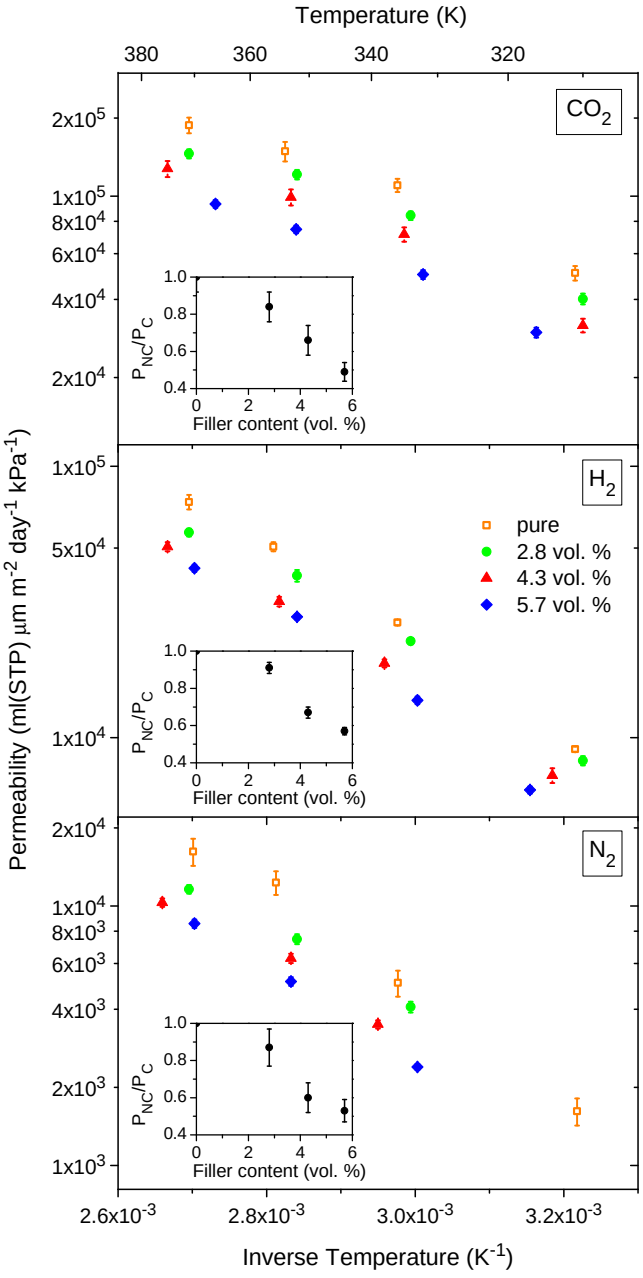

FIGURE 4. Arrhenius plots of the permeability of CO_2, H_2 and N_2 in the pure epoxy matrix and in the nanocomposite samples. The insets report, for each nanocomposite sample, the permeability reduction P_{NC}/P_C at $T = 334\,K$ as a function of the filler concentration.

In ideal nanocomposites, i.e. when the polymer matrix completely wets the fillers' surface and none of the defects introduced in chapter 1 appear, the nanocomposites' permeability P_{NC} can be predicted by using two simple models. The parameters in both models are the permeability P_{C} of the polymer matrix, the permeability P_{d} of the dispersed phase (i.e. of the fillers) and the filler volume fraction φ_{d}.

(1) The Nielsen (1967) model, developed for impermeable fillers as those used for this study, explains the reduction of the membranes' permeability by assuming that the permeating molecules travel, in the nanocomposite, a longer (more tortuous) path in order to migrate from one side of the membrane to the other, due to the presence of the impermeable nanofillers. The permeability of the nanocomposites is reduced by a geometrical factor τ_{T}, called tortuosity factor, with respect to the pure polymer matrix (Aroon et al., 2010). Platelets with thickness w and lateral size L produce a τ_{T} given by the relation $\tau_{\mathrm{T}} = (1 + \varphi_d L/2w)$ and a permeability reduction given by (Adame and Beall, 2009)

$$\frac{P_{\mathrm{NC}}}{P_{\mathrm{C}}} = \frac{1 - \varphi_{\mathrm{d}}}{\tau_{\mathrm{T}}} \tag{6.4.1}$$

(2) The second model is called "Maxwell model" [1]. The permeability $P_{\mathrm{NC}}/P_{\mathrm{C}}$ of the nanocomposite is given by (Moore and Koros, 2005):

$$\frac{P_{\mathrm{NC}}}{P_{\mathrm{C}}} = \frac{P_{\mathrm{d}} + 2P_{\mathrm{C}} - 2\varphi_{\mathrm{d}}(P_{\mathrm{C}} - P_{\mathrm{d}})}{P_{\mathrm{d}} + 2P_{\mathrm{C}} + \varphi_{\mathrm{d}}(P_{\mathrm{C}} - P_{\mathrm{d}})} \tag{6.4.2}$$

In the present impermeable fillers ($P_{\mathrm{d}} = 0$), $w = 10\,\mathrm{nm}$ and $L \simeq 10\,\mu\mathrm{m}$: we can use the above models to estimate the ratio between the nanocomposites' permeability and the permeability of the polymer matrix, as a function of the filler content φ_{d}. Figure 5 shows the measured $P_{\mathrm{NC}}/P_{\mathrm{C}}$ ratios (points) at different φ_{d} values and the $P_{\mathrm{NC}}/P_{\mathrm{C}}$ ratios (lines) as calculated by using Nielsen model (line a) and Maxwell's model (line b). The comparison between the experimental and calculated $P_{\mathrm{NC}}/P_{\mathrm{C}}$ ratios indicates that the Nielsen's model strongly overestimates the reduction of the nanocomposites, whereas Maxwell's model qualitatively describes an almost linear permeability decrease with increasing filler content, but underestimates the permeability reduction. These models assume an ideal morphology of the matrix-filler interface: to accurately describe the obtained experimental results, it is therefore worth considering the potential formation of defects.

Interface defects are connected to the formation of voids or of polymer chain rigidification at the interface between matrix and fillers. The nanocomposites in which such defects appear can be modeled as a system consisting of two phases:

(1) the pure, unmodified polymer matrix with permeability P_{C};

[1] The Maxwell model for the permeability of PNCs is based on an equation originally derived by Maxwell (1873) for the electrical conductivity of composites

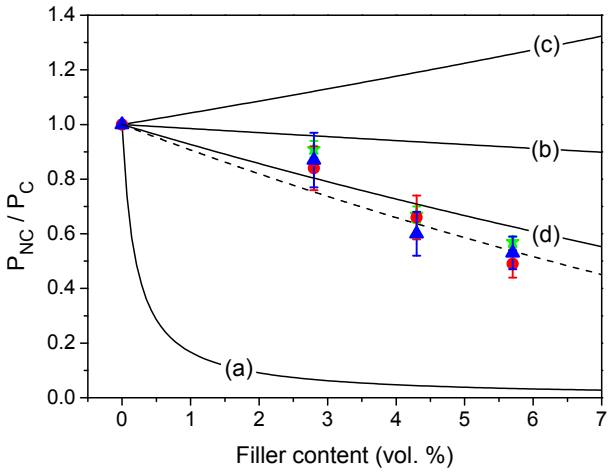

FIGURE 5. P_{NC}/P_C ratio as obtained from experimental measurements (symbols) and calculations with different models, as a function of the filler content φ_d. The experimental points represent the values for CO_2 (red circles), H_2 (green stars), N_2 (blue triangles). Line (a) represents Nielsen's model (equation (6.4.1)), line (b) Maxwell's equation in the case of ideal morphology (equation (6.4.2)). Line (c) is obtained using a modified Maxwell model assuming the presence of interface voids. Line (d) represents Maxwell model in the case of the presence of a pseudo-dispersed phase for the case of a rigidified polymer layer (equations (6.4.9) and (6.4.10)) with thickness $l_{if} = 20\,nm$ surrounding the fillers. A similar situation but with $l_{if} = 25\,nm$ is represented by the dashed line.

(2) a "pseudo-dispersed phase", formed by the fillers having permeability P_d surrounded by the modified polymer layers. The modified layers have permeability P_{if} and occupy a volume fraction φ_{if} in the PNC (the subscript "if" stands for "interface").

The effective permeability of this pseudo-dispersed phase is given by the following relation (Pal, 2008; Aroon et al., 2010; Moore and Koros, 2005; Rezakazemi et al., 2014):[2]

$$P_{ps} = P_{if}\frac{P_d + 2P_{if} - 2\varphi_s(P_{if} - P_d)}{P_d + 2P_{if} + \varphi_s(P_{if} - P_d)} \tag{6.4.3}$$

where $\varphi_s = \varphi_d/(\varphi_d + \varphi_{if})$ is the volume fraction of the filler particles in the pseudo-dispersed phase. For filler particles shaped as platelets with thickness w, if the

[2]Note that equation (6.4.3) is nothing but eq. 6.4.2 in which the continuous phase is replaced by the interface and the nanocomposite permeability is replaced by the permeability of the pseudo-dispersed phase.

interfacial region consists of layers with thickness l_{if} on both sides of the platelets, φ_{s} can be obtained by (Checchetto et al., 2014)

$$\varphi_{\mathrm{s}} = \frac{\varphi_{\mathrm{d}}}{\varphi_{\mathrm{d}} + \varphi_{\mathrm{if}}} = \frac{w}{w + 2l_{\mathrm{if}}} \tag{6.4.4}$$

Modeling the system as composed by a continuous phase in which particles with permeability P_{ps} and volume fraction $(\varphi_{\mathrm{d}} + \varphi_{\mathrm{if}})$ are dispersed, the ratio $P_{\mathrm{NC}}/P_{\mathrm{C}}$ can be evaluated by the following equation, which is a modified expression of eq. 6.4.2, in which the pseudo-dispersed phase replaces the dispersed phase:

$$\frac{P_{\mathrm{NC}}}{P_{\mathrm{C}}} = \frac{P_{\mathrm{ps}} + 2P_{\mathrm{C}} - 2(\varphi_{\mathrm{d}} + \varphi_{\mathrm{if}})(P_{\mathrm{C}} - P_{\mathrm{ps}})}{P_{\mathrm{ps}} + 2P_{\mathrm{C}} + (\varphi_{\mathrm{d}} + \varphi_{\mathrm{if}})(P_{\mathrm{C}} - P_{\mathrm{ps}})} \tag{6.4.5}$$

The above equation provides an estimate of the nanocomposite permeability reduction when the permeability P_{if} of the interface and its thickness l_{if} are known.

Let us first consider interfacial voids: their presence would increase the permeability of the nanocomposite. In fact, the permeability P_{if} of the voids can be estimated as the product between the solubility of vacuum $S_{\mathrm{vac}} = (RT)^{-1}$ and Knudsen diffusivity:

$$D_{\mathrm{K}} = \frac{1}{3} d_{\mathrm{pore}} \sqrt{\frac{8}{\pi} \frac{RT}{M}} \tag{6.4.6}$$

where d_{pore} is the size of the void and M is the molar weight of the diffusing molecule. This situation was simulated by assuming $P_{\mathrm{d}} = 0$, by choosing CO_2 as penetrant, $d_{\mathrm{pore}} = (6v_{\mathrm{h}}/\pi)^{1/3} = 0.7\,\mathrm{nm}$ and $l_{\mathrm{if}} = 3d_{\mathrm{pore}}$. The obtained $P_{\mathrm{NC}}/P_{\mathrm{C}}$ values are represented in Figure 5 by line (c). The figure shows that this behavior is incompatible with the experimental observations for the permeability of the nanocomposite, as its predicts an increase of permeability with increasing filler loading, in contrast with the observed decrease. Note also that the presence of interfacial voids can be excluded by the PALS analysis, which would evidence an increase of the *o*-Ps formation (and thus an increase of the I_3 annihilation signal), rather than its reduction as it was observed.

A formation of a rigidified polymer region with reduced free volume is, on the other hand, compatible with the observed I_3 reduction as well as with the observed reduction of the permeability (Kim et al., 2006; Mahajan and Koros, 2002).

The permeability P_{if} of the rigidified, interfacial polymer layer is reduced with respect to P_{C}. The reduction is quantitatively defined by the so-called "chain rigidification factor" $\beta = P_{\mathrm{C}}/P_{\mathrm{if}}$. The structural analysis described in section 3.2.2 shows that the FLG nanoplatelets in the PNCs have their surface aligned parallel to the membrane surfaces and do not aggregate. To apply eq. 6.4.5 to our experimental results, we will model the nanocomposite as in Figure 6, assuming that above and below every FLG platelet, a rigidified polymer region with thickness l_{if} and permeability P_{if} has formed. Nanoplatelets are separated by an average distance $2h$, measured along the direction of net mass flow, i.e. orthogonal to the FLG surface. The average distance between the nanoplatelets can be calculated

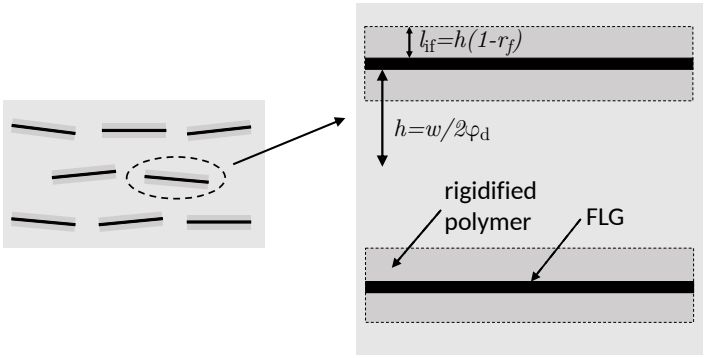

FIGURE 6. Graphical representation of the nanocomposite structure. The FLG platelets are represented as black rectangles and the light gray region is the unmodified polymeric matrix. The rigidified polymer layers are represented as dark gray rectangles of thickness l_{if} surrounding the nanoplatelets. The arrow of length h represents one half of the average distance between two FLG nanoplatelets.

knowing their thickness and their volume fraction. For $w = 10\,\text{nm}$, we obtain for h the following values: 178 nm for $\varphi_d = 2.8$ vol.%, 120 nm for $\varphi_d = 4.3$ vol.% and 88 nm for $\varphi_d = 5.7$ vol.%. A fraction of this region, that is a layer of thickness $l_{if} = (1-r_f)h$, consist of rigidified polymer chains. Therefore, for every region with volume $V = 2hL^2$ surrounding the filler, a sub-domain with volume $V_{if} = 2l_{if}L^2 = 2h(1-r_f)L^2$ consists of rigidified polymer whereas the remaining part, with volume $V - V_{if}$, consists of unmodified polymer. To evaluate l_{if}, we assumed that the free volume reduction due to the addition of fillers occurs only in these interface regions. Namely, we can show that a free volume loss uniformly distributed in the whole polymer matrix is not compatible with our experimental observations. To do so, we need to remember the relation between permeability and free volume:

$$P = A_P \exp\left(-\frac{B_P}{f}\right) \tag{6.4.7}$$

where A_P and B_P are empirical parameters depending on the size and shape of the penetrant molecule (Matteucci et al., 2006). A fractional free volume reduction of approx. 15-20%, as reported in Figure 3 (see insets), would reduce the permeability by approx. one order of magnitude, i.e. much more than experimentally observed. We will thus assume, to a first approximation, that the fractional free volume reduction is concentrated only around the fillers, where f vanishes, whereas the unmodified polymer matrix maintains the same f as the pure polymer. We used PALS data to obtain r_f and thus l_{if} using the following equation:

$$\frac{V - V_{if}}{V} = r_f = \frac{f_{NC}}{f_C} \tag{6.4.8}$$

The values of r_f in the different samples are reported in the insets of Figure 3. For the sample with 4.3 vol.% filler content, a value of $l_{\mathrm{if}} = (18 \pm 4)\,\mathrm{nm}$ was obtained, whereas for the 5.7 vol.% loaded sample, the thickness l_{if} is $(20 \pm 3)\,\mathrm{nm}$. For the nanocomposite with lowest filler content, i.e. 2.8 vol.%, the r_f values approach unity (inside their indetermination), so a meaningful value for l_{if} cannot be obtained.

Since we assumed total rigidification and complete free volume loss at the interface, it is reasonable to assume $\beta \simeq \infty$, which means that the interface is impermeable, $P_{\mathrm{if}} = 0$. If this is the case, $P_{\mathrm{ps}} = 0$ as well and we can simplify eq. 6.4.5:

$$\frac{P_{\mathrm{NC}}}{P_{\mathrm{C}}} = \frac{1 - (\varphi_{\mathrm{d}} + \varphi_{\mathrm{if}})}{1 + \frac{1}{2}(\varphi_{\mathrm{d}} + \varphi_{\mathrm{if}})} \tag{6.4.9}$$

The volume fraction φ_{if} of the interface can be calculated knowing l_{if} and we can write

$$\varphi_{\mathrm{d}} + \varphi_{\mathrm{if}} = \varphi_{\mathrm{d}} \left(1 + \frac{2l_{\mathrm{if}}}{w}\right) \tag{6.4.10}$$

The permeability reduction as predicted by the two above equations is represented by line (d) of Figure 5 in the case $l_{\mathrm{if}} = 20\,\mathrm{nm}$, as obtained from PALS data for the 5.7 vol.% loaded sample. Line (d) is in good agreement with the permeability data and shows that polymer rigidification at the matrix-filler interface explains the experimental observations. We also remark that the ratio $P_{\mathrm{NC}}/P_{\mathrm{C}}$ calculated in this way depends weakly on β: for example, choosing $\beta = 5$ would provide values differing by less than 10 % from those obtained with $\beta = \infty$. Similar observations were reported by other researchers (Li et al., 2005; Moore et al., 2004). A better agreement would be obtained by a higher value of l_{if}. The dashed line in Figure 5 shows the ratio $P_{\mathrm{NC}}/P_{\mathrm{C}}$ that would result by assuming $l_{\mathrm{if}} = 25\,\mathrm{nm}$, a slightly thicker interface region. The free volume reduction detected by PALS seems therefore to be underestimated. We argue that the rigidified regions contain free volume elements that, despite being probed by positrons, are not accessible by the diffusing molecules and thus do not contribute to their transport.

We can now compare the obtained values for the thickness of the rigidified polymer region with the ones found in literature for similar high aspect ratio fillers. Studied on the solvent uptake of ethylenevinyl acetate/montmorillonite nanocomposites explain the large decrease in solvent uptake after 5 wt. % filler addition with the formation of a rigidified polymer layer of at least 25 nm (Pramanik et al., 2004). Measurements carried out by Atomic Force Microscopy by Adame and Beall (2009) in polyamide/clay nanocomposites revealed rigidified regions with thicknesses of approximately 40-50 nm.

To conclude this discussion, we remember that the presence of the rigidified polymer region does not affect the T_{g} value as detected by PALS and DSC analysis. The glass transition temperature T_g detected by positrons, see Figure 1, does not change with filler content. PALS analysis is indeed based on *o*-Ps formation

and annihilation in the free volume elements, which do not form in the rigidified regions. A T_g variation is also not detectable by DSC (see section 3.2.2.3). Negligible or no T_g variations upon filler additions are reported in literature for many of nanocomposites where rigidification occurs, evidenced by mechanical or thermal effects: see, for example, (Bansal et al., 2005; Moll and Kumar, 2012; Harton et al., 2010; Rittigstein and Torkelson, 2006; Lu and Nutt, 2003; Ash et al., 2002; Holt et al., 2014, 2013; Starr et al., 2016). No clear explanation exists for this unexpected behavior. Indrakanti et al. (2004) and Moll and Kumar (2012) suggest that this behavior occurs when the interface layer is decoupled from the remaining part of the polymer and it does not relax in the timeframe of the DSC experiments. Therefore, the detected glass transition temperature is that of the unmodified polymer matrix.

6.5. Conclusions

This study evidences that the addition of high aspect ratio FLG fillers decreases the gas permeability of the epoxy membrane because it gives rise to the formation of rigidified polymer layers, which are gas-impermeable. The decrease in permeability can be explained by assuming the rigidification of the polymer layers at the matrix-filler interface. These rigidified regions are gas impermeable; their thickness has been estimated starting from PALS measurements and was found to be of $\sim 20\,\text{nm}$. This value is in good agreement with those found in literature for other polymer nanocomposite samples, although determined through different methods.

CHAPTER 7

Diffusion mechanism through cellulose nanofiber films

7.1. Introduction

The current packaging industry is based mostly on petroleum-derived polymers such as poly(vinyl alcohol) (PVA), polyvinyldiene chloride (PVdC) and polyethylene terephthalate (PET), given to their low cost, good processability and good barrier properties (Miller and Krochta, 1997; Syverud and Stenius, 2009). The extensive use of these polymers gives rise to serious environmental concerns due to their problematic disposal, their difficult recycling and the dependence on fossil resources for their production (Sorrentino et al., 2007; Siracusa et al., 2008; Jamshidian et al., 2010). The development of biodegradable and carbon-neutral packaging materials is therefore needed.

Cellulose nanofibers (CNs) are a biobased and biodegradable material with promising properties for applications in food packaging industry. They are rod-shaped cellulose crystals with width of few nm and length of several hundreds of nm. The high aspect ratio of the CNs and their ability to form inter- and intrafibrillar hydrogen bonds permit them to assemble in dense, highly packed films having good optical transparency and gas barrier properties. These barrier properties are also a consequence of the cellulose nanofibers' high crystallinity (Aulin et al., 2010). Studies carried out by Rodionova et al. (2011); Aulin et al. (2010) and Bayer et al. (2016) have demonstrated the excellent gas barrier properties of self-supporting cellulose nanofiber films with thickness of few µm: their oxygen permeability values are in fact competitive with those of common synthetic polymers used in the packaging industry, such as ethylene vinyl alcohol (EVOH) or poly (vinyl alcohol) (Pauly, 1999). Cellulose nanofiber films can also be deposited as coatings on different substrates using simple and inexpensive deposition techniques, such as dip-coating and spin-coating (Herrera et al., 2016). Several studies have been carried out on CN-coated polymers, and it was observed that the coatings decrease the gas transport rates by orders of magnitude with respect to those through the uncoated substrates (Fukuzumi et al., 2009; Lavoine et al., 2014; Aulin et al., 2013; Herrera et al., 2016). Highly transparent CN-based coatings with good barrier properties are thus attracting great interest in the food packaging technology to replace petroleum-based materials.

Research is examining the influence on the gas barrier properties of the cellulose nanofiber films of different factors, such as the specific penetrant molecule (Fukuzumi et al., 2013a) or the membrane temperature (Bayer et al., 2016). The effect of fibril entanglement, (Belbekhouche et al., 2011), functional groups on the fiber's surface (Fukuzumi et al., 2013a) and fiber length (Fukuzumi et al., 2013b) have also been studied.

In this work, we analyze the gas transport properties of bilayer membranes consisting of cellulose nanofiber films deposited on PLA (polylactic acid) foils. The aim of this study is to investigate in detail the processes governing gas transport through well characterized TEMPO-oxidized cellulose nanofiber (TOCN) films, to understand the mechanism behind the excellent gas barrier properties of these materials (see section 3.3 for information on TEMPO-mediated oxidation).

To this task, bilayer membrane samples were prepared by depositing TOCN films on PLA foils by a liquid casting technique. We also prepared nanocomposite coatings by dispersing TiO_2 nanoparticles in the TOCN films, in order to study the influence of the nanoparticles on the films' properties.

Polylactic acid is a transparent, bioderived and biodegradable polymer with potential applications in the food packaging technology (Jamshidian et al., 2010). Though it has good gas barrier properties (Jamshidian et al., 2010), its permeability is still higher than that of commercial polymers such as PET or PVdC (Hanika et al., 2003) and the improvement of its gas barrier performances could stimulate its use for food packaging.

TiO_2 (titania) is an inert, non-toxic, inexpensive material with applications in different fields thanks to its photocatalytic activity (Rhim et al., 2013; Fujishima et al., 2000). In the food packaging sector, the antimicrobial properties of TiO_2 nanoparticles make them suitable for applications as fillers in nanocomposite materials. Indeed, when irradiated with UV light, TiO_2 produces reactive oxygen species able to kill microorganisms (Rhim et al., 2013; He and Hwang, 2016). Moreover, it has been shown that TiO_2 nanoparticles dispersed in a biopolymer matrix can improve the mechanical properties of the material (Zhou et al., 2009).

We performed gas permeation experiments by using test gases with different molecular size and condensability and studied the permeation of such gases by systematically changing the membrane temperature and gas pressure. The data obtained from the permeation tests were interpreted based on the information on the void structure of the films, obtained by depth-profiled PALS analysis.

The sample preparation and characterization have been described in the *Materials* chapter of this thesis (see section 3.3) and will be only briefly recalled in the following. In this chapter, we will therefore focus on the results obtained by PALS and gas transport measurements and on their interpretation.

7.2. Free volume and gas transport properties: experimental results

7.2.1. Structural properties. Here, we recall the information obtained by the structural analysis of the samples, as presented in section 3.3, focusing on the aspects which are relevant to understand the gas transport mechanism through TOCN coatings. AFM microscopy shows that the cellulose nanofibers are rod-like crystals with width of approx. 4 nm and length between 50 nm and 300 nm. When deposited on a support, they form films with uniform thickness and morphology, as detected by SEM. SEM analysis also showed that, in the TOCN coatings, the cellulose nanofibers are aligned parallel to each other and with their main axis parallel to the membrane's surface. The absence of inhomogeneities in the TOCN films is also confirmed by their high optical transparency.

TOCN:TiO_2 coatings have structure analogous to that of TOCN coatings. TiO_2 nanoparticle agglomerates with size of the order of 100 nm have been detected by SEM and reduce the optical transparency of the films due to light scattering.

7.2.2. PALS analysis. Depth-profiled PALS measurements were carried out with pulsed low energy positron system (PLEPS) apparatus (Egger, 2010; Sperr et al., 2008) at the high intensity positron source NEPOMUC (NEutron induced POsitron source MUniCh) (Hugenschmidt, 2010; Hugenschmidt et al., 2008). e^+ are injected in the studied samples by a pulsed, variable energy positron beam. Depth-profiled analyses were obtained using positron implantation energies in the range 1-12 keV, corresponding to average implantation depths $\overline{x}$ between 27 and 1.4×10^3 nm, as obtained by the following equation (Mills and Wilson, 1982):

$$\overline{x}(\mathrm{nm}) = \frac{40}{\varrho} E^{1.6} \tag{7.2.1}$$

where ϱ is the cellulose density and in this case equals $1.57\,\mathrm{g\,cm^{-3}}$ (see section 3.3) and E is the positron implantation energy expressed in keV.

The overall time resolution of the apparatus (pulsing and detector) was 230-240 ps and the beam diameter was smaller than 1 mm at all energies. The acquired spectra, consisting of 4×10^6 events each, were analyzed with the software PATFIT-88 (Kirkegaard et al., 1989). All spectra were well fitted with three lifetime components: the shortest component $\tau_1 = 121$ ps had an intensity of $I_1 \simeq 10\%$, the second component $\tau_2 = 380$ ps had an intensity $I_2 \simeq 72\%$. The longest component τ_3 was attributed to *o*-Ps annihilation events in nano-sized voids.

In the following, we will neglect the short-lived lifetime components, τ_1 and τ_2, and we will only discuss the τ_3 parameter and its intensity I_3, which describe the *o*-Ps annihilation and give information, respectively, on the size of the voids and on their number density (Mallon, 2003; Consolati and Quasso, 2010). In Figure 1, τ_3 and I_3 are plotted as a function of the mean positron implantation depth. None of these quantities seem to depend on the implantation depth: τ_3 has a constant average value of (1.37 ± 0.02) ns and I_3 lies at $(17.70 \pm 0.03)\,\%$. The voids

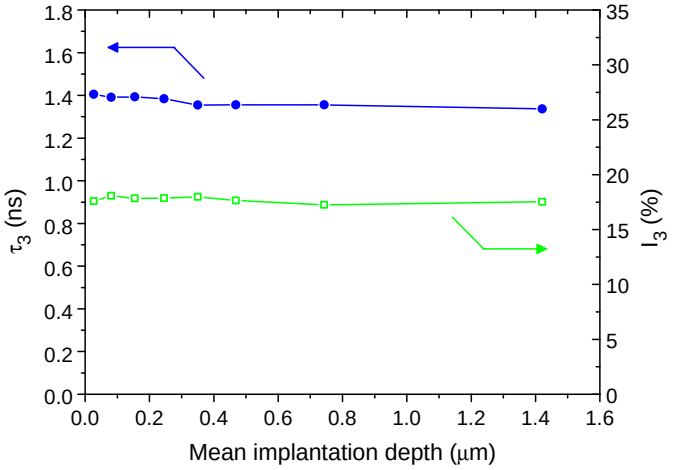

FIGURE 1. o-Ps lifetime τ_3 (full circles, left vertical axis) and intensity I_3 of the o-Ps annihilation signal (open squares, right vertical axis) as a function of the positron mean implantation depth.

are therefore uniformly distributed in the TOCN thickness with depth-independent size.

PALS spectra acquired at different temperatures in the range between 290 and 330 K, i.e. in the temperature range in which also gas transport was studied, showed no change in τ_3 nor I_3. As an example, the τ_3 and I_3 values are plotted as a function of temperature in Figure 2 for a positron energy of 4 keV, corresponding to an implantation depth of 234 nm.

7.2.3. Gas transport kinetics. The gas transport measurements were carried out with the technique and the apparatus described in section 4.1.2 using nitrogen, carbon dioxide, helium and deuterium as test gases. The measurements were carried out with the CP technique given the high signal to noise ratio of the detector (quadrupole mass spectrometer), which allowed us to detect very small gas fluxes through the TOCN membranes. D_2 was preferred over H_2 as a test gas to further increase the signal to noise ratio of the corresponding mass signal. Measurements were also carried out using air with relative humidity (RH) between 20% and 50%, as measured by a Delta Ohm HD2301 thermohygrometer, to detect the oxygen and water vapor signals. The critical temperature T_c and kinetic diameter σ_k of the studied gases are given in Table 1 of chapter 4. Measurements were performed at temperatures between 293 and 324 K on membrane samples shaped as disks with effective diameter (determined by the Viton O-rings in the sample holder) of 13 mm. Samples outgassing was performed before the permeation experiments by keeping them in high vacuum inside the experimental apparatus for at least 12 h.

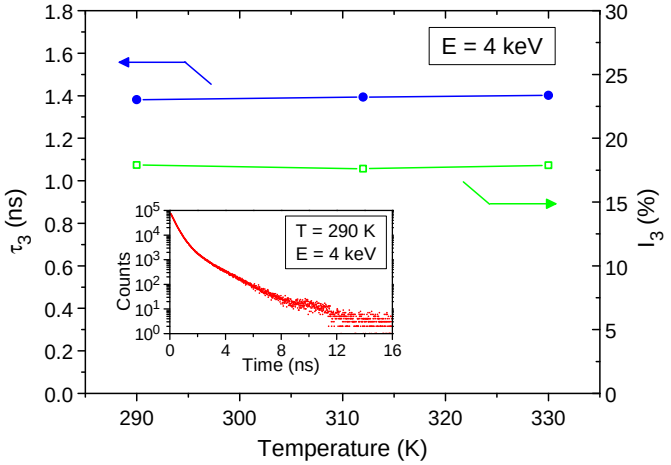

FIGURE 2. o-Ps lifetime τ_3 (full circles, left vertical axis) and intensity I_3 of the o-Ps annihilation signal (open squares, right vertical axis) as a function of temperature. The inset reports the positron annihilation spectrum acquired at $T = 290$ K and $E = 4$ keV.

Figure 3 shows the plots of the gas permeation flux $J(t)$ (we will call them permeation curves hereafter) of CO_2 and N_2 through an uncoated $(23 \pm 1)\,\mu m$ thick PLA membrane at temperature $T = (293 \pm 1)\,K$ and with upstream pressure $p_{HPS} = (35 \pm 1)\,kPa$. The inset shows the permeation curves for N_2 and O_2 when air at a RH of 37% is used as a test gas, at the same p_{HPS} and temperature. From the permeation curves, the gas transport parameters, i.e. the permeability P and the diffusivity D can be obtained as explained in section 4.1.2. P is obtained from the flux J^{stc} in stationary transport conditions (stc) by equation (4.1.8), whereas D can be obtained by fitting the permeation curves to equation (4.1.9); the obtained values, see Table 1, agree with those obtained by Komatsuka et al. (2008) and Bao et al. (2006), but the He permeability is somewhat smaller than that measured by Guinault et al. (2012). Due to the extremely fast transient of the gas transport of He in PLA, the diffusivity of this gas could not be measured. However, given a transient time shorter than 1 s, we can estimate a diffusivity $D \gtrsim 1 \times 10^{-6}\,cm^2\,s^{-1}$ (remembering $D = \ell^2/6\theta$, equation (2.1.18)).

We carried out permeation tests on TOCN/PLA and TOCN:TiO_2/PLA bilayer membranes with coating thicknesses ℓ from 2.6 µm to 6.6 µm. No permeation signal was detected through the TOCN-coated samples nor in the TOCN:TiO_2-coated samples when CO_2, N_2 or air at different RH values were used with p_{HPS} values up to ~ 100 kPa. The permeation flux for these gases was thus under the detection limit of the apparatus, of the order of $10^{-2}\,ml(STP)\,m^{-2}day^{-1}$. Assuming that the gas barrier properties of the bilayer membranes can be attributed only to the

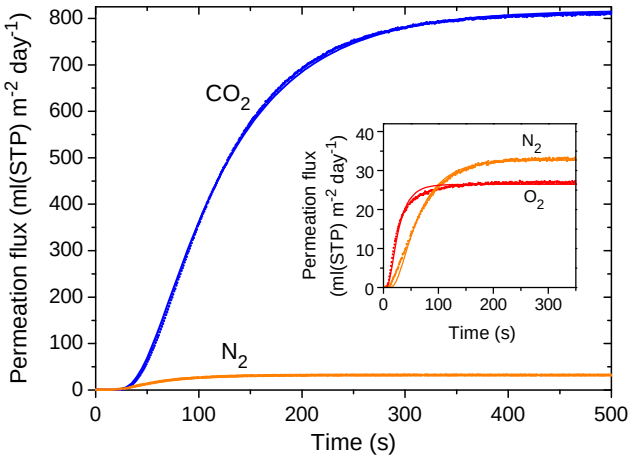

FIGURE 3. Permeation curves of CO_2 and N_2 for an uncoated PLA membrane of thickness $\ell_{\mathrm{PLA}} = (23 \pm 1)\,\mu\mathrm{m}$ at temperature $T = (293 \pm 1)\,\mathrm{K}$ and pressure $p_{\mathrm{HPS}} = (35 \pm 1)\,\mathrm{kPa}$. In the inset, the permeation curves for N_2 and O_2 are reported when air is used as a test gas, with the same membrane temperature and p_{HPS}. The lines represent the fits to equation (4.1.9).

Gas	Permeability $(\mathrm{ml(STP)}\,\mu\mathrm{m}\,\mathrm{m}^{-2}\,\mathrm{day}^{-1}\,\mathrm{kPa}^{-1})$	Diffusivity $(\mathrm{cm}^2\,\mathrm{s}^{-1})$
CO_2	$(5.2 \pm 0.2) \times 10^2$	$(6.5 \pm 0.6) \times 10^{-9}$
N_2	21 ± 1	$(1.29 \pm 0.09) \times 10^{-8}$
O_2	90 ± 5	$(2.8 \pm 0.2) \times 10^{-8}$
D_2	$(2.01 \pm 0.06) \times 10^3$	$(7 \pm 3) \times 10^{-7}$
He	$(2.6 \pm 0.1) \times 10^3$	-

TABLE 1. Permeability and diffusion coefficient of the analyzed test gases through a $(23 \pm 1)\,\mu\mathrm{m}$ thick PLA foil at temperature $T = (293 \pm 1)\,\mathrm{K}$ and pressure $p_{\mathrm{HPS}} = (35 \pm 1)\,\mathrm{kPa}$.

coatings, with thickness $\ell = 1\,\mu\mathrm{m}$ and using an upstream pressure $p_{\mathrm{HPS}} = 100\,\mathrm{kPa}$, this detection limit corresponds to a minimum detectable permeability $P_{\mathrm{min}} \simeq 10^{-4}\,\mathrm{ml(STP)}\,\mu\mathrm{m}\,\mathrm{m}^{-2}\,\mathrm{day}^{-1}\,\mathrm{kPa}^{-1}$ (see equation (4.1.8)).

To obtain a deeper understanding of the diffusion mechanism through the TOCN coatings, detailed permeation studies were carried out with D_2 and He by changing sample temperatures and HPS pressure. With these small-size gases, permeation fluxes were detected also through the nanocellulose-based coatings.

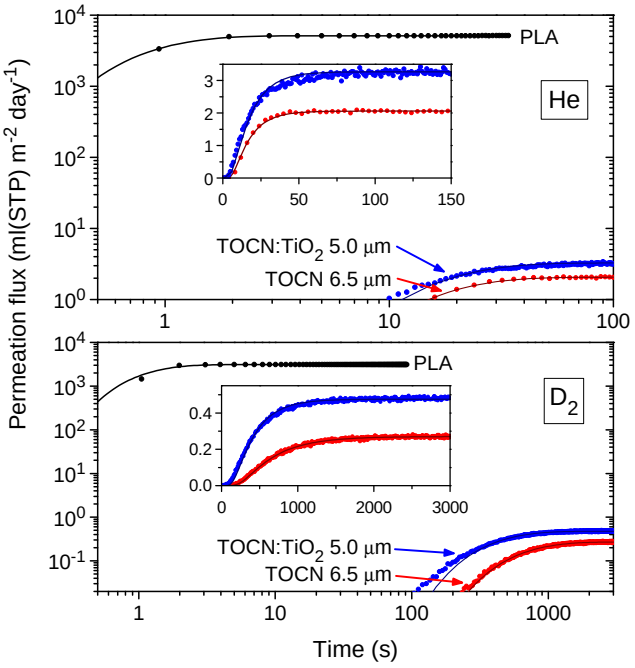

FIGURE 4. Permeation curves of He (upper panel) and D_2 (lower panel) through uncoated PLA (black symbols); TOCN/PLA (red symbols) and TOCN:TiO_2/PLA (blue symbols) membranes. The thickness of the coatings is indicated in the labels, the relative indetermination on the thickness is 5%. The same permeation curves in the TOCN/PLA and TOCN:TiO_2/PLA are also reported in the insets in linear scale. The lines represent the fits to equation (4.1.9). Measurements were performed at $T = (301 \pm 2)\,\mathrm{K}$ and $p_{\mathrm{HPS}} = (35 \pm 1)\,\mathrm{kPa}$.

The permeation curves of He and D_2 through uncoated PLA, TOCN/PLA and TOCN:TiO_2/PLA membranes at room temperature are reported in Figure 4. It can be observed that few µm thick TOCN or TOCN:TiO_2 coatings on the PLA foil reduce the permeation flux in stationary transport conditions by at least 3 orders of magnitude with these small-size gases.

In Figure 5 we show the D_2 permeation curves through TOCN/PLA bilayer membranes with different coating thickness ℓ_{TOCN} from 2.6 µm to 6.6 µm at fixed temperature $T = (301 \pm 2)\,\mathrm{K}$ and pressure $p_{\mathrm{HPS}} = (35 \pm 1)\,\mathrm{kPa}$. We can also observe that, increasing the coating thickness, the permeation flux at stc decreases and the transient times needed to set stc increase.

If we compare the permeation curves of He and D_2 in pure PLA and in the coated samples, we can observe that the coating decreases J^{stc} by orders of magnitude and increases the transient times by orders of magnitude. We can thus conclude

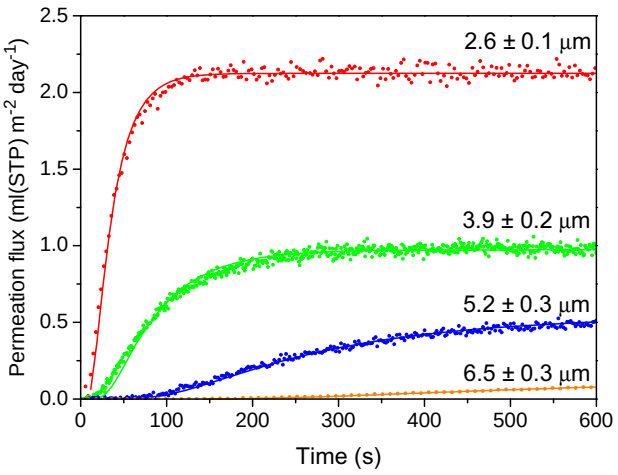

FIGURE 5. D_2 permeation curves through TOCN/PLA bilayer membranes with different TOCN coating thickness (indicated in the labels). The lines represent the fits to equation (4.1.9). Measurements were performed at $T = (301 \pm 2)\,\mathrm{K}$ and $p_{\mathrm{HPS}} = (35 \pm 1)\,\mathrm{kPa}$.

that the transport properties of the bilayer membranes are effectively determined by the coatings, whereas the PLA substrate merely acts as a permeable mechanical support. To analyze the gas transport process, the bilayer membranes can be thus described as membranes consisting only on nanocellulose-based films with thickness equal to that of the coating alone, thus neglecting the presence of the PLA support (Crank, 1979).

The measured permeability and diffusivity values for He and D_2 in the TOCN and TOCN:TiO_2 films at room temperature are reported in Table 2. The reported values are averages obtained on films with different thicknesses. The values in the table reveal that the TiO_2 nanoparticles only slightly affect the permeation properties of the TOCN coatings.

The flux J^{stc} in stationary transport conditions has been measured by changing the D_2 and He upstream pressure p_{HPS}. The obtained values are reported in Figure 6 for a TOCN/PLA membrane and show that J^{stc} is directly proportional to p_{HPS}, proving that the transport of these gases in TOCN layers occurs by the solution-diffusion mechanism, see equation (2.1.11) (Matteucci et al., 2006). A similar trend was also observed for the TOCN:TiO_2 films, meaning that the nanoparticle addition does not influence the gas transport mechanism.

Further information on the transport mechanism was obtained by carrying out permeation experiments at different temperatures. A set of experimental permeation curves through TOCN at temperatures between 295 K and 342 K is reported

	Permeability ($\mathrm{ml(STP)\,\mu m\,m^{-2}\,day^{-1}\,kPa^{-1}}$)	Diffusivity ($\mathrm{cm^2\,s^{-1}}$)
He, TOCN	0.4 ± 0.1	$(4.3 \pm 0.8) \times 10^{-9}$
He, TOCN:TiO_2	0.6 ± 0.1	$(5.6 \pm 0.5) \times 10^{-9}$
D_2, TOCN	0.10 ± 0.03	$(2.2 \pm 0.4) \times 10^{-10}$
D_2, TOCN:TiO_2	0.06 ± 0.02	$(8 \pm 2) \times 10^{-11}$

TABLE 2. Average permeability and diffusion coefficient of the analyzed test gases through TOCN and TOCN:TiO_2 membranes at temperature $T = (301 \pm 2)\,\mathrm{K}$ and pressure $p_{\mathrm{HPS}} = (35 \pm 1)\,\mathrm{kPa}$.

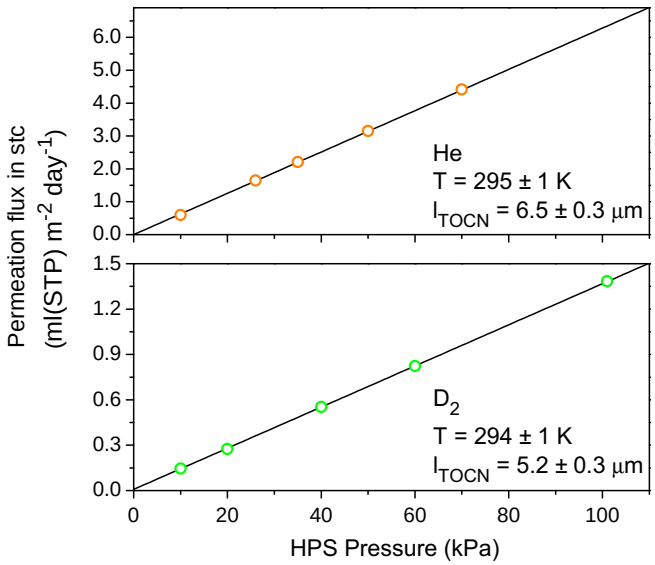

FIGURE 6. Permeation flux J^{stc} as a function of the upstream pressure of He (upper panel) and D_2 (lower panel). The straight lines are a guide for the eyes, the experimental errors are inside the size of the symbols.

in Figure 7. Increasing the temperature, the value of the gas flux J^{stc} increases and the transient times decrease. The addition of TiO_2 nanoparticles in the TOCN layers does not change this behavior. The Arrhenius plots of the P and D values for the two gases in the TOCN/PLA bilayer membranes are reported in Figure 8. Figure 9 shows corresponding data for D_2 permeation through the TOCN:TiO_2/PLA membranes. The P and D values obtained at different temperatures have been fitted to equations (2.1.29) and (2.1.26), respectively to find the apparent activation energies for permeation E_P and for diffusion E_D in the studied samples. The obtained values are reported in the figures. The pre-exponential factor D_0 for diffusion in TOCN was calculated as well and is $\sim 4 \times 10^{-3}\,\mathrm{cm^2\,s^{-1}}$ for He and

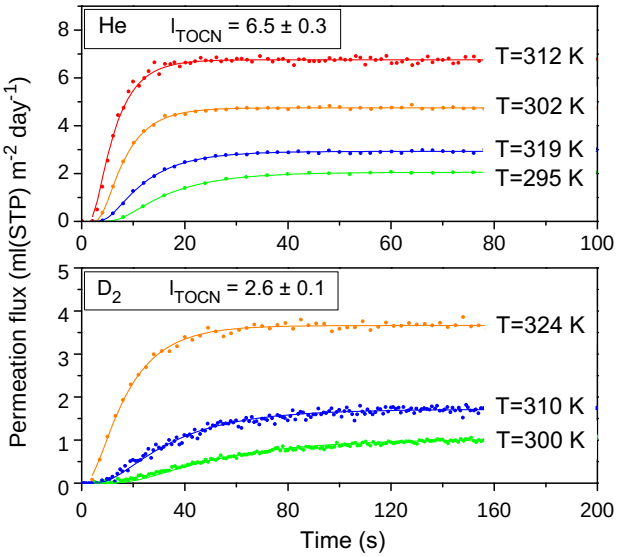

FIGURE 7. He (upper panel) and D_2 (lower panel) permeation curves through TOCN/PLA membranes obtained at different temperatures T and at $p_{\mathrm{HPS}} = (35 \pm 1)\,\mathrm{kPa}$.

$\sim 1 \times 10^{-3}\,\mathrm{cm^2\,s^{-1}}$ for D_2. For the sake of comparison, we note that in glassy polymers such as, for example, polyimides, the apparent activation energy E_D for small penetrants like H_2 lies in the range of 5 to 20 $\mathrm{kJ\,mol^{-1}}$ (Yampolskii et al., 1998), i.e. approximately a factor 2 smaller than the values detected for the TOCN films.

The solubility of the TOCN films was evaluated by the usual relation $P = SD$. The TOCN solubility values are approximately $1 \times 10^{-3}\,\mathrm{ml(STP)\,cm^{-3}\,atm^{-1}}$ for He and $5 \times 10^{-3}\,\mathrm{ml(STP)\,cm^{-3}\,atm^{-1}}$ for D_2. As often observed in size-sieving polymers, the solubility's temperature dependence is weak (Matteucci et al., 2006). Note that, in these units, for a perfect gas at standard temperature and pressure the solubility of vacuum is $S_{\mathrm{vac}} = \frac{n}{PV} = \frac{1}{RT} = 1\,\mathrm{ml(STP)\,cm^{-3}\,atm^{-1}}$, i.e. a factor 10^3 larger than in the studied samples.

7.3. Thermally activated diffusion mechanism in nanocellulose films

In this section, we will discuss the obtained results based on a comparison with other results reported in literature. We will then give an interpretation of the reported results, to describe the mechanism controlling the diffusion of small gases in TOCN films. Let us first consider the pure TOCN films.

Experimental results show that permeability of TOCN to He and D_2 is orders of magnitude lower than that of most commercial polymers (Matteucci et al., 2006). The D_2 permeability values obtained in this study are 2 orders of magnitude lower than those obtained by Bayer et al. (2016) in nanocellulose membranes prepared by

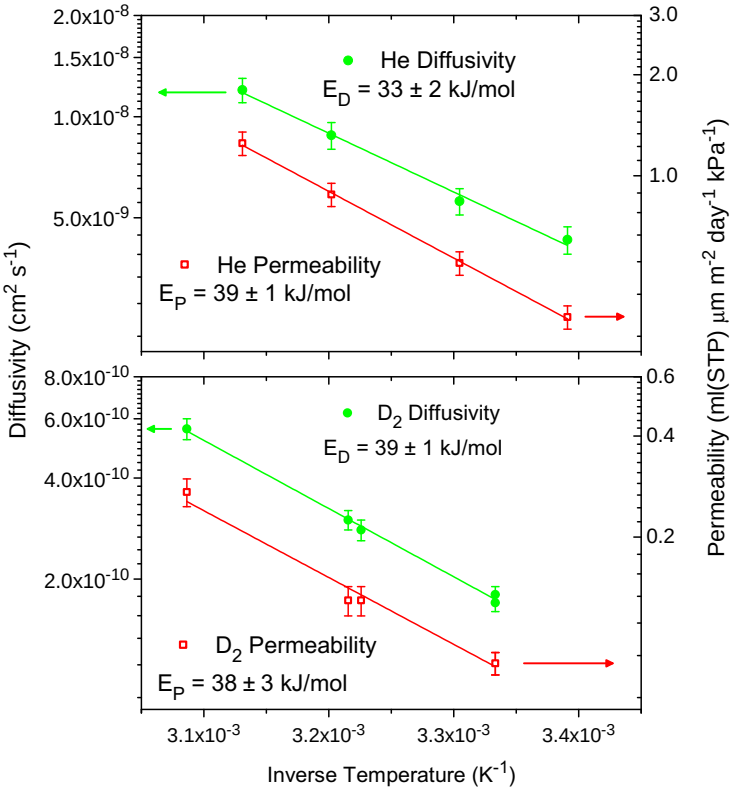

FIGURE 8. Arrhenius plot of the transport parameters of He (upper panel) and D_2 (lower panel) in TOCN films. Diffusivity values are reported as solid circles on the left vertical axis, permeability values are reported as open squares on the right vertical axis.

hydrochloric or sulfuric acid hydrolysis and are comparable to the values obtained by Fukuzumi et al. (2013a) on films obtained by TEMPO-mediated oxidation of cellulose fibers. In the same paper, Fukuzumi et al. (2013a) also measured the permeability of CO_2, O_2 and N_2 obtaining values slightly larger than those reported in this work. We attribute this effect to the different packing of the cellulose nanofibers due to peculiarities in their preparation. Indeed, it is known that the drying process of the CNs influences their packing and that the fibril coalescence reduce the swelling properties (Müller et al., 2014; Klemm et al., 2011; Ul-Islam et al., 2013). A review on the coalescence of cellulose fibers lists all the reactions that might occur during drying (Pönni et al., 2012). The process of coalescence between different fibers is still not completely understood and several reactions contribute to it (such as lactone bridge formation and crosslinking between adjacent nanocrystals). The main difference between the preparation of our TOCN and that described in other works is that we thoroughly wash the oxidized fibers with water to neutralize the pH instead of adding HCl. As a consequence, in our solution a

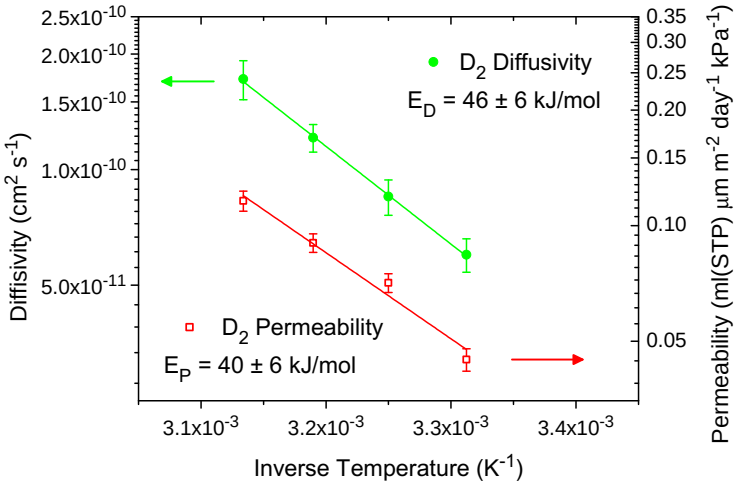

FIGURE 9. Arrhenius plot of the transport parameters of D_2 in TOCN:TiO_2 films. Diffusivity values are reported as solid circles on the left vertical axis, permeability values are reported as open squares on the right vertical axis.

reduced presence of ions between the polysaccharide chains can be expected, and therefore a reduced shielding of the charges borne by the nanofibers which results in enhanced fiber coalescence. Furthermore, the formation of salt nanocrystals during the films' drying is avoided. These conditions may favor the planar and parallel arrangement of the fibrils, which result therefore highly packed and form dense films with excellent gas barrier properties.

Starting from the separate evaluation of D and S, it is possible to infer that the low permeability of the TOCN films is due to the low diffusivity of gases through them. This can be shown by comparing the gas transport parameters of the nanocellulose-based coatings with those of common commercial polymers used for gas barrier applications. The D_2 solubility in the TOCN films is close to that of PET, PVA or PS (polystyrene), i.e. of the order of $10^{-2}\,\mathrm{ml(STP)\,cm^{-3}\,atm^{-1}}$ (Matteucci et al., 2006; Paterson et al., 1999). Diffusivity, on the other hand, is orders of magnitude lower than in PET or Teflon, which have H_2 diffusion constants of $\sim 10^{-7}\,\mathrm{cm^2\,s^{-1}}$ and $\sim 10^{-5}\,\mathrm{cm^2\,s^{-1}}$, respectively. The higher diffusivity of H_2 in these polymers is explained by their free volume structure: the cavities in these semi crystalline polymers have larger average size and thermally redistribute in their amorphous fraction (Zekriardehani et al., 2017; Olson et al., 2003; Madani et al., 1996; Rudel et al., 2008).

The TOCN films consist of a highly packed assembly of aligned cellulose nanorods with diameter of 4 nm and length between 50 and 300 nm, as shown in

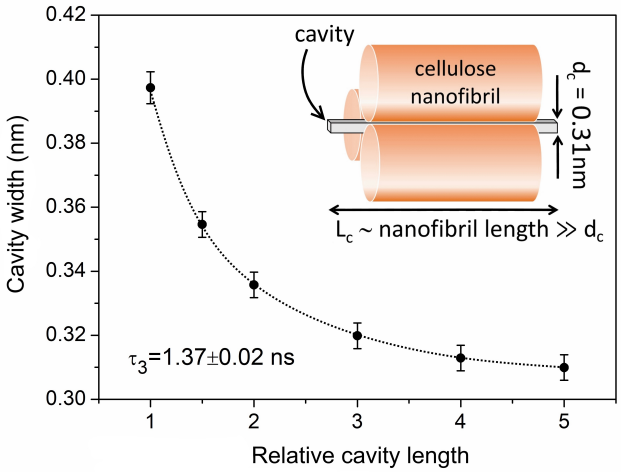

FIGURE 10. Relation between the cavity width d_c and the relative cavity length $m = L_c/d_c$ for fixed *o*-Ps annihilation lifetime $\tau_3 = (1.37 \pm 0.02)$ ns, as measured by PALS analysis. The dotted line is a guide for the eyes. In the inset, a graphical representation of the structure of the interfibrillar cavities.

Figures 18 and 21 of section 3.3, having crystalline structure (Dufresne, 2013; Lavoine et al., 2012). Due to the impermeable nature of the nanocrystals (Lavoine et al., 2012), the penetrant molecules are contained and migrate through empty regions between these nanofibers. Given the nanofiber geometry and their packing, we may assume that these cavities have the shape of channels with cross sectional size d_c and length $L_c = m d_c$ with $m \gg 1$, see Figure 10. As a first approximation, we assume that these channels are shaped as prisms with square cross section. Assuming such a geometry, d_c can be estimated from the *o*-Ps annihilation lifetime by the following relation:

$$\tau_3^{-1} = \lambda_0 \left[1 - \left(\frac{d_c}{d_c + 2\Delta R} + \frac{1}{\pi} \sin \frac{\pi d_c}{d_c + 2\Delta R} \right)^2 \times \left(\frac{m d_c}{m d_c + 2\Delta R} + \frac{1}{\pi} \sin \frac{\pi m d_c}{m d_c + 2\Delta R} \right) \right] \quad (7.3.1)$$

where $\lambda_0 \simeq 0.5\,\mathrm{ns}^{-1}$ is the *o*-Ps annihilation rate in the bulk state and $\Delta R = 0.166$ nm is the empirical electron layer thickness (Jasiska et al., 1996). Values for the width d_c are reported in Figure 10 for different values of the relative cavity length as described by the parameter $m = L_c/d_c$. These values were calculated with $\tau_3 = (1.37 \pm 0.02)$ ns. From the figure, it can be noted that for $m \gtrsim 5$, d_c reaches a constant value of $d_c = 0.31$ nm. In the case of the studied TOCN films, this condition is fully satisfied because the length of the cavity is comparable to that of the fibers, i.e. of the order of 100 nm. The previous discussion indicates

that the migration path for the diffusing molecules is formed by interconnected elongated cavities with a cross section of 0.31 nm. This geometry suggests that the selective transport properties of the TOCN films can be attributed to a size-sieving effect. Indeed, the size of the cavities is similar to that of He and D_2 but smaller than that of the other studied molecules (CO_2, N_2 and O_2).

Let us now consider the mechanism controlling the transport of He and D_2. When the cavity size d_c is comparable to the kinetic diameter σ_k of the diffusing molecules, diffusion can occur through two mechanisms, depending on the ratio σ_k/d_c (Xiao and Wei, 1992; Burganos, 2010; Gavalas, 2006).

Knudsen diffusion occurs when $\sigma_k/d_c < 0.5$. Penetrant molecules are in the gas phase and move with the thermal velocity given by $u = \sqrt{\frac{8k_BT}{\pi M}}$, where M is the molecular weight of the penetrant. The size of the cavity provides a measure of the diffusional length and the diffusion coefficient is given by $D_K = \frac{1}{3}ud_c$. In this regime, diffusion is not a thermally activated process and the diffusion coefficient depends weakly on temperature, only through the thermal velocity u, so that $D_K \propto \sqrt{T}$.

When $\sigma_k/d_c > 0.8$, diffusion occurs in configurational regime and penetrant diffusion in such cavities resembles surface diffusion. In this model, the penetrant interacts with the cavity walls and loses its gaseous state. It resides in a periodic potential at thermal equilibrium with the host matrix (Xiao and Wei, 1992; Burganos, 2010; Gavalas, 2006). If the potential is strongly corrugated with respect to k_BT, the particles vibrate with frequency ν within the bound state. Diffusion occurs through successive jumps between these bound states and is thermally activated, because a diffusive jump can occur only if the particle has an energy large enough to overcome a potential barrier E_D. For configurational diffusion, the diffusivity is given by the following expression:

$$D_{conf} = \frac{1}{z}\nu l_s^2 \exp\left(\frac{-E_D}{k_BT}\right) \tag{7.3.2}$$

where $1/z$ is the probability that the diffusing molecule jumps into one of the z available adjacent sites and l_s is the average distance between these sites (Xiao and Wei, 1992; Burganos, 2010; Gavalas, 2006).

Our experimental observations reveal that diffusion of small penetrants in TOCN films occurs in configurational regime because: (i) $\sigma_k/d_c > 0.8$ for He and D_2 and (ii) transport has thermally activated character. To compare the experimentally obtained pre-exponential factor ($D_0 \sim 4 \times 10^{-3}\,cm^2\,s^{-1}$) with the values suggested by the model, i.e. $D_0 = \frac{1}{z}\nu l_s^2$, we can take $\nu \sim 10^{12}\,s^{-1}$ and $z = 2$ (Barrer, 1978), which corresponds to assuming that, in these cavities, a molecule can only jump in sites at its right or at its left and that the penetrant concentration in the films is low enough to ensure that single-file diffusion is not set. In these conditions, the distance between the sites results $l_s \sim 1\,nm$, that is $d_c < l_s \ll L_c$.

We note that the obtained value for l_s well compares with the average distance between the carboxyl groups (-COOH) on the surface of the CNs, $\sim 2\,\mathrm{nm}$. Indeed, there is a carboxyl group every 2.5 cellobioses and the distance between neighboring cellobioses is approximately 1 nm (Jacobson et al., 1961). We therefore suggest that the measured activation energy is connected to sterical effects in the penetrant jumps between the diffusion sites rather than on sorption energies.

Let us now consider how the addition of TiO_2 nanoparticles influences gas transport in the TOCN-based membranes. The gas barrier properties of the TOCN films are not be affected by the addition of TiO_2 nanoparticles. The dependence of the gas flux J^{stc} on the gas pressure p_{HPS} is linear in both films and the apparent activation energy for permeation E_P in TOCN:TiO_2 films is compatible to that in pure TOCN films, inside the experimental error. No difference exists also in the apparent activation energy for diffusion E_D, clearly indicating that the mechanism governing gas transport in the TiO_2-filled samples is not influenced by nanoparticle dispersion. The most evident effect is the fact that the absolute value of the D_2 diffusion coefficient in the TOCN:TiO_2 samples is reduced by about a factor 3. The simplest way to explain this temperature-independent effect is as follows: TiO_2 nanoparticles are D_2-impermeable and their presence thus increases the tortuosity of the penetrant migration path. This increased tortuosity decreases the penetrant diffusivity according to the relation $D' = D/\tau_{\mathrm{T}}$. The fact that He does not show this behavior suggests that TiO_2 agglomerates allow selective He transport. However, further investigation would be needed to clear this point.

7.4. Conclusions

The experimental results on the gas transport properties of the nanocellulose-based films evidence their excellent barrier properties when exposing the membrane to ambient air, which make them well suited for applications in the field of food packaging (Parry, 1993) and showing good potential for OLED (Burrows et al., 2001) technology.

The diffusive paths consist of elongated nanocavities between the tightly packed nanofibers. The cross sectional size of these nanochannels has been evaluated by PALS and resulted of approx. 0.31 nm, suggesting that the selective transport of small penetrants is due to size-sieving effects. Molecule diffusion in the nanocellulose-based films is thermally activated and occurs in configurational regime. The dispersion of TiO_2 nanoparticles in the films does not alter the mechanism governing gas transport, despite a limited reduction in the gas diffusion coefficient, which can be attributed to tortuosity effects.

Conclusions

In this thesis we have studied the gas transport properties of membrane materials having different structural properties by gas phase permeation technique. The gas transport results were analyzed using information obtained by different characterization techniques to analyse the chemical properties (FTIR, DSC), structure (XRD), morphology (SEM, AFM) and free volume (PALS) of the membrane. Results indicate that the gas transport properties are controlled by free volume structure of the materials which limit, in fact, the penetrant diffusivity both in the dense, microporous and nanocomposite samples. The apparent Arrhenius behavior of the gas diffusivity in the dense amine- modified epoxy resins is due to the temperature dependent fractional free volume whose value increases linearly with temperature. The addition of FLG nanofillers produces gas-impermeable layers at the interface between matrix and filler where molecular transport is impeded by the local free volume reduction. In the microporous cellulose- based membranes, the free volume is formed by interconnected cavities having cross-sectional size comparable to the dimension of the penetrant molecules: in this confined geometry, the size- dependent molecular transport is consequence of sieving effects and diffusion occurs in configurational regime conditions.

Future perspectives of this research activity have their most interesting playground in the development of innovative cellulose-based materials. In fact, changing the process parameters for the film/coating preparation or adding different kinds of nanoadditives, samples with tuned packing properties of the NC fibers can be prepared to be tested as innovative green materials-based membranes for gas separation/purification applications or in advanced packaging applications such as in OLED technology.

List of Publications

Patil, P. N., Roilo, D., Brusa, R. S., Miotello, A., and Checchetto, R. (2015). Influence of nano-level molecular packing on the gas transport properties in amine-modified epoxy resins. *Polymer*, 58:130–138.

Patil, P. N., Roilo, D., Brusa, R. S., Miotello, A., Aghion, S., Ferragut, R., and Checchetto, R. (2016). Free volumes and gas transport in polymers: amine-modified epoxy resins as a case study. *Phys. Chem. Chem. Phys.*, 18(5):3817–3824.

Bounos, G., Andrikopoulos, K. S., Moschopoulou, H., Lainioti, G. C., Roilo, D., Checchetto, R., Ioannides, T., Kallitsis, J. K., and Voyiatzis, G. A. (2017). Enhancing water vapor permeability in mixed matrix polypropylene membranes through carbon nanotubes dispersion. *Journal of Membrane Science*, 524:576–584.

Roilo, D., Patil, P. N., Brusa, R. S., Miotello, A., and Checchetto, R. (2017). Nanovoids in epoxy resins: Role in the transport of light gases. *Polymer*, 113:147–155.

Roilo, D., Patil, P. N., Brusa, R. S., Miotello, A., Aghion, S., Ferragut, R., and Checchetto, R. (2017). Polymer rigidification in graphene based nanocomposites: Gas barrier effects and free volume reduction. *Polymer*, 121:17–25.

Roilo, D., Maestri, C. A., Scarpa, M., Bettotti, P., Egger, W., Koschine, T., Brusa, R. S., and Checchetto, R. (2017). Cellulose Nanofibrils Films: Molecular Diffusion through Elongated Sub-Nano Cavities. *The Journal of Physical Chemistry C*, 121(28):15437–15447.

Roilo, D., Maestri, C. A., Scarpa, M., Bettotti, P., and Checchetto, R. (2017). Gas barrier and optical properties of cellulose nanofiber coatings with dispersed TiO_2 nanoparticles. *Surface and Coatings Technology*, Accepted online October 2017, doi:10.1016/j.surfcoat.2017.10.015

Acknowledgments

First and foremost, I need to express my gratitude to my supervisor, Riccardo Checchetto, for his guidance, patience and encouragements throughout my whole PhD. After three years, I still feel I could learn so much from his endless curiosity and will to go deep in the understanding of the physics we were observing, never accepting shortcuts or easy replies to difficult questions.

Roberto S. Brusa acted has been a second supervisor, never refusing to provide me with help or suggestions. I am extremely thankful to him as well for his contagious, authentic enthusiasm for physics and for research in general.

I am grateful also to Antonio Miotello, the head of the IdEA laboratory in which I did my PhD. He always showed great interest in our work and his questions, comments and suggestions were always extremely accurate and precious.

Pushkar N. Patil accompanied me in my first steps as a researcher. I am grateful to him for all the time he spent in teaching me how research works, starting from the earliest stages of my activity, years ago.

A sincere and huge thank you goes to all the technical staff of the IdEA lab and of other Research Groups of the Department of Physics of the University of Trento. Nicola Bazzanella spent hours and hours in helping me, not only by providing me each time with the best SEM micrographs one could expect, but also by assisting me every time I had a technical or scientific question to ask. My sincere gratitude goes also to Claudio Cestari, who never let me wait more than half an hour when I needed his expertise to operate, modify or improve the experimental apparatuses of our lab. His ability to build in no time the right tool to solve every problem is simply stunning. Marco Bettonte, as well, never refused giving me the best advice and lots of his time to help me solving the most diverse difficulties in the experimental part of my work. Thank you also to Luigino Vivaldi, for his precious support related with the electronics of the instruments.

I also need to mention my collaborators in the Department of Physics. In particular, Marina Scarpa and Paolo Bettotti made me always feel comfortable in asking them for any help, might or might not be related to the scientific collaboration we carried out. I am thankful to my colleague, the Ph.D. student Cecilia A. Maestri for her tireless work and for providing me with samples and analyses with surprising speed, every time I needed them.

APPENDIX A

Water vapor and gas transport in nanocomposite polypropylene-carbon nanotube membranes

A.1. Introduction

In this appendix, we present a study on the water vapor and gas transport properties of nanocomposite membranes consisting of a isotactic polypropylene (iPP) matrix with dispersed multiwalled carbon nanotubes (MWCNTs). We used pristine MWCNT as well as PP-grafted nanotubes (polypropilene-grafted, MWCNT-g-PP) and prepared membranes with different filler concentration: the influence of filler agglomeration on the gas and water vapor transport properties of the membranes was also considered.

Carbon nanotubes (CNTs) are cylinders whose walls are made of one or more graphene layers (respectively called single-walled carbon nanotubes, SWCNT or multiwalled carbon nanotubes MWCNT). Typical diameters are in the range of 0.8 to 2 nm for SWCNT and 5 to 20 nm for MWCNT (but can be higher in some cases); their length ranges from less than 100 nm to some cm (De Volder et al., 2013). CNTs exhibit interesting properties such as chemical inertness, mechanical strength and thermal stability, which suggest the use of these fillers for the preparation of polymer nanocomposites (Sahoo et al., 2010; Coleman et al., 2006).

Polymer-CNT nanocomposites have recently been suggested as mixed matrix membranes for molecular separation (Dong et al., 2013; Ismail et al., 2009): these nanofillers are suggested to promote the formation in the nanocomposite of nanochannels for the selective transport of penetrant molecules. One of the main problems in the preparation of CNT-based polymer nanocomposites is the formation of CNT agglomerates in the polymer matrix (Sahoo et al., 2010). We have prepared nanocomposites with surface PP grafting to improve their compatibility with the matrix and thus favor their dispersion (Sanip et al., 2011).

Polypropylene (PP) is a commercial semi crystalline polymer widely used for different applications, including packaging and textiles. Different studies present in the scientific literature evidence that surface grafting of the nanotubes improves CNT dispersion also in the PP matrix (Zhou et al., 2006; Lee et al., 2007).

This work was carried out in collaboration with colleagues of the Institute of Chemical Engineering Sciences, Foundation for Research and Technology-Hellas, (Patras, Greece) and the departments of Chemistry and Chemical Engineering of

the University of Patras (Greece). The contribution of these colleagues was related to sample preparation and structural characterization as well as the measurement of water vapor transport. In this chapter, we will therefore focus on our contribution, i.e. the study of the gas transport properties of the membranes, while only an overview on the preparation and characterization of the nanocomposite samples will be given. A more detailed description can be found (Bounos et al., 2017) and references therein.

A.2. Sample preparation and characterization

A.2.1. Nanocomposite membranes preparation. The isotactic polypropylene used for the membrane preparation was purchased from Ega-Chemie (Steinheim, Germany). MWCNTs were supplied by Nanothinx (Patras, Greece) and have diameter of 15-35 nm. Details on the preparation of the MWCNT-g-PP are reported elsewhere (Yang et al., 2007, 2008). The nanocomposite membranes containing pristine or functionalized MWCNT as fillers were prepared by melt mixing the MWCNTs with iPP using a homemade batch mixer. We will call MWCNT/iPP and MWCNT-g-PP/iPP the nanocomposite membranes with dispersed pristine MWCNT and PP-grafted MWCNT, respectively.

A.2.2. SEM analysis. Figure 1 (a) and (b) show the cross section of MWCNT/iPP and MWCNT-g-PP/iPP membranes, respectively. In the membranes prepared with grafted nanotubes, a limited number of agglomerates is found. Similar observations are reported in literature (Lee et al., 2007; Prashantha et al., 2008). The SEM micrograph in Figure 1 (c) shows a MWCNT agglomerate at higher magnification. An evident nanotube pull-out can be observed, indicating the low adhesion between the pristine MWCNT and the iPP matrix. The nanotube pull-out is less prominent in the case of the functionalized particles shown in Figure 1 (d). To summarize, SEM analysis confirms that the functionalization of the nanotubes enhances their compatibility with the iPP matrix and their dispersion, resulting in a smaller tendency to form aggregates. Observation of the samples by optical microscopy (not reported here, see (Bounos et al., 2017) for details), confirms these results.

A.2.3. DSC analysis and crystallization kinetics. DSC analysis was carried out on iPP and on the nanocomposite samples. The degree of crystallinity X_c of the nanocomposites was calculated from the melting thermographs using the following relation:

$$X_c = \frac{\Delta H_f}{(1-\varphi_w)\Delta H_0} \tag{A.2.1}$$

where ΔH_f is the heat of fusion of the measured sample, ΔH_0 is the heat of fusion for a completely crystalline sample and φ_w is the CNT weight fraction in the nanocomposites. ΔH_0 was chosen equal to $209\,\mathrm{J\,g^{-1}}$ (Brandrup et al., 1989). The

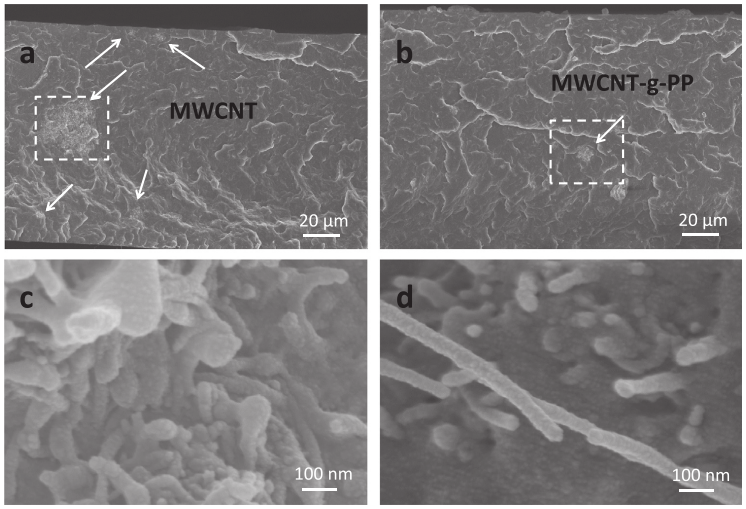

FIGURE 1. SEM images of the cross sections of MWCNT/iPP (a) and MWCNT-g-PP/iPP (b) membranes fractured in liquid nitrogen. The filler loading is 0.5 wt. % in both samples. Images (c) and (d) show the regions in the dashed squares in images (a) and (b), respectively, at higher magnification. Reproduced from (Bounos et al., 2017) with permission from Elsevier.

values obtained for MWCNT/iPP and MWCNT-g-PP/iPP nanocomposites with different filler loadings are reported in Figure 2. Insignificant variations of X_c with changing filler loadings are observed below a critical concentration of 2 wt. % for MWCNT/iPP and 4 wt. % for MWCNT-g-PP/iPP (note that, in the figure, the point corresponding to MWCNT/iPP and MWCNT-g-PP/iPP at 2 wt. % loading overlap). At higher concentrations, the degree of crystallinity is reduced.

A.2.4. Water vapor and gas transport measurements. To measure the Water Vapor Transmission Rate (WVTR) of the films, the "wet cup" method described by the standard ASTM E 96-95 (ASTM International, 2010) has been used. The WVTR is defined as the ratio between the water vapor stream j^{stc} at regime and the membrane surface area A: $\mathrm{WVTR} = j^{\mathrm{stc}}/A$, under specific temperature and humidity conditions. The apparatus used has been described in detail by Andrikopoulos et al. (2014). From the WVTR, the specific water vapor transmission rate can be obtained by normalizing it to the membrane thickness ℓ: Sp. WVTR $= \mathrm{WVTR} \cdot \ell$. The Sp. WVTR is connected to the membranes' water vapor permeability by the following relation:

$$P = \frac{\text{Sp. WVTR}}{\Delta p} = \frac{\text{Sp. WVTR}}{p_{\mathrm{sat}}(\mathrm{RH}_1 - \mathrm{RH}_2)} \tag{A.2.2}$$

where p_{sat} is the saturation vapor pressure at the test temperature and RH_1 and RH_2 are the relative humidities at the upstream side and downstream side of the

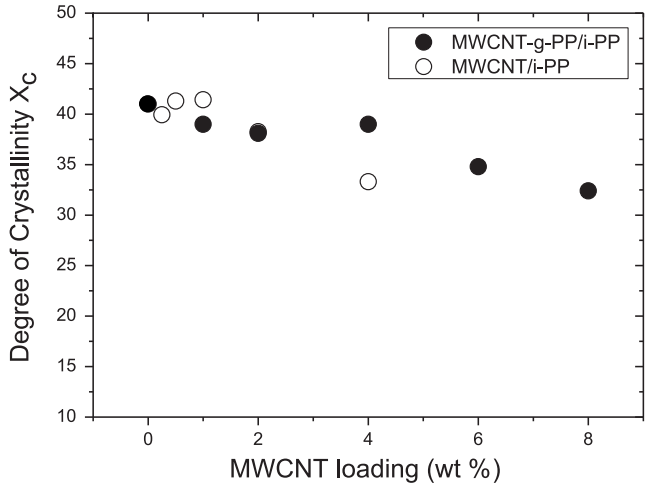

FIGURE 2. Degree of crystallinity of iPP nanocomposites as a function of MWCNT weight fraction. Note that the points relative to MWCNT/iPP and MWCNT-g-PP/iPP at 2 % filler loading overlap. Reproduced from (Bounos et al., 2017) with permission from Elsevier.

membrane, respectively. The measurements were carried out at $T = 310$ K and with $\mathrm{RH}_1 = 100\%$ and $\mathrm{RH}_2 = 50\%$.

For the gas transport measurements, the CV procedure described in section 4.1.1 was used. The samples' thickness was between 80 and 200 µm. CO_2, N_2 and H_2 were used as test gases and the membrane temperature was changed systematically from 290 K and 370 K.

Further permeation measurements were carried out independently by using a Wicke-Kallenbach setup. The permeance of H_2O, CO_2 and CH_4 was measured at 296 K using He as a sweep gas. The composition of the permeated gas was determined using a Shimadzu GC-2014 gas chromatograph equipped with a thermal conductivity detector.

A.3. Influence of MWCNT addition on water vapor and gas transport properties

The water vapor permeability value measured at 310 K is $P_{\mathrm{H_2O}} = 2.98 \times 10^5$ ml(STP) µm m^{-2} day^{-1} kPa^{-1}, in agreement with literature values (Barrie et al., 1968). The ratio P/P_{iPP} between the water vapor permeability of pure iPP and that of the nanocomposite membranes is plotted for different filler loadings in Figure 3. The permeability of the MWCNT/iPP membranes increases with increasing filler loading up to a critical concentration of 2 wt. %, where the ratio P/P_{iPP} reaches a maximum value of ~ 22. For higher filler concentration, the nanocomposite

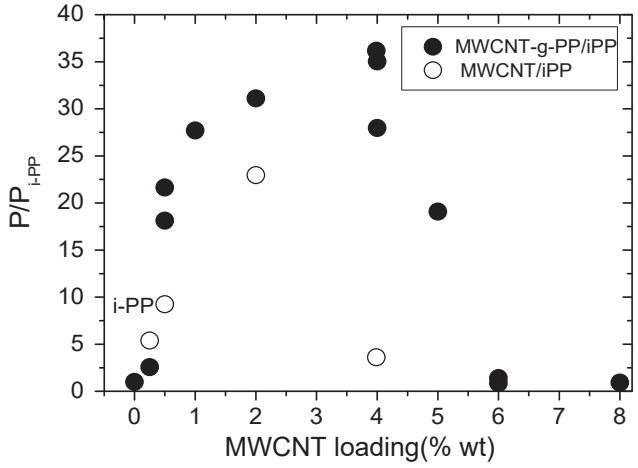

FIGURE 3. Ratio P/P_{iPP} between the water vapor permeability of the nanocomposite samples and pure iPP, plotted as a function of filler loading. Reproduced from (Bounos et al., 2017) with permission from Elsevier.

	Permeability $\left(\frac{\mathrm{ml(STP)\,\mu m}}{\mathrm{m^2\,day\,kPa}}\right)$		
membrane	H_2O vapor	CH_4	CO_2
pure iPP	1.19×10^4	4×10^1	1.26×10^3
MWCNT-g-PP/iPP (4 wt. %)	1.65×10^5	5×10^1	1.35×10^3

TABLE 1. Permeability to different gases of a 70 µm thick iPP membrane and a 200 µm thick MWCNT-g-PP/iPP nanocomposite membrane with a filler loading of 4 wt. %.

permeability decreases strongly. A similar behavior is observed with the MWCNT-g-iPP/PP membranes, but in this case the critical concentration is 4 wt. %, where P/P_{iPP} reaches a maximum of ~ 35. Such behaviors show that the water vapor permeability of the nanocomposites is related to the presence of MWCNT agglomerates.

To confirm these results, gas transport measurements were carried out with the Wicke-Kallenbach setup, comparing the gas permeability of a iPP membrane with that of a MWCNT-g-PP/iPP membrane with 4 wt % filler loading. The results obtained with water vapor, CO_2 and CH_4 are reported in Table 1. The water vapor permeability data confirm the observations made using the wet cup method: the permeability increases by more than one order of magnitude after the addition of the MWCNT-g-PP fillers. With CO_2 and CH_4, instead, no significant change was observed between the pure and the nanocomposite membrane.

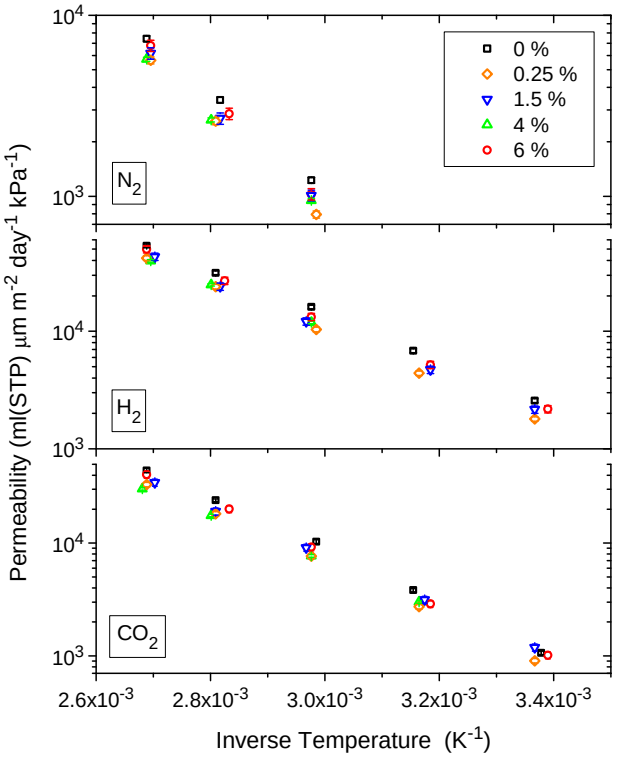

FIGURE 4. Arrhenius plots of N_2, H_2 and CO_2 permeability through iPP and MWCNT-g-PP/iPP membranes. The filler loadings are indicated in the legend.

Further gas transport studies were carried out by monitoring CO_2, N_2 and H_2 permeability and diffusivity as a function of temperature. We analyzed a pure iPP membrane and four MWCNT-g-PP/iPP samples with filler loadings between 0.25 wt. % and 6 wt. %. The permeability and diffusivity data are shown, respectively, in Figures 4 and 5. We note that: i) the diffusivity of N_2 could not be measured for temperatures lower than 330 K because of the poor signal to noise ratio of those measurements and ii) due to the short timelag, the diffusivity of H_2 could not be measured with the studied samples. From the Arrhenius plots of the experimental data in Figures 4 and 5, the apparent activation energies for permeation E_P and diffusion E_D (see equations (2.1.29) and (2.1.26)) were measured and are plotted in Figure 6. No difference can be observed in the gas permeability and diffusivity, nor in the respective apparent activation energies, between the pure iPP membrane and the different nanocomposites, meaning that the diffusion mechanism of gas molecules in all studied membranes is the same. These results confirm those obtained with the Wicke-Kallenbach setup. To summarize, we have observed that the water vapor permeability of the nanocomposite samples increases with increasing filler content up to a critical concentration and it drops again for higher filler concentrations.

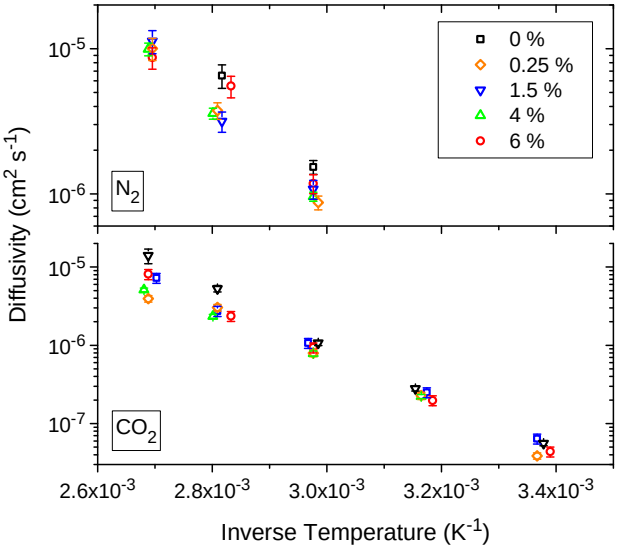

FIGURE 5. Arrhenius plots of N_2 and CO_2 diffusivity in iPP and MWCNT-g-PP/iPP membranes. The filler loadings are indicated in the legend.

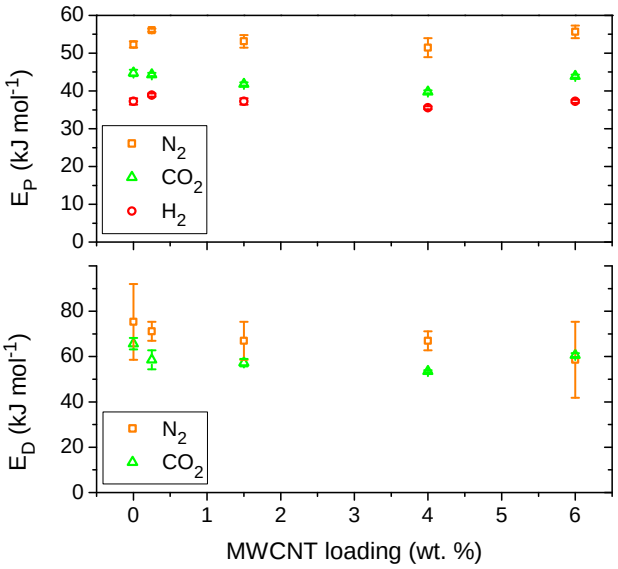

FIGURE 6. Apparent activation energies for permeation (E_P) and for diffusion (E_D) of the three test gases in the MWCNT-g-PP/iPP nanocomposite membranes as a function of filler loading.

The gas transport parameters and their activation energies, on the other hand, do not change with the filler content.

As we have seen in chapters 1 and 6, the addition of fillers can affect the transport properties of the membranes by locally changing the polymer structure. DSC measurements revealed that the degree of crystallinity of the matrix is not affected by the presence of the fillers up to the critical concentration (see section A.2.3). The addition of MWCNTs may then alter the transport properties of the membrane by: i) changing the free volume structure of the polymer at the interface or ii) give rise to defects such as pores at the matrix-filler interface. Remembering equation (2.3.3), i.e. $D = A_D \exp(^{-B_D}/_f)$, we strike out the strong (exponential) dependence of the gas diffusivity on the fractional free volume f. On the other hand, in the case of interface pores, gas molecules would diffuse into them with a diffusivity given by Knudsen: $D_{\mathrm{K}} = \frac{d_{\mathrm{pore}}}{3}\sqrt{\frac{8}{\pi}\frac{k_{\mathrm{B}}T}{M}}$, where d_{pore} is the size of the void and M is the molecular weight of the diffusing molecule. Both a change in the fractional free volume f and the formation of pores would influence the transport of all penetrants in the same manner, and they cannot explain the fact that permeability of water changes dramatically upon MWCNT addition, whereas gas transport seems to be unaffected by the presence of fillers.

We thus suggest that the transport properties of these membranes are related to peculiar properties of the H_2O-MWCNT system. The enhanced water transport can be explained by the presence, in the membrane material, of a pseudo dispersed phase consisting of the high aspect ratio MWCNT and the surrounding matrix interphase region. Since no measurable water desorption was detected on the MWCNT samples used in this work, we can attribute the enhanced water vapor permeability of the composites to an increased water diffusivity. Water diffusion may be promoted by the atomic-scale smoothness of the MWCNT, which provides an almost friction-less transport mechanism for water (Kalra et al., 2003). This scenario is compatible with the observed increase in water permeability with increasing filler concentration and dispersion. A higher concentration of the fillers implies that a higher volume fraction of the membrane is occupied by the pseudo-dispersed phase. When the filler concentrations is higher than the critical concentrations, the water permeability decreases. This effect can be attributed to the appearance of MWCNT agglomerates. However, the exact mechanism responsible for this behavior is still to be completely cleared.

A.4. Conclusions

The addition of pristine and functionalized Multi Walled Carbon NanoTubes in a isotactic PolyPropylene matrix selectively enhances the water vapor permeability of the material, while leaving unchanged the permeability to other gases such as N_2, CO_2, H_2, CH_4. Structural analysis of the samples indicates that the water vapor permeability enhancement is closely related to the carbon nanotubes' dispersion which, on turn, is improved by their surface functionalization with PP. The water

vapor permeability can be explained by the formation of a region, at the polymer-matrix interface, characterized by fast water transport rates. It is still an open point the reason why gas molecules transport in this region is not enhanced in a similar manner.

Bibliography

Adame, D. and Beall, G. W. (2009). Direct measurement of the constrained polymer region in polyamide/clay nanocomposites and the implications for gas diffusion. *Applied Clay Science*, 42:545–552.

Andrikopoulos, K. S., Bounos, G., Tasis, D., Sygellou, L., Drakopoulos, V., and Voyiatzis, G. A. (2014). The effect of thermal reduction on the water vapor permeation in graphene oxide membranes. *Advanced Materials Interfaces*, 1(8).

Aroon, M., Ismail, M., Matsuura, T., and Montazer-Rahmati, M. (2010). Performance studies of mixed matrix membranes for gas separation: A review. *Sep. Purif. Technol.*, 75:229–242.

Ash, B. J., Schadler, L. S., and Siegel, R. W. (2002). Glass transition behavior of alumina/polymethylmethacrylate nanocomposites. *Materials Letters*, 55(12):83–87.

ASTM International (2010). Astm e96 / e96m-10, standard test methods for water vapor transmission of materials.

Aulin, C., Gällstedt, M., and Lindström, T. (2010). Oxygen and oil barrier properties of microfibrillated cellulose films and coatings. *Cellulose*, 17(3):559–574.

Aulin, C., Karabulut, E., Tran, A., Wågberg, L., and Lindström, T. (2013). Correction to Transparent Nanocellulosic Multilayer Thin Films on Polylactic Acid with Tunable Gas Barrier Properties. *ACS Appl. Mater. Interfaces*, 5(20):10395–10396.

Baker, R. W. (2004). *Membrane Technology and Applications, 2nd Edition.* John Wiley & Sons, Ltd, Chichester, England.

Baker, R. W. (2009). Membrane gas-separation: Applications. In Drioli, E. and Giorno, L., editors, *Membrane Operations - Innovative Separations and Transformations*, pages 167–194. WILEY-VCH Verlag GmbH & Co. KGaA, Weinheim.

Baker, R. W. and Low, B. T. (2014). Gas Separation Membrane Materials: A Perspective. *Macromolecules*, 47(20):6999–7013.

Bansal, A., Yang, H., Li, C., Cho, K., Benicewicz, B. C., Kumar, S. K., and Schadler, L. S. (2005). Quantitative equivalence between polymer nanocomposites and thin polymer films. *Nature materials*, 4(9):693.

Bao, L., Dorgan, J. R., Knauss, D., Hait, S., Oliveira, N. S., and Maruccho, I. M. (2006). Gas permeation properties of poly(lactic acid) revisited. *Journal of Membrane Science*, 285(12):166–172.

Barrer, R. M. (1978). *Zeolite and Clay Minerals as Sorbents and Molecular Sieves*. Academic Press, New York.

Barrie, J., Crank, J., and Park, G. (1968). *Diffusion in Polymers*. Academic Press.

Basu, S., Khan, A. L., Cano-Odena, A., Liu, C., and Vankelecom, I. F. J. (2010). Membrane-based technologies for biogas separations. *Chem. Soc. Rev.*, 39:750–768.

Bayer, T., Cunning, B. V., Selyanchyn, R., Nishihara, M., Fujikawa, S., Sasaki, K., and Lyth, S. M. (2016). High Temperature Proton Conduction in Nanocellulose Membranes: Paper Fuel Cells. *Chemistry of Materials*, 28(13):4805–4814.

Belbekhouche, S., Bras, J., Siqueira, G., Chappey, C., Lebrun, L., Khelifi, B., Marais, S., and Dufresne, A. (2011). Water sorption behavior and gas barrier properties of cellulose whiskers and microfibrils films. *Carbohydrate Polymers*, 83(4):1740–1748.

Bettotti, P., Maestri, C. A., Guider, R., Mancini, I., Nativ-Roth, E., Golan, Y., and Scarpa, M. (2016). Dynamics of Hydration of Nanocellulose Films. *Adv. Mater. Interfaces*, 3(5):1500415.

Bondi, A. (1968). *Physical Properties of Molecular Crystals, Liquids, and Glasses*. Wiley series on the science and technology of materials. Wiley.

Bounos, G., Andrikopoulos, K. S., Moschopoulou, H., Lainioti, G. C., Roilo, D., Checchetto, R., Ioannides, T., Kallitsis, J. K., and Voyiatzis, G. A. (2017). Enhancing water vapor permeability in mixed matrix polypropylene membranes through carbon nanotubes dispersion. *Journal of Membrane Science*, 524:576–584.

Brandrup, J., Immergut, E. H., Grulke, E. A., Abe, A., and Bloch, D. R. (1989). *Polymer handbook*, volume 7. Wiley New York etc.

Breck, D. W. (1974). *Zeolite Molecular Sieves: Structure, Chemistry and Use*. John Wiley & Sons, Inc., New York, NY, USA.

Burganos, V. N. (2010). Modeling and Simulation of Membrane Structure and Transport Properties. In Drioli, E. and Giorno, L., editors, *Comprehensive membrane science and engineering*, pages 29–75. Elsevier, Kidlington, UK.

Burrows, P. E., Graff, G. L., Gross, M. E., Martin, P. M., Hall, M., Mast, E., Bonham, C. C., Bennett, W. D., Michalski, L. A., Weaver, M. S., Brown, J. J., Fogarty, D., and Sapochak, L. S. (2001). Gas permeation and lifetime tests on polymer-based barrier coatings. In *Proc. SPIE*, volume 4105, pages 75–83.

Calventus, Y., Montserrat, S., and Hutchinson, J. (2001). Enthalpy relaxation of non-stoichiometric epoxy-amine resins. *Polymer*, 42(16):7081 – 7093.

Cangialosi, D., Schut, H., Wübbenhorst, M., van Turnhout, J., and van Veen, A. (2003). Accumulation of charges in polycarbonate due to positron irradiation. *Radiation Physics and Chemistry*, 68(3):507 – 510. Proceedings of the 7th International Conference on Positron and Positronium Chemistry.

Carotenuto, G., Nicola, S. D., Ausanio, G., Massarotti, D., Nicolais, L., and Pepe, G. P. (2014). Synthesis and characterization of electrically conductive polyethylene-supported graphene films. *Nanoscale Research Letters*, 9(1):475.

Caseri, W. (2000). Nanocomposites of polymers and metals or semiconductors: historical background and optical properties. *Macromolecular Rapid Communications*, 21(11):705–722.

Checchetto, R., Gratton, L. M., Miotello, A., and Cestari, C. (1995). Hydrogen permeation apparatus with thermal desorption spectroscopy capabilities. *Meas. Sci. Technol.*, 6(11):1605–1611.

Checchetto, R., Miotello, A., Nicolais, L., and Carotenuto, G. (2014). Gas transport through nanocomposite membrane composed by polyethylene with dispersed graphite nanoplatelets. *Journal of Membrane Science*, 463:196–204.

Chen, X. and Mao, S. S. (2007). Titanium dioxide nanomaterials: synthesis, properties, modifications, and applications. *Chem. Rev*, 107(7):2891–2959.

Chirayil, C. J., Mathew, L., and Thomas, S. (2014). Review of recent research in nano cellulose preparation from different lignocellulosic fibers. *Reviews on Advanced Materials Science*, 37(1/2):20 – 28.

Chung, H. S. (1996). On the Macedo-Litovitz hybrid equation for liquid viscosity. *The Journal of Chemical Physics*, 44(4):1362–1364.

Chung, T.-S., Jiang, L. Y., Li, Y., and Kulprathipanja, S. (2007). Mixed matrix membranes (MMMs) comprising organic polymers with dispersed inorganic fillers for gas separation. *Progress in polymer science*, 32:483–507.

Cohen, M. H. and Turnbull, D. (1959). Molecular Transport in Liquids and Glasses. *The Journal of Chemical Physics*, 31(5):1164–1169.

Coleman, J. N., Khan, U., Blau, W. J., and Gunko, Y. K. (2006). Small but strong: a review of the mechanical properties of carbon nanotube–polymer composites. *Carbon*, 44(9):1624–1652.

Compton, O. C., Kim, S., Pierre, C., Torkelson, J. M., and Nguyen, S. T. (2010). Crumpled graphene nanosheets as highly effective barrier property enhancers. *Advanced Materials*, 22(42):4759–4763.

Consolati, G. and Quasso, F. (2010). Morphology of Free-Volume Holes in Amorphous Polymers by Means of Positron Annihilation Lifetime Spectroscopy. In Utracki, L. A. and Jamieson, A. M., editors, *Polymer Physics: From Suspensions to Nanocomposites and Beyond*, pages 393–420. John Wiley and Sons, Hoboken.

Crank, J. (1979). *The Mathematics of Diffusion*. Clarendon Press, Oxford.

Cui, Y., Kumar, S., Kona, B. R., and Houcke, D. v. (2015). Gas barrier properties of polymer/clay nanocomposites. *RSC Adv.*, 5(78):63669–63690.

Cui, Y., Kundalwal, S. I., and Kumar, S. (2016). Gas barrier performance of graphene/polymer nanocomposites. *Carbon*, 98:313–333.

De Azeredo, H. M. (2009). Nanocomposites for food packaging applications. *Food research international*, 42(9):1240–1253.

De Volder, M. F. L., Tawfick, S. H., Baughman, R. H., and Hart, A. J. (2013). Carbon nanotubes: Present and future commercial applications. *Science*, 339(6119):535–539.

Dimovski, S., Nikitin, A., Ye, H., and Gogotsi, Y. (2004). Synthesis of graphite by chlorination of iron carbide at moderate temperatures. *J. Mater. Chem.*, 14(2):238–243.

Dlubek, G. (2010). Local free-volume distribution from pals and dynamics of polymers. In Utracki, L. A. and Jamieson, A. M., editors, *Polymer Physics: From Suspensions to Nanocomposites and Beyond*, pages 421–472. John Wiley and Sons, Hoboken.

Dlubek, G., Hassan, E. M., Krause-Rehberg, R., and Pionteck, J. (2006). Free volume of an epoxy resin and its relation to structural relaxation: Evidence from positron lifetime and pressure-volume-temperature experiments. *Phys. Rev. E*, 73:031803.

Dlubek, G., Shaikh, M. Q., Rätzke, K., Faupel, F., and Paluch, M. (2008). Temperature dependence of the free volume from positron lifetime experiments and its relation to structural dynamics: Phenylphthalein-dimethylether. *Phys. Rev. E*, 78:051505.

Dong, G., Li, H., and Chen, V. (2013). Challenges and opportunities for mixed-matrix membranes for gas separation. *J. Mater. Chem. A*, 1:4610–4630.

Duda, J. L. and Zielinski, J. M. (1996). Free-volume theory. In Neogi, P., editor, *Diffusion in Polymers*, pages 143–171. Marcel Dekker, New York, N. Y.

Dufresne, A. (2010). Polymer nanocomposites from biological sources. In Nalwa, H., editor, *Encyclopedia of Nanoscience and Nanotechnology.*, pages 543–569. American Scientific Publisher, Valencia, CA, USA, 2nd edition edition.

Dufresne, A. (2013). Nanocellulose: a new ageless bionanomaterial. *Materials Today*, 16(6):220–227.

Durbetaki, A. J. (1956). Direct titration of oxirane oxygen with hydrogen bromide in acetic acid. *Analytical Chemistry*, 28(12):2000–2001.

Ebewele, R. (2000). *Polymer Science and Technology.* CRC Press.

Egger, W. (2010). Pulsed low-energy positron beams in materials sciences. In Dupasquier, A., Mills, A. P., and Brusa, R. S., editors, *Physics with Many Positrons*, volume 174 of *Proceedings of the International School of Physics "Enrico Fermi"*, pages 419–449. North-Holland, Amsterdam.

Eldrup, M., Lightbody, D., and Sherwood, J. N. (1981). The temperature dependence of positron lifetimes in solid pivalic acid. *Chemical Physics*, 63(12):51–58.

EVONIK Industries (2015). AEROXIDE®, AERODISP® and AEROPERL® Titanium Dioxide as Photocatalyst - Technical Information 1243. https://www.aerosil.com/sites/lists/RE/DocumentsSI/TI-1243-Titanium-Dioxide-as-Photocatalyst-EN.pdf. accessed 2017-09-20.

Freeman, B. D. (1999). Basis of permeability/selectivity tradeoff relations in polymeric gas separation membranes. *Macromolecules*, 32(2):375–380.

Fujishima, A., Rao, T. N., and Tryk, D. A. (2000). Titanium dioxide photocatalysis. *Journal of Photochemistry and Photobiology C: Photochemistry Reviews*, 1(1):1 – 21.

Fukuzumi, H., Fujisawa, S., Saito, T., and Isogai, A. (2013a). Selective Permeation of Hydrogen Gas Using Cellulose Nanofibril Film. *Biomacromolecules*, 14(5):1705–1709.

Fukuzumi, H., Saito, T., and Isogai, A. (2013b). Influence of TEMPO-oxidized cellulose nanofibril length on film properties. *Carbohydrate Polymers*, 93(1):172–177.

Fukuzumi, H., Saito, T., Iwamoto, S., Kumamoto, Y., Ohdaira, T., Suzuki, R., and Isogai, A. (2011). Pore Size Determination of TEMPO-Oxidized Cellulose Nanofibril Films by Positron Annihilation Lifetime Spectroscopy. *Biomacromolecules*, 12(11):4057–4062.

Fukuzumi, H., Saito, T., Iwata, T., Kumamoto, Y., and Isogai, A. (2009). Transparent and High Gas Barrier Films of Cellulose Nanofibers Prepared by TEMPO-Mediated Oxidation. *Biomacromolecules*, 10(1):162–165.

Ganesh, K., Nagarajan, R., and Duda, J. L. (1992). Rate of gas transport in glassy polymers: a free volume based predictive model. *Industrial & Engineering Chemistry Research*, 31(3):746–755.

Gavalas, G. R. (2006). Zeolite Membranes for Gas and Liquid Separations. In Yampolskii, Y., Pinnau, I., and Freeman, B. D., editors, *Materials Science of Membranes for Gas and Vapor Separation*, pages 307–333. John Wiley & Sons, Ltd, Chichester, West Sussex, England.

George, S. C. and Thomas, S. (2001). Transport phenomena through polymeric systems. *Progress in Polymer Science*, 26(6):985 – 1017.

Ghosal, K. and Freeman, B. D. (1994). Gas separation using polymer membranes: an overview. *Polymers for Advanced Technologies*, 5(11):673–697.

Gilbert, M. D., Schneider, N. S., and MacKnight, W. J. (1991). Mechanism of the dicyandiamide/epoxide reaction. *Macromolecules*, 24:360–369.

Gonzàlez, M. G., Cabanelas, J. C., and Baselga, J. (2012). Applications of ftir on epoxy resins-identification, monitoring the curing process, phase separation and water uptake. *Infrared Spectroscopy - Materials Science, Engineering and Technology*, pages 261–284.

Gringolts, M., Bermeshev, M., Yampolskii, Y., Starannikova, L., Shantarovich, V., and Finkelshtein, E. (2010). New high permeable addition poly (tricyclononenes) with si (ch3) 3 side groups. synthesis, gas permeation parameters, and free volume. *Macromolecules*, 43(17):7165–7172.

Guinault, A., Sollogoub, C., Ducruet, V., and Domenek, S. (2012). Impact of crystallinity of poly (lactide) on helium and oxygen barrier properties. *European Polymer Journal*, 48(4):779–788.

Han, S. H., Misdan, N., Kim, S., Doherty, C. M., Hill, A. J., and Lee, Y. M. (2010). Thermally rearranged (tr) polybenzoxazole: effects of diverse imidization routes on physical properties and gas transport behaviors. *Macromolecules*, 43(18):7657–7667.

Hanika, M., Langowski, H.-C., Moosheimer, U., and Peukert, W. (2003). Inorganic Layers on Polymeric Films Influence of Defects and Morphology on Barrier Properties. *Chemical Engineering & Technology*, 26(5):605–614.

Harada, M., Okamoto, N., and Ochi, M. (2016). Influence of the introduction of flexible alkyl chains on the thermal behavior and mechanical properties of mesogenic epoxy thermosets. *J. Appl. Polym. Sci.*, 133(47):n/a–n/a.

Harton, S. E., Kumar, S. K., Yang, H., Koga, T., Hicks, K., Lee, H., Mijovic, J., Liu, M., Vallery, R. S., and Gidley, D. W. (2010). Immobilized Polymer Layers on Spherical Nanoparticles. *Macromolecules*, 43(7):3415–3421.

He, X. and Hwang, H.-M. (2016). Nanotechnology in food science: Functionality, applicability, and safety assessment. *Journal of Food and Drug Analysis*, 24(4):671–681.

Herrera, M. A., Sirviö, J. A., Mathew, A. P., and Oksman, K. (2016). Environmental friendly and sustainable gas barrier on porous materials: Nanocellulose coatings prepared using spin- and dip-coating. *Materials & Design*, 93(Supplement C):19–25.

Herrera-Alonso, J. M., Sedláková, Z., and Marand, E. (2010). Gas transport properties of polyacrylate/clay nanocomposites prepared via emulsion polymerization. *Journal of Membrane Science*, 363(1):48–56.

Hoa, S. (2009). *Principles of the Manufacturing of Composite Materials*. DEStech Publications, Incorporated.

Hoge, H. J. and Lassiter, J. W. (1951). Critical temperatures, Pressures, and Volumes of Hydrogen , Deuterium, and Hydrogen Deuteride. *Journal of Research of the National Bureau of Standards*, 47(2):75–79.

Holt, A. P., Griffin, P. J., Bocharova, V., Agapov, A. L., Imel, A. E., Dadmun, M. D., Sangoro, J. R., and Sokolov, A. P. (2014). Dynamics at the Polymer/Nanoparticle Interface in Poly(2-vinylpyridine)/Silica Nanocomposites. *Macromolecules*, 47(5):1837–1843.

Holt, A. P., Sangoro, J. R., Wang, Y., Agapov, A. L., and Sokolov, A. P. (2013). Chain and Segmental Dynamics of Poly(2-vinylpyridine) Nanocomposites. *Macromolecules*, 46(10):4168–4173.

Hristov, H., Bolan, B., Yee, A., Xie, L., and Gidley, D. (1996). Measurement of hole volume in amorphous polymers using positron spectroscopy. *Macromolecules*, 29(26):8507–8516.

Hu, C.-C., Lee, K.-R., Ruaan, R.-C., Jean, Y., and Lai, J.-Y. (2006). Gas separation properties in cyclic olefin copolymer membrane studied by positron annihilation, sorption, and gas permeation. *Journal of membrane science*, 274(1):192–199.

Huang, Y. and Paul, D. R. (2007). Effect of film thickness on the gas-permeation characteristics of glassy polymer membranes. *Industrial & Engineering Chemistry Research*, 46(8):2342–2347.

Hugenschmidt, C. (2010). Positron sources and positron beams. In Dupasquier, A., Mills, A. P., and Brusa, R. S., editors, *Physics with Many Positrons*, volume 174 of *Proceedings of the International School of Physics "Enrico Fermi"*, pages 399–417. North-Holland, Amsterdam.

Hugenschmidt, C., Löwe, B., Mayer, J., Piochacz, C., Pikart, P., Repper, R., Stadlbauer, M., and Schreckenbach, K. (2008). Unprecedented intensity of a low-energy positron beam. *Nuclear Instruments and Methods in Physics Research Section A: Accelerators, Spectrometers, Detectors and Associated Equipment*, 593(3):616–618.

Indrakanti, A., Jones, R. L., and Kumar, S. K. (2004). Do nonequilibrium effects control strong surface segregation from polymer blends? *Macromolecules*, 37(1):9–12.

Ismail, A., Goh, P. S., Sanip, S. M., and Aziz, M. (2009). Transport and separation properties of carbon nanotube-mixed matrix membrane. *Separation and Purification Technology*, 70(1):12–26.

Jacobson, R. A., Wunderlich, J. A., and Lipscomb, W. N. (1961). The crystal and molecular structure of cellobiose. *Acta Crystallographica*, 14(6):598–607.

Jamshidian, M., Tehrany, E. A., Imran, M., Jacquot, M., and Desobry, S. (2010). Poly-Lactic Acid: Production, Applications, Nanocomposites, and Release Studies. *Comprehensive Reviews in Food Science and Food Safety*, 9(5):552–571.

Jasiska, B., Kozio, A., and Goworek, T. (1996). Ortho-positronium lifetimes in non-spherical voids. *Journal of Radioanalytical and Nuclear Chemistry*, 210(2):617–623.

Jean, Y. C. (1995). Characterizing free volumes and holes in polymers by positrion annihilation spectroscopy. In Dupasquier, A. and Mills, A., editors, *Positron Spectroscopy of Solids*. IOS Press.

Jean, Y. C., Van Horn, J. D., Hung, W.-S., and Lee, K.-R. (2013). Perspective of positron annihilation spectroscopy in polymers. *Macromolecules*, 46(18):7133–7145.

Jin, J., Rafiq, R., Gill, Y. Q., and Song, M. (2013). Preparation and characterization of high performance of graphene/nylon nanocomposites. *European Polymer Journal*, 49(9):2617–2626.

Jordan, C., Galy, J., and Pascault, J.-P. (1992). Measurement of the extent of reaction of an epoxycycloaliphatic amine system and influence of the extent of reaction on its dynamic and static mechanical properties. *Journal of Applied Polymer Science*, 46(5):859–871.

Kalaitzidou, K., Fukushima, H., and Drzal, L. T. (2007). Multifunctional polypropylene composites produced by incorporation of exfoliated graphite nanoplatelets. *Carbon*, 45(7):1446–1452.

Kalra, A., Garde, S., and Hummer, G. (2003). Osmotic water transport through carbon nanotube membranes. *Proceedings of the National Academy of Sciences*, 100(18):10175–10180.

Kansy, J. (1996). Microcomputer program for analysis of positron annihilation lifetime spectra. *Nuclear Instruments and Methods in Physics Research Section A: Accelerators, Spectrometers, Detectors and Associated Equipment*, 374(2):235 – 244.

Kim, H., Abdala, A. A., and Macosko, C. W. (2010). Graphene/Polymer Nanocomposites. *Macromolecules*, 43(16):6515–6530.

Kim, H. and Macosko, C. W. (2009). Processing-property relationships of polycarbonate/graphene composites. *Polymer*, 50(15):3797–3809.

Kim, S., Marand, E., Ida, J., and Guliants, V. V. (2006). Polysulfone and mesoporous molecular sieve MCM-48 mixed matrix membranes for gas separation. *Chemistry of materials*, 18(5):1149–1155.

Kirkegaard, P., Pedersen, N. J., and Eldrup, M. (1989). PATFIT-88 (RISO-M–2740). *Risoe National Lab., Roskilde (Denmark)*, 20(14).

Klemm, D., Kramer, F., Moritz, S., Lindström, T., Ankerfors, M., Gray, D., and Dorris, A. (2011). Nanocelluloses: A New Family of Nature-Based Materials. *Angew. Chem. Int. Ed.*, 50(24):5438–5466.

Komatsuka, T., Kusakabe, A., and Nagai, K. (2008). Characterization and gas transport properties of poly(lactic acid) blend membranes. *Desalination*, 234(1):212–220.

Krevelen, D. (1990). *Properties of Polymers: Their Correlation with Chemical Structure, Their Numerical Estimation and Prediction from Additive Group Contributions*. Elsevier.

Kwisnek, L., Kaushik, M., Hoyle, C. E., and Nazarenko, S. (2010). Free volume, transport, and physical properties of n-alkyl derivatized thiol- ene networks:

Chain length effect. *Macromolecules*, 43(8):3859–3867.

Lavoine, N., Desloges, I., Dufresne, A., and Bras, J. (2012). Microfibrillated cellulose Its barrier properties and applications in cellulosic materials: A review. *Carbohydrate Polymers*, 90(2):735–764.

Lavoine, N., Desloges, I., Khelifi, B., and Bras, J. (2014). Impact of different coating processes of microfibrillated cellulose on the mechanical and barrier properties of paper. *Journal of Materials Science*, 49.

Lee, C., Wei, X., Kysar, J. W., and Hone, J. (2008). Measurement of the elastic properties and intrinsic strength of monolayer graphene. *Science*, 321(5887):385–388.

Lee, S. H., Cho, E., Jeon, S. H., and Youn, J. R. (2007). Rheological and electrical properties of polypropylene composites containing functionalized multi-walled carbon nanotubes and compatibilizers. *Carbon*, 45(14):2810–2822.

Lee, W. M. (1980). Selection of barrier materials from molecular structure. *Polymer Engineering & Science*, 20(1):65–69.

Leenaerts, O., Partoens, B., and Peeters, F. M. (2008). Graphene: A perfect nanoballoon. *Applied Physics Letters*, 93(19):193107.

Li, Y. and Chung, T. S. (2008). Highly selective sulfonated polyethersulfone (spes)-based membranes with transition metal counterions for hydrogen recovery and natural gas separation. *Journal of Membrane Science*, 308(1):128 – 135.

Li, Y., Chung, T.-S., Cao, C., and Kulprathipanja, S. (2005). The effects of polymer chain rigidification, zeolite pore size and pore blockage on polyethersulfone (pes)-zeolite a mixed matrix membranes. *Journal of Membrane Science*, 260(1):45–55.

Lin, H. and Freeman, B. D. (2006). Gas permeation and diffusion in cross-linked poly (ethylene glycol diacrylate). *Macromolecules*, 39(10):3568–3580.

Lin, H., Freeman, B. D., Kalakkunnath, S., and Kalika, D. S. (2007). Effect of copolymer composition, temperature, and carbon dioxide fugacity on pure-and mixed-gas permeability in poly (ethylene glycol)-based materials: Free volume interpretation. *Journal of membrane science*, 291(1):131–139.

Lin, H., Kai, T., Freeman, B. D., Kalakkunnath, S., and Kalika, D. S. (2005). The effect of cross-linking on gas permeability in cross-linked poly(ethylene glycol diacrylate). *Macromolecules*, 38(20):8381–8393.

Liu, J., Cao, D., and Zhang, L. (2009). Static and dynamic properties of model elastomer with various cross-linking densities: A molecular dynamics study. *The Journal of Chemical Physics*, 131(3):034903.

Lu, H. and Nutt, S. (2003). Restricted Relaxation in Polymer Nanocomposites near the Glass Transition. *Macromolecules*, 36(11):4010–4016.

Lv, H.-l., Wang, B.-g., and Kong, Y. (2009). Prediction of solvent diffusivities in amorphous polymers by free-volume theory: Group contribution and pals methods. *Polymer journal*, 41(12):1049–1054.

Macedo, P. and Litovitz, T. (1965). On the relative roles of free volume and activation energy in the viscosity of liquids. *The Journal of Chemical Physics*, 42(1):245–256.

Mack, P. and Smith, M. (2005). Covalently compatible in-mold coating compositions for use with epoxy. US Patent App. 10/891,584.

Madani, M., MacQueen, R., and Granata, R. (1996). Positron annihilation lifetime study of ptfe/silica composites. *Journal of Polymer Science Part B: Polymer Physics*, 34(16):2767–2770.

Mahajan, R. and Koros, W. J. (2002). Mixed matrix membrane materials with glassy polymers. Part 1. *Polymer Engineering & Science*, 42(7):1420–1431.

Malhotra, B. D. and Pethrick, R. A. (1983). Correlation of dielectric relaxation and positron annihilation in glass-forming liquids. *Phys. Rev. B*, 28:1256–1262.

Mallon, P. E. (2003). Application to Polymers. In Mallon, P. E., Jean, Y. C., and Schrader, D. M., editors, *Principles and Applications of Positron and Positronium Chemistry*, pages 253–280. World Scientific, Singapore.

Matteucci, S., Yampolskii, Y., Freeman, B. D., and Pinnau, I. (2006). Transport of Gases and Vapors in Glassy and Rubbery Polymers. In Yampolskii, Y., Pinnau, I., and Freeman, B. D., editors, *Materials Science of Membranes for Gas and Vapor Separation*, pages 1–48. John Wiley & Sons, Ltd, Chichester, West Sussex, England.

Maxwell, J. C. (1873). *A Treatise on Electricity and Magnetism*. Oxford Univ. Press, London. Google-Books-ID: gokfAQAAMAAJ.

Meares, P. (1954). The diffusion of gases through polyvinyl acetate1. *Journal of the American Chemical Society*, 76(13):3415–3422.

Miller, K. S. and Krochta, J. M. (1997). Oxygen and aroma barrier properties of edible films: A review. *Trends in Food Science & Technology*, 8(7):228–237.

Mills, A. P. and Wilson, R. J. (1982). Transmission of 1 - 6-keV positrons through thin metal films. *Phys. Rev. A*, 26(1):490–500.

Müller, A., Zink, M., Hessler, N., Wesarg, F., Müller, F. A., Kralisch, D., and Fischer, D. (2014). Bacterial nanocellulose with a shape-memory effect as potential drug delivery system. *RSC Advances*, 4(100):57173–57184.

Mogensen, O. E. (1995). *Positron Annihilation in Chemistry*. Springer, Berlin.

Moll, J. and Kumar, S. K. (2012). Glass Transitions in Highly Attractive Highly Filled Polymer Nanocomposites. *Macromolecules*, 45(2):1131–1135.

Moore, T. and Koros, W. (2005). Non-ideal effects in organic-inorganic materials for gas separation membranes. *Journal of molecular structure*, 739:87–98.

Moore, T. T., Mahajan, R., Vu, D. Q., and Koros, W. J. (2004). Hybrid membrane materials comprising organic polymers with rigid dispersed phases. *AIChE journal*, 50(2):311–321.

Nagel, C., Günther-Schade, K., Fritsch, D., Strunskus, T., and Faupel, F. (2002). Free volume and transport properties in highly selective polymer membranes. *Macromolecules*, 35(6):2071–2077.

Nagel, C., Schmidtke, E., Günther-Schade, K., Hofmann, D., Fritsch, D., Strunskus, T., and Faupel, F. (2000). Free volume distributions in glassy polymer membranes: comparison between molecular modeling and experiments. *Macromolecules*, 33(6):2242–2248.

Nair, R. R., Blake, P., Grigorenko, A. N., Novoselov, K. S., Booth, T. J., Stauber, T., Peres, N. M. R., and Geim, A. K. (2008). Fine structure constant defines visual transparency of graphene. *Science*, 320(5881):1308–1308.

Nakanishi, H. and Jean, Y. C. (1988). Positrons and positronium in liquids. In Schrader, D. M. and Jean, Y. C., editors, *Positron and positronium chemistry*. Elsevier, Amsterdam, The Netherlands.

Neas, D. and Klapetek, P. (2012). Gwyddion: an open-source software for SPM data analysis. *Central European Journal of Physics*, 10(1):181–188.

Nielsen, E. (1967). Models for the permeability of filled polymer systems. *J. Macromol. Sci. Chem. A*, 1:929–942.

NIST (2017). NIST | National Institute of Standards and Technology. accessed 2017-09-27.

Nogi, M., Handa, K., Nakagaito, A. N., and Yano, H. (2005). Optically transparent bionanofiber composites with low sensitivity to refractive index of the polymer matrix. *Applied Physics Letters*, 87(24):243110.

Noorjahan, A. and Choi, P. (2015). Effect of free volume redistribution on the diffusivity of water and benzene in poly(vinyl alcohol). *Chemical Engineering Science*, 121:258 – 267. 2013 Danckwerts Special Issue on Molecular Modelling in Chemical Engineering.

Novoselov, K. S., Falko, V. I., Colombo, L., Gellert, P. R., Schwab, M. G., and Kim, K. (2012). A roadmap for graphene. *Nature*, 490(7419):192–200.

Okabe, T., Takehara, T., Inose, K., Hirano, N., Nishikawa, M., and Uehara, T. (2013). Curing reaction of epoxy resin composed of mixed base resin and curing agent: Experiments and molecular simulation. *Polymer*, 54(17):4660 – 4668.

Okamoto, K.-i., Tanaka, K., Katsube, M., Kita, H., Sueoka, O., and Ito, Y. (1993). Correlation between positron annihilation and gas diffusion properties of various rubbery polymers. *Polymer journal*, 25(3):275–284.

Olson, B. G., Lin, J., Nazarenko, S., and Jamieson, A. M. (2003). Positron annihilation lifetime spectroscopy of poly (ethylene terephthalate): contributions from rigid and mobile amorphous fractions. *Macromolecules*, 36(20):7618–7623.

Osman, M. A., Mittal, V., Morbidelli, M., and Suter, U. W. (2004). Epoxy-layered silicate nanocomposites and their gas permeation properties. *Macromolecules*, 37(19):7250–7257.

Pal, R. (2008). Permeation models for mixed matrix membranes. *Journal of Colloid and Interface Science*, 317:191–198.

Parry, R. T. (1993). *Principles and Applications of Modified Atmosphere Packaging of Foods*. Blackie Academic & Professional, Glasgow, UK. Google-Books-ID: gTvUZwEACAAJ.

Pascault, J. P., Sauterau, H., Verdu, J., and Williams, R. J. J. (2012). *Thermosetting polymers*. Marcel Dekker, New York.

Patel, A., Maiorana, A., Yue, L., Gross, R. A., and Manas-Zloczower, I. (2016). Curing Kinetics of Biobased Epoxies for Tailored Applications. *Macromolecules*, 49(15):5315–5324.

Paterson, R., Yampolskii, Y., Fogg, P. G., Bokarev, A., Bondar, V., Ilinich, O., and Shishatskii, S. (1999). IUPAC-NIST solubility data series 70. Solubility of gases in glassy polymers. *Journal of Physical and Chemical Reference Data*, 28(5):1255–1450.

Patil, P. N., Rath, S. K., Sharma, S. K., Sudarshan, K., Maheshwari, P., Patri, M., Praveen, S., Khandelwal, P., and Pujari, P. K. (2013). Free volumes and structural relaxations in diglycidyl ether of bisphenol-a based epoxy-polyether amine networks. *Soft Matter*, 9:3589–3599.

Paul, D. and Robeson, L. (2008). Polymer nanotechnology: Nanocomposites. *Polymer*, 49(15):3187 – 3204.

Paul, D. R. (2010). Fundamentals of transport phenomena in polymeric membranes. In Drioli, E. and Giorno, L., editors, *Comprehensive Membrane Science and Engineering*, pages 75–90. Elsevier, Kidlington, OX5, United Kingdom.

Pauly, S. (1999). Permeability and diffusion data. In Brandrup, J., Immergut, E. H., and Grulke, editors, *Polymer Handbook*, pages 543–569. John Wiley & Sons, New York, NY, USA, 4th edition edition.

Pethrick, R. A., Jacobsen, F. M., Mogensen, O. E., and Eldrup, M. (1980). Positron lifetime study of the transition from glassy to normal liquid state for two phenyl ethers. *J. Chem. Soc., Faraday Trans. 2*, 76:225–232.

Pönni, R., Vuorinen, T., and Kontturi, E. (2012). Proposed nano-scale coalescence of cellulose in chemical pulp fibers during technical treatments. *Bioresources*, 7(4):6077–6108.

Poelman, D. and Smet, P. F. (2003). Methods for the determination of the optical constants of thin films from single transmission measurements: a critical review. *J. Phys. D: Appl. Phys.*, 36(15):1850–1857.

Potts, J. R., Dreyer, D. R., Bielawski, C. W., and Ruoff, R. S. (2011). Graphene-based polymer nanocomposites. *Polymer*, 52(1):5 – 25.

Poulsen, L., Zebger, I., Klinger, M., Eldrup, M., Sommer-Larsen, P., and Ogilby, P. R. (2003). Oxygen diffusion in copolymers of ethylene and norbornene. *Macromolecules*, 36(19):7189–7198.

Pramanik, M., Acharya, H., and Srivastava, S. K. (2004). Exertion of inhibiting effect by aluminosilicate layers on swelling of solution blended EVA/clay nanocomposite. *Macromolecular Materials and Engineering*, 289(6):562–567.

Prashantha, K., Soulestin, J., Lacrampe, M., Claes, M., Dupin, G., and Krawczak, P. (2008). Multi-walled carbon nanotube filled polypropylene nanocomposites based on masterbatch route: Improvement of dispersion and mechanical properties through pp-g-ma addition. *express polymer letters*, 2(10):735–745.

Qi, C., Ma, D., Hu, Y., Yan, F., Gao, H., Yang, Z., Zhou, X., and Wang, T. (2001). The buildup of the electric field during positron annihilation lifetime spectroscopy measurement. *Journal of Polymer Science Part B: Polymer Physics*, 39(3):332–336.

Redhead, P. A., Hobson, J. P., and Kornelsen, E. V. (1993). *The physical basis of ultrahigh vacuum*. American Insitute of Physics, New York, NY, USA.

Rezakazemi, M., Ebadi Amooghin, A., Montazer-Rahmati, M. M., Ismail, A. F., and Matsuura, T. (2014). State-of-the-art membrane based CO2 separation using mixed matrix membranes (MMMs): An overview on current status and future directions. *Progress in Polymer Science*, 39(5):817–861.

Rhim, J.-W., Park, H.-M., and Ha, C.-S. (2013). Bio-nanocomposites for food packaging applications. *Progress in Polymer Science*, 38(1011):1629–1652.

Ricci, F. P., Ricci, M. A., and Rocca, D. (1977). The free volume theory and the macedo-litovitz hybrid equation for diffusion in liquids. *The Journal of Physical Chemistry*, 81(2):171–177.

Rittigstein, P. and Torkelson, J. M. (2006). Polymernanoparticle interfacial interactions in polymer nanocomposites: Confinement effects on glass transition temperature and suppression of physical aging. *J. Polym. Sci. B Polym. Phys.*, 44(20):2935–2943.

Robeson, L. M. (1991). Correlation of separation factor versus permeability for polymeric membranes. *Journal of Membrane Science*, 62(2):165 – 185.

Robeson, L. M. (2008). The upper bound revisited. *Journal of Membrane Science*, 320(1):390 – 400.

Rodionova, G., Lenes, M., Eriksen, y., and Gregersen, y. (2011). Surface chemical modification of microfibrillated cellulose: improvement of barrier properties for packaging applications. *Cellulose*, 18(1):127–134.

Roilo, D., Maestri, C. A., Scarpa, M., Bettotti, P., Egger, W., Koschine, T., Brusa, R. S., and Checchetto, R. (2017). Cellulose Nanofibrils Films: Molecular Diffusion through Elongated Sub-Nano Cavities. *The Journal of Physical Chemistry C*, 121(28):15437–15447.

Rudel, M., Kruse, J., Rätzke, K., Faupel, F., Yampolskii, Y. P., Shantarovich, V. P., and Dlubek, G. (2008). Temperature dependence of positron annihilation lifetimes in high permeability polymers: amorphous teflons af. *Macromolecules*, 41(3):788–795.

Sadasivuni, K. K., Saiter, A., Gautier, N., Thomas, S., and Grohens, Y. (2013). Effect of molecular interactions on the performance of poly(isobutylene-co-isoprene)/graphene and clay nanocomposites. *Colloid and Polymer Science*, 291(7):1729–1740.

Sahoo, N. G., Rana, S., Cho, J. W., Li, L., and Chan, S. H. (2010). Polymer nanocomposites based on functionalized carbon nanotubes. *Progress in polymer science*, 35(7):837–867.

Saito, T., Kimura, S., Nishiyama, Y., and Isogai, A. (2007). Cellulose nanofibers prepared by TEMPO-mediated oxidation of native cellulose. *Biomacromolecules*, 8(8):2485–2491.

Sanip, S., Ismail, A. F., Goh, P., Soga, T., Tanemura, M., and Yasuhiko, H. (2011). Gas separation properties of functionalized carbon nanotubes mixed matrix membranes. *Separation and Purification Technology*, 78(2):208–213.

Semiat, R. and Hasson, D. (2009). Seawater and brackish-water desalination with membrane operations. In Drioli, E. and Giorno, L., editors, *Membrane Operations - Innovative Separations and Transformations*, pages 221–4243. WILEY-VCH Verlag GmbH & Co. KGaA, Weinheim.

Siqueira, G., Bras, J., and Dufresne, A. (2010). Cellulosic bionanocomposites: A review of preparation, properties and applications. *Polymers*, 2(4):728–765.

Siracusa, V., Rocculi, P., Romani, S., and Dalla Rosa, M. (2008). Biodegradable polymers for food packaging: a review. *Trends in Food Science & Technology*, 19(12):634–643.

Sorrentino, A., Gorrasi, G., and Vittoria, V. (2007). Potential perspectives of bio-nanocomposites for food packaging applications. *Trends in Food Science & Technology*, 18:84–95.

Sperr, P., Egger, W., Kögel, G., Dollinger, G., Hugenschmidt, C., Repper, R., and Piochacz, C. (2008). Status of the pulsed low energy positron beam system (PLEPS) at the Munich Research Reactor FRM-II. *Applied Surface Science*, 255(1):35–38.

Starner, W. E. (1997). Reactive accelerators for amine cured epoxy resins. US Patent 5,591,812.

Starr, F. W., Douglas, J. F., Meng, D., and Kumar, S. K. (2016). Bound Layers Cloak Nanoparticles in Strongly Interacting Polymer Nanocomposites. *ACS Nano*, 10(12):10960–10965.

Syverud, K. and Stenius, P. (2009). Strength and barrier properties of MFC films. *Cellulose*, 16(1):75–85.

Tanaka, K., Kawai, T., Kita, H., Okamoto, K.-i., and Ito, Y. (2000). Correlation between gas diffusion coefficient and positron annihilation lifetime in polymers with rigid polymer chains. *Macromolecules*, 33(15):5513–5517.

Tao, S. J. (1972). Positronium Annihilation in Molecular Substances. *The Journal of Chemical Physics*, 56(11):5499–5510.

Thornton, A. W., Nairn, K. M., Hill, A. J., and Hill, J. M. (2009). New relation between diffusion and free volume: I. predicting gas diffusion. *Journal of Membrane Science*, 338(1):29–37.

Thran, A., Kroll, G., and Faupel, F. (1999). Correlation between fractional free volume and diffusivity of gas molecules in glassy polymers. *Journal of Polymer Science Part B: Polymer Physics*, 37(23):3344–3358.

Tian, N., Ning, R., and Kong, J. (2016). Self-toughening of epoxy resin through controlling topology of cross-linked networks. *Polymer*, 99:376–385.

Ul-Islam, M., Khattak, W. A., Kang, M., Kim, S. M., Khan, T., and Park, J. K. (2013). Effect of post-synthetic processing conditions on structural variations and applications of bacterial cellulose. *Cellulose*, 20(1):253–263.

Urbaczewski-Espuche, E., Galy, J., Gerard, J.-F., Pascault, J.-P., and Sautereau, H. (1991). Influence of chain flexibility and crosslink density on mechanical properties of epoxy/amine networks. *Polymer Engineering & Science*, 31(22):1572–1580.

Van der Bruggen, B. (2009). Fundamentals of membrane solvent separation and pervaporation. In Drioli, E. and Giorno, L., editors, *Membrane Operations - Innovative Separations and Transformations*, pages 45–61. WILEY-VCH Verlag GmbH & Co. KGaA, Weinheim.

Vieth, W. (1991). *Diffusion in and Through Polymers: Principles and Applications*. Hanser Gardner Publications, Munich.

Vrentas, J. and Vrentas, C. (1989). Volumetric behavior of glassy polymer-penetrant systems. *Macromolecules*, 22(5):2264–2266.

Vrentas, J. S. and Duda, J. L. (1977). Diffusion in polymersolvent systems. I. Reexamination of the free-volume theory. *J. Polym. Sci. Polym. Phys. Ed.*, 15(3):403–416.

Vrentas, J. S. and Vrentas, C. M. (1991). Solvent self-diffusion in crosslinked polymers. *Journal of Applied Polymer Science*, 42(7):1931–1937.

Wang, J.-S. (1936). On the diffusion of gases through metals. *Mathematical Proceedings of the Cambridge Philosophical Society*, 32(4):657662.

Wang, X. and Zhou, W. (2002). Glass Transition of Microtome-Sliced Thin Films. *Macromolecules*, 18(35):6747–6750.

Wang, Y. Y., Nakanishi, H., Jean, Y. C., and Sandreczki, T. C. (1990). Positron annihilation in amine-cured epoxy polymerspressure dependence. *Journal of Polymer Science Part B: Polymer Physics*, 28(9):1431–1441.

Wu, J., Huang, G., Li, H., Wu, S., Liu, Y., and Zheng, J. (2013). Enhanced mechanical and gas barrier properties of rubber nanocomposites with surface functionalized graphene oxide at low content. *Polymer*, 54(7):1930–1937.

Xiao, J. and Wei, J. (1992). Diffusion mechanism of hydrocarbons in zeolites - I. Theory. *Chemical Engineering Science*, 47(5):1123–1141.

Xie, W., Ju, H., Geise, G. M., Freeman, B. D., Mardel, J. I., Hill, A. J., and McGrath, J. E. (2011). Effect of free volume on water and salt transport properties in directly copolymerized disulfonated poly (arylene ether sulfone) random copolymers. *Macromolecules*, 44(11):4428–4438.

Yampolskii, Y. and Shantarovich, V. (2006). Positron annihilation lifetime spectroscopy and other methods for free volume evaluation in polymers. In Yampolskii, Y., Pinnau, I., and Freeman, B. D., editors, *Materials Science of Membranes for Gas and Vapor Separation*, pages 190–210. John Wiley & Sons, Ltd, Chichester, West Sussex, England.

Yampolskii, Y., Shishatskii, S., Alentiev, A., and Loza, K. (1998). Correlations with and prediction of activation energies of gas permeation and diffusion in glassy polymers. *Journal of Membrane Science*, 148(1):59–69.

Yang, B.-X., Pramoda, K. P., Xu, G. Q., and Goh, S. H. (2007). Mechanical reinforcement of polyethylene using polyethylene-grafted multiwalled carbon nanotubes. *Advanced Functional Materials*, 17(13):2062–2069.

Yang, B.-X., Shi, J.-H., Pramoda, K., and Goh, S. H. (2008). Enhancement of the mechanical properties of polypropylene using polypropylene-grafted multiwalled carbon nanotubes. *Composites Science and Technology*, 68(12):2490–2497.

Yang, J., Ren, Y., Tian, A.-m., and Sun, H. (2000). Compass force field for 14 inorganic molecules, he, ne, ar, kr, xe, h2, o2, n2, no, co, co2, no2, cs2, and so2, in liquid phases. *The Journal of Physical Chemistry B*, 104(20):4951–4957.

Yoo, B. M., Shin, H. J., Yoon, H. W., and Park, H. B. (2014). Graphene and graphene oxide and their uses in barrier polymers. *Journal of Applied Polymer Science*, 131(1):39628.

Young, M. (2000). *Optics and Lasers - Including Fibers and Optical Waveguides | Matt Young | Springer*. Springer-Verlag, Berlin Heidelberg.

Zekriardehani, S., Jabarin, S., Gidley, D., and Coleman, M. (2017). Effect of chain dynamics, crystallinity, and free volume on the barrier properties of poly (ethylene terephthalate) biaxially oriented films. *Macromolecules*, 50(7):2845–2855.

Zheng, J.-M., Qiu, J., Madeira, L. M., and Mendes, A. (2007). Polymer structure and the compensation effect of the diffusion pre-exponential factor and activation energy of a permeating solute. *The Journal of Physical Chemistry B*, 111(11):2828–2835.

Zhou, J., Wang, S., and Gunasekaran, S. (2009). Preparation and Characterization of Whey Protein Film Incorporated with TiO2 Nanoparticles. *Journal of Food Science*, 74(7):N50–N56.

Zhou, X. P., Xie, X. L., Zeng, F., Li, R. K. Y., and Mai, Y. W. (2006). Properties of polypropylene/carbon nanotube composites compatibilized by maleic anhydride grafted sebs. In *Key Engineering Materials*, volume 312, pages 223–228. Trans Tech Publ.